Modeling, optimization, and characterization of high concentration photovoltaic systems using multijunction solar cells

by

Pratibha Sharma

Thesis submitted to the

Faculty of Graduate and Postdoctoral Studies

in partial fulfillment of the requirements

for the Doctorate of Philosophy degree in Electrical Engineering

School of Electrical Engineering and Computer Science

University of Ottawa

Abstract

Recent advancements in the development of high-efficiency multijunction solar cells have led to a renewed interest in the design and implementation of high concentration photovoltaic systems. With the emergence of novel materials and design structures, understanding the operation of multijunction solar cells has become a challenging task. Modeling and simulation hence play an important role in the analysis of such devices.

In this dissertation, techniques for accurate optoelectrical modeling of concentrating photovoltaic systems, based on multijunction solar cells, are proposed. A 2-dimensional, distributed circuit model is proposed, parametrized to values obtained by numerical modeling of three multijunction cell designs, namely: a three-junction, lattice matched design, a three-junction lattice-mismatched, inverted metamorphic design, and a four-junction, lattice matched design. Cell performance for all the three designs is evaluated under both uniform and nonunifom illumination profiles at high concentrations and efficiency enhancement by optimizing finger spacing is proposed. The effect of luminescent coupling from higher bandgap subcells is also determined.

Fresnel-lens based, refractive concentrating optical systems are modeled and optimized using an optical ray-tracing simulator at two different concentrations, with and without a secondary optical element. The corresponding optical efficiency, acceptance angle, and the degree of nonuniformity are determined for each optical system. An integrated approach, combining optical design with electrical modeling is proposed for optimizing the multijunction solar cell in tandem with the corresponding concentrating optics. The approach is validated by on-sun, acceptance angle measurements, using a three-junction,

lattice-matched cell.

Also, temperature effects are modeled and are experimentally validated for a three-junction, lattice-matched design. Experimental results with a single-junction, dilute-nitride cell, targeted for four-junction operation, are presented as well. A modified distributed circuit model is used for analysis of temperature effects in a four-junction solar cell, and the results under both uniform and nonuniform temperature profiles are presented.

When implemented, the designs and their corresponding analyses, may result in new insights into the development of CPV systems, thereby enabling enhanced efficiencies at higher concentrations.

Statement of originality

The author declares that results presented in this thesis were obtained during the period of her doctoral degree and under the supervision of Dr. Karin Hinzer. To the best of the author's knowledge, these results are original.

The numerical modeling of solar cells using Sentaurus was done by other members of SUNLAB. The numerical modeling of the three-junction solar cells was performed by Alex Walker and Anna Trojnar, and for the four-junction solar cell was primarily performed by Matthew Wilkins. The computer aided design (CAD) files for the Fresnel Köhler design were provided by LPI and the work was performed in collaboration with COFOVO energy. The on-sun measurements on the tracker were primarily performed by Dr. John Cook.

The work presented in this thesis has led to the following manuscripts and conference proceedings:

Publications in refereed journal and conference proceedings

P. Sharma, M. M. Wilkins, H. P. Schriemer, and K. Hinzer, *"Concentrating optical system optimization for 3- and 4-junction solar cells: impact of illumination profiles"*, Journal of Photonics for Energy, vol. 7 (1), January 2017.

R. Cheriton, M. M. Wilkins, **P. Sharma**, C. E. Valdivia, A. H. Trojnar, H. P. Schriemer, K. Hinzer, J. Gupta, B. Bouzazi, G. Kolhatkar, A. Boucherif, J. Abdelatif, S. Fafard, V. Aimez, and R. Arés, *"Design optimizations of InGaAsN(Sb) subcells for concentrator photovoltaic systems,"* Journal of Vacuum Science and Technology B, vol. 34, February 2016.

P. Sharma, M. M. Wilkins, H. P. Schriemer, and K. Hinzer, *"Optimization of a four junction solar cell CPV system using ray tracing and SPICE modeling"*, 42nd IEEE Photovoltaic Specialists conference, June 2015 (Best Student Paper award finalist).

H. P. Schriemer, J. P. D. Cook, **P. Sharma**, L. de la Salle, F. Carle, P. M. White, V. Tatsiankou, J. E. Haysom, E. Dragomirescu, and K. Hinzer, *"Refractive Concentrator Optics Architectures, Tracker Precision, and Cumulative Energy Harvest,"* 42nd IEEE Photovoltaic Specialists conference, June 2015.

P. Sharma, A. H. Trojnar, M. M. Wilkins, A. W. Walker, H. P. Schriemer and K. Hinzer, *"Comparative Analysis of Nonuniform Illumination and Chromatic Aberration in Triple and Quadruple Junction Solar Cells under Concentration Using SPICE,"* EU PVSEC 2014, September 2014.

M. M. Wilkins, A. Gabr, **P. Sharma**, H. P. Schriemer, S. Fafard, and K. Hinzer, *"4-junction solar cells with dilute nitrides: Optimization with luminescent coupling,"* EU PVSEC 2014, September 2014.

P. Sharma, A. W. Walker, J. F. Wheeldon, K. Hinzer, and H. P. S Schriemer, *"Enhanced efficiencies for high-concentration, multijunction PV systems by optimizing grid spacing under nonuniform illumination"*, International Journal on Photoenergy, Article ID 582083, August 2014.

P. Sharma, M. M. Wilkins, H. P. Schriemer, and K. Hinzer, *"Modeling nonuniform irradiance and chromatic aberration effects in a four junction solar cell using SPICE"*, Proceedings of the 40th IEEE Photovoltaic Specialists conference, June 2014.

P. Sharma, A. W. Walker, J. F. Wheeldon, H. P. Schriemer, and K. Hinzer, *"Optimization*

of finger spacing for concentrator photovoltaic cells under non-uniform illumination using spice," Proceedings of the SPIE , Photonics North Conference, June 2013.

Presentations

P. Sharma, M. M. Wilkins, R.Cheriton, C.E. Valdivia, H. P Schriemer, and K. Hinzer, *"Modeling and optimization of concentrated photovoltaic systems using 4-junction solar cells,"* Poster presentation and demonstration, Innovation 360 (CMC TEXPO 2015), Ottawa, September 2015.

K. Hinzer, C. E. Valdivia, M. M. Wilkins, R. Cheriton, **P. Sharma**, A. H. Trojnar, H. P. Schriemer, B. Bouzazi, G. Kolhatkar, A. Boucherif, A. Jaouad, S. Fafard, V. Aimez, R. Arés, and J. Gupta, *"Designs optimisations for concentrated solar systems using dilute nitride four-junction photovoltaics*," Photonics North 2015, Ottawa, June 9-11, 2015. *Invited.*

P. White, **P. Sharma**, P. Besson, M. Baudrit, S. Fafard, H. Schriemer, and Karin Hinzer, *"Effect of nonuniform illumination on triple junction solar cells under concentration,*" CPV 11, France, April 2015.

C. E. Valdivia, M. M. Wilkins, **P. Sharma**, R. Cheriton, A. Trojnar, G. Kolhatkar, A. Boucherif, A. Jaouad, B.Bouzazi, S.Fafard, V.Aimez, R. Ars, and Karin Hinzer, *"Towards CPV systems using Dilute Nitride containing 4-junction solar cells,*" CPV 11, France, April 2015.

P. Sharma, A. W. Walker, M. Wilkins, A. Trojnar, H. P. Schriemer, and K. Hinzer, *"Modeling nonuniform illumination and chromatic aberrations in multijunction solar cells,*" The Schalow Townes Symposium, University of Ottawa, September 2014.

K. Hinzer, M. M. Wilkins, A. H. Trojnar, **P. Sharma**, C.E. Valdivia, J.P.D. Cook, J.E. Haysom, H. Schriemer, and A.W. Walker, *"High Efficiency Multi-Junction Solar Cell Designs and their Integration in High Concentration Solar Systems,"* Photonics North 2014, May, 2014.*Invited.*

P. Sharma, J. F. Wheeldon, A.W. Walker, H. P. Schriemer, and K. Hinzer, *"Grid optimization for concentrator photovoltaic cells under non-uniform illumination using SPICE,"* Poster presentation, Graduate Research Day, University of Ottawa, March 2013.

P. Sharma, J. F. Wheeldon, M.D. Yandt, J. P . D. Cook and K. Hinzer , *"Comparative Analysis of Secondary Optics for Concentrated Photovoltaic Systems,"* Poster Presentation, Graduate Research Day, University of Ottawa, February 2012.

Acknowledgements

This doctoral work has been a very interesting and rewarding journey, thanks to the contributions of various individuals, who have been indispensable in bringing this research to light.

First and foremost I want to thank my supervisor Dr. Karin Hinzer. I appreciate all her contributions of time, technical guidance, and funding to make my Ph.D. experience productive and stimulating. I am grateful to her for accepting me as a graduate student, when I was 7 months pregnant and for supporting me to balance my work and family over the past 5 years. I am thankful to her for encouraging me to travel to several international conferences to present my work and to network with colleagues, which led to several job offers. I am also thankful for the excellent example she has provided as a successful woman engineer and professor, while being a wife and a mother at the same time.

I would like to thank Dr. Henry Schriemer, who is a member of my supervisory committee, for his technical insights and encouragement throughout my doctoral degree. His emphasis on a clear writing style and the suggestions on how to write impactful technical papers have improved my writing skills to a large extent.

I would like to gratefully acknowledge the advice and support of my supervisory committee members, Profs. Trevor Hall and Steven McGarry.

I am thankful to the SUNLAB modeling group - Matthew Wilkins, Chris Validivia Ross Cheriton, Anna Trojnar, Alex Walker and Ahmed Gabr, for their help with numerical modeling. Thank you for bearing with my million requests and questions, and for always taking the time to answer.

I am grateful to the past and present members of SUNLAB for their help, particularly Jeff Wheeldon, Viktar Tatsiankou, Richard Beal, Joan Haysom, Francine Proulx and Patrick White. Many thanks to John Cook for performing all the on-sun measurements in the harsh, Ottawa winters.

Thanks to our collaborators at the Université de Sherbrooke for all the insightful discussions on the 4CPV project and to LPI for providing CAD files for the Fresnel Köhler system. I am grateful for the financial support provided by Natural Sciences and Engineering Research Council of Canada (NSERC) and Ontario Graduate Scholarship (OGS). Many thanks to CMC for providing access to Sentaurus and Zemax software.

I am grateful to my parents who brought me up with a love for science and encouraged me to pursue my dreams, no matter how difficult it seemed. Thanks to my Dad for always believing in me, my Mom for pushing me to do the impossible and, to my younger brother for his support. I am very grateful to my parents-in-law for supporting me in this endeavor and taking care of the little ones, while I was away writing this thesis. My heartfelt thanks goes to my daughter, Suhana, and my infant son, Rishabh, for brightening my days with their infectious smiles!

Last but not the least, I would like to thank my best friend, my soulmate, my greatest critic, my husband - Paramesh, for his unconditional and unwavering support and encouragement to pursue this dream and for taking care of our kids while I was working. Thanks for hearing me out when I was frustrated, for sharing my excitement when I was thrilled, for motivating me in low tides and for being the rock I could always lean on.

Table of Contents

List of Tables

List of Figures

Nomenclature

Abbreviations

1-D	One-dimensional
2-D	Two-dimensional
3-D	Three-dimensional
3JIMM	Three-junction lattice-mismatched, inverted metamophic
3JLM	Three-junction, lattice-matched
4JLM	Four-junction, lattice-matched
X	Concentration ratio
AM	Air mass
ARC	Anti-reflective coating
CPV	Concentrated photovoltaic
EQE	External quantum efficiency
F-K	Fresnel Köhler
F-TP	Fresnel truncated pyramid

HCPV	High concentration photovoltaic
IQE	Internal quantum efficiency
LCOE	Levelized cost of energy
LCPV	Low concentration photovoltaic
LR	Learning rate
MJSC	Multijunction solar cells
OTF	Optical transfer function
PAR	Peak-to-average irradiance ratio
PMMA	Polymethylmethacrylate
POE	Primary optical element
PV	Photovoltaic technology
SC	Subcell
SOE	Secondary optical element
SPICE	Simulation Program with Integrated Circuit Emphasis

Mathematical Symbols

α	Acceptance half-angle
η_c	Coupling coefficient
η_{opt}	Optical efficiency
ϕ_0	Optical power

ϕ_l	Optical power at long wavelength
ϕ_s	Optical power at short wavelength
θ_{sun}	Solar half-angle
$A_{entrance}$	Area of the entrance aperture
A_{exit}	Area of the exit aperture
E_g	Bandgap
f_0	Focal length
FF	Fill-factor
I_0	Reverse saturation current
I_d	Dark current
I_{mpp}	Current at maximum power point
I_{sc}	Short-circuit current
J_d	Dark current density
J_{sc}	Short-circuit current density
L_f	Finger length
L_f	Finger width
m	Slope of linear profile
n_C	Refractive index of the material at 656.3 nm
n_d	Refractive index of the material at 589.67 nm
n_F	Refractive index of the material at 485.1 nm
P_{Max}	Maximum power point
r_j	Radius of the j^{th} zone

R_L	Lateral resistance
R_{se}	Electrode resistance
R_{Sheet}	Sheet resistance
R_{sh}	Shunt resistance
R_s	Series resistance
S_f	Finger spacing
Seg_N	Segment number
T_{ref}	Reference temperature
V_{mpp}	Voltage at maximum power point
V_{oc}	Open-circuit voltage
Xti	Temperature coefficient of saturation current
η	Efficiency
λ	Wavelength
μ	Carrier mobility
ϕ	Incident photon flux
D	Diffusion coefficient
d	Discount rate
G	Generation rate
h	Planck's constant
J	Current density
k_b	Boltzmann's constant
q	Electronic charge

Q_y	Annual energy output
R	Reflection
T	Temperature
T	Transmission
U	Recombination rate
Y	Analysis period

Chapter 1

Introduction

To myself I am only a child

playing on the beach, while

vast oceans of truth lie

undiscovered before me.

Issac Newton

With the rising cost of fossil fuels and increasing concerns about climate change, a significant amount of effort is being made to use renewable energy sources for energy generation. Solar energy, being ubiquitous and clean, has attracted significant attention as a viable renewable energy source for the past half century and continues to be a major player in the renewable energy market. Solar irradiance delivers 3.9×10^{24} Joules of energy to the Earth over the course of a year, enough to satisfy the planet's electricity demand many times over [1]. Therefore, solar energy is considered a major player in the renewable industry domain. Majority of solar energy conversion is being done by using photovoltaic

(PV) technology which allows for direct conversion of sunlight to electricity. PV technology has undergone massive improvements over the past three decades with total worldwide deployment risen to more than 170 GW [2]; the conventional silicon-based solar cell being the heart of the technology. However, with the efficiency of conventional flat-panel PV plateauing closer to the maximum theoretical limit, there is an increasing demand to identify other potential PV technologies, which promise high efficiencies at low costs. Several new technologies have emerged as a result, including the multicrystalline silicon, the thin film technology, and the multijunction solar cell technology. Figure 1.1 shows the cell efficiencies of some of these technologies under 1000 W/m^2 irradiation [3]. The efficiencies of single-junction based technologies are limited to $< 30\%$, approaching to the theoretical maximum of 33% [4]. The maximum efficiency of a crystalline-silicon solar cell is 25% obtained using the silicon material with silicon based module efficiencies peaking at 22.9%.

Of these PV technologies, the highest efficiency has been reported with the multijunction solar cell (MJSC) technology. This technology utilizes a broader spectrum for solar energy conversion and has shown immense efficiency improvements over the past decade. The promise of multijunction technology, however, falls flat in terms of the marketability in the flat panel PV market. Large size PV panels based on multijunction solar cells are not feasible due to their excessive manufacturing costs. In order to curtail this cost, the idea of using inexpensive optics to focus light on a smaller area, high-efficiency, multijunction solar cell has thus garnered the attention of PV industry, giving birth to the concentrated photovoltaic (CPV) technology. A brief chronological review of the CPV technology is presented in the following section, followed by the economics governing the CPV.

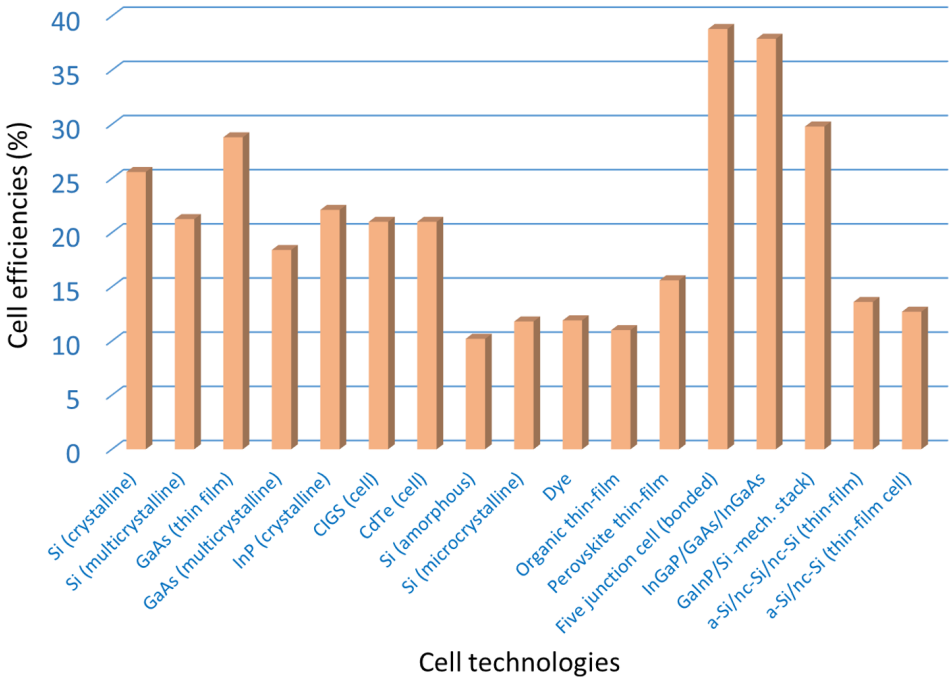

Figure 1.1: *Terrestrial cell efficiencies measured under the global AM1.5 spectrum at a cell temperature of* $25^{\circ}C$*. Data obtained from [3]. The five-junction wafer bonded technology shows the highest efficiency at 1 sun =* $1000\ W/m^2$*.*

1.1 Brief history and current status of CPV

Driven by the oil-crisis, the CPV technology was initially developed using concentrator silicon cells by National Sandia Laboratories in 1976 [5], with a target to compete with conventional fossil-fuel-based power plants. The first CPV systems used Fresnel lenses mounted on a two-axis tracking system [6]. With efficiencies ranging from 19 to 27% [7], concentrator cells were being developed all over the world. Notably, a 350 kW advanced version of the Sandia concentrator was installed in 1981 in Saudi Arabia for demonstration purposes. Many companies in the United States such as Boeing, Motorola, RCA, Spectrolab, General Electric and academic groups at Stanford, Purdue and Arizona State made an effort to develop CPV systems [8]. However, the discovery of new fossil fuel sources, leading to the plunging oil prices, decelerated the development of CPV.

In parallel, however, the need to address and mitigate global warming, and develop clean, renewable energy sources became the main driver for the development of flat-panel PV technology [8]. PV emerged as a viable power source for remote, inaccessible areas, and a subsidized grid connected market emerged for rooftop PV applications [9]. Still, the high cost ratio of CPV in comparison to flat panel solar cells curbed the market penetrability of CPV systems. By the early 1990s there were only a few dedicated companies which continued to pursue CPV.

The interest in CPV technology regained momentum with the development of high-efficiency, multijunction solar cells. These solar cells were primarily developed for space applications [10], [11]. However, the high-cost per unit area of these cells made them a befitting candidate for CPV applications as well [8]. While the silicon solar cells were

used for lower concentration (<40 times) (LCPV) applications, the high-efficiency multi-junction solar cells found their niche in high-concentration (>300 times) (HCPV) applications [12], [13]. More accurate knowledge of the direct normal resource further aided in the development of CPV and also proved beneficial for other PV technologies. It was found that in regions with a good solar resource, the annual energy available to a two-axis tracking concentrator is actually greater than stationary systems even with flat-plate systems [14].

In the mid 2000s, with the cost of PV plateauing, research funding, both industrial and academic, was directed to CPV, which offered the promise of a faster cost reduction than flat-plate PV [9], [15]. As a result, numerous start-ups dedicated to CPV emerged between 2005 and 2014 leading to a significant increase in installed CPV capacity.

Figure 1.2 shows the worldwide installed HCPV capacity over the past decade, as obtained from a recent report by National Renewable Energy laboratory (NREL) and the Fraunhofer institute for solar energy systems.

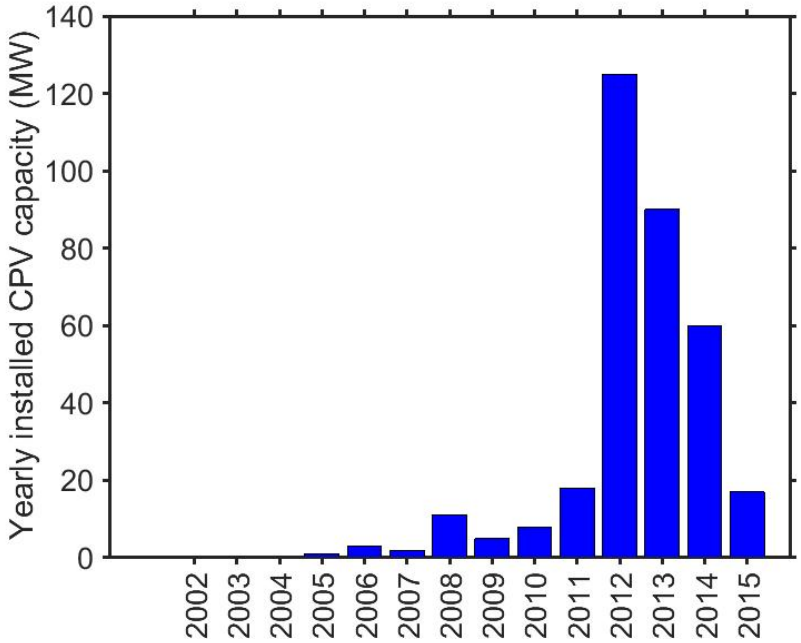

Figure 1.2: *Highly concentrated photovoltaic installed capacity based on data from latest report by Fraunhofer and NREL [16].*

CPV industry has seen its share of ups and downs in the past five years with yearly installed deployments peaking to 120 MW in 2012 alone and declining to 20 MW in 2015 [16]. The significant decline in CPV deployments is primarily attributed to the dramatic reduction in prices of silicon technology [17].

1.2 Economics of CPV

With a deeper technical understanding of the technology, the cost estimation for CPV deployment can be performed reliably. In order to project system costs over the useful lifetime of a CPV system, a metric called the levelized cost of energy (LCOE) is primarily

used. LCOE is the lowest price at which energy must be sold for an project to recover its expense and is used for comparison of alternative energy technologies. LCOE is determined by taking the ratio of the sum of the expected costs, discounted over the life of the project and the lifetime expected energy production, to provide the averaged lifetime cost of producing electrical energy in \$/kWh. It can be calculated by using the following equation [18]:

$$LCOE = \frac{\text{Total life-cycle costs}}{\sum_{y=1}^{Y} Q^y/(1+d^y)} \tag{1.1}$$

where Q^y is the energy output for the year y, d is the discount rate, Y is the analysis period.

LCOE predictions vary depending on the capital, operational and maintenance costs, the learning rate [19], and the atmospheric conditions [20]. In order achieve 10 MW_p power at 1000 suns the nominal cost of a CPV plant was determined to be \$2.6/W [21] a decade ago. This cost can further be reduced by applying a learning rate model as follows:

$$\frac{C}{C_0} = \left(\frac{M}{M_0}\right)^{-LR} \tag{1.2}$$

where C_0 is the cost of producing M_0, the cost, C, of a new production M is calculated using its learning rate (LR), implying that if the learning rate is high, the cost of new productions will be reduced. Based on a study done by our group at SUNLAB, a learning rate of 18% has been predicted for CPV [19]. This predicted learning rate for CPV is higher than the learning rates of concentrated solar power (11%) and traditional photovoltaic (14%)

technologies. Learning rate is influenced by better system efficiencies as well as more efficient deployment techniques. Figure 1.3 shows the consistent decline in CPV system prices over a period of 6 years [19]. A higher learning rate implies that the LCOE of CPV will reduce faster than PV and marketability of CPV will further increase making it more competitive with the flat-panel market.

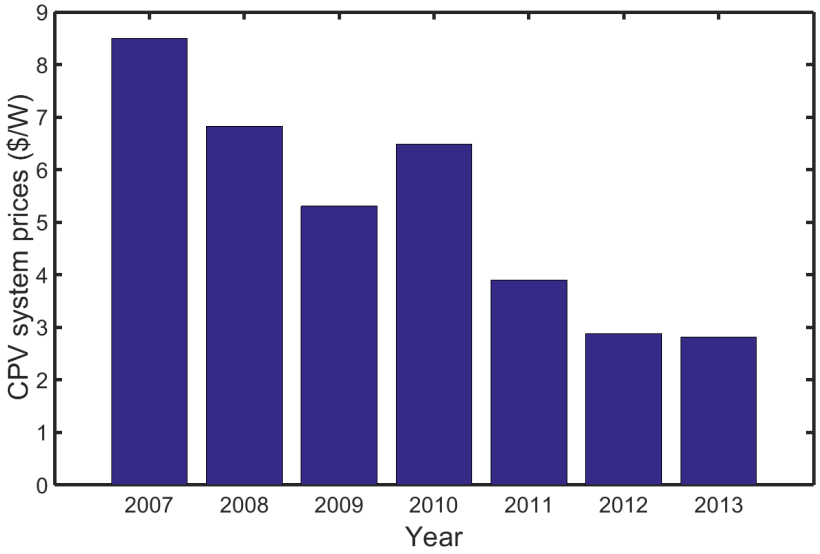

Figure 1.3: *CPV system prices adapted from [19] shown in United States dollar per watt ($/W).*

For high concentration PV systems, an LCOE of $0.14/kWh has been suggested while for low concentration systems, the LCOE has been reported to be $0.24/kWh [22]. A study done in Spain suggests that the LCOE of CPV may be lower than PV in certain geographical areas with high solar insolation [23]. It has also been suggested that for a fixed module price, module efficiency directly affects the LCOE. This implies that higher efficiency systems lower the LCOE even for the same module price [18]. The plunging prices of oil and that of silicon, however, have impacted CPV module production for the past two

years and may affect the learning rates for this technology. Even with the uncertainties in the current market, with the continued advancement in the development of high-efficiency cells, there is still a potential for achieving additional cost reductions.

1.3 Components of a CPV system

While cell efficiency is the main driver to achieve cost-reductions using CPV, other CPV system components also contribute to reducing the LCOE. Components within a CPV system vary significantly due to the availability of a plethora of optical designs and concentrator cells. However, most systems consist of the following main components:

1. Concentrator solar cells: Owing to their high-efficiencies, multijunction solar cells are primarily used for HCPV, while the use of silicon-based concentrator cells is limited to LCPV applications. Concentrator cell efficiencies exert a direct impact on CPV system efficiencies and therefore, are a major factor in lowering system costs. Most highly-concentrated commercial systems today are composed of three-junction solar cells with monolithic designs but newer architectures are also emerging.

2. Concentrating optics: A variety of optical architectures exist for concentrators, making it challenging to optimize the concentrator cells for every optical system. Typical architectures are either refractive (lens-based) or reflective (mirror-based). Figure 1.4 (a) shows a Fresnel lens used to concentrate sunlight onto a smaller concentrator solar cell. In some cases, a secondary optical element is also included in a lens-based design. A two-stage, Cassegrain mirror based design [24] is shown in Figure 1.4 (b).

Sunlight falls on the primary mirror and is reflected to a secondary mirror. The light reflected from the secondary mirror is focused on to the concentrator solar cell. While minimizing the number of optical system components would aid in cost reduction, the performance of the complete system is equally important, so as to extract maximum efficiencies from multijunction solar cells.

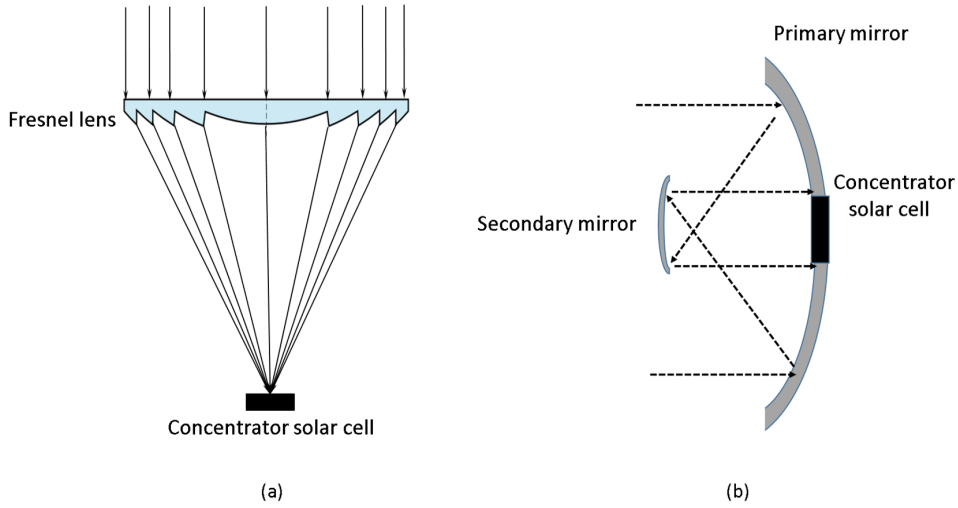

Figure 1.4: *(a) A refractive concentrator using a Fresnel lens as the focusing optical element, and (b) an example of a Cassegrain optical design using primary and secondary mirrors to focus light on a concentrator solar cell.*

3. Receivers: The solar cell and all its associated components such as the by-pass diode, the electrical connectors, and sometimes the secondary optics, are assembled together along with the heat-sink, to form a receiver. Figure 1.5 shows a CPV receiver with a multijunction solar cell and the electrical connections. Bypass diodes are typically added to prevent hotspots due to shading.

4. Modules: A CPV module consists of: (i) receivers along with opto-mechanical com-

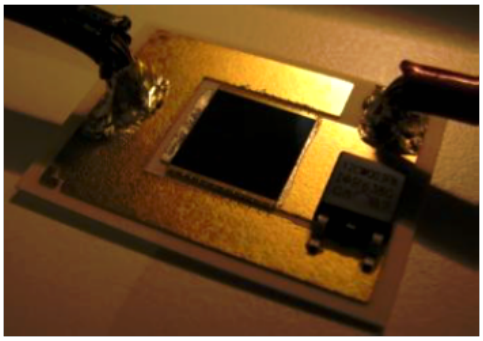

Figure 1.5: *A CPV receiver with a multijunction solar cell, a bypass diode, and electrical connections.*

ponents which focus light onto the solar cell, (ii) electrical connections to connect each receiver, (iii) thermal conduits to extract heat out of the system and (iv) protective shells to prevent moisture and other environmental elements from affecting the receiver.

5. Trackers: Trackers are mechanical, moving structures which follow the sun. CPV modules accept the direct component of sunlight and have to be oriented appropriately to track the sun. Multiple modules are mounted on a tracker forming a CPV system. A reduction in tracking accuracy limits the collected energy in a CPV system. Figure 1.6 shows a test site with several CPV modules installed on a tracker at the University of Ottawa, maintained by our research group, the SUNLAB.

1.4 Thesis motivation

The cost-effectiveness of CPV with multijunction solar cells is realizable only at high concentrations. However, designing systems above 500× concentration comes with a number

Figure 1.6: *An installed CPV system at our solar test site at the University of Ottawa.*

of challenges. Some of the most important technical issues affecting CPV performance include:

1. Series resistance losses: The effect of series resistance is more pronounced at high concentrations due to the higher system currents which lead to greater Ohmic losses. Therefore, solar cells have to be optimized to minimize series resistance at specific concentrations.

2. Non-uniform spatial and spectral profiles: Concentrating optics often generate non-uniform illumination profiles, both spatially and spectrally. Such profiles can cause excessive current generation in localized areas, leading to localized current mismatch, hotspots and increased series resistance losses.

3. Misalignments and optics tolerances: Misalignments of the optics with respect to the

cell can cause deterioration in cell efficiencies. Since CPV utilizes only the direct component of sunlight, solar tracking is indispensable. However, proper system design can reduce sensitivity to tracking errors, vital to maximizing energy conversion efficiency.

4. Temperature: CPV systems operate at much higher temperatures than flat-plate PV. Higher temperatures affect material properties and can diminish system efficiencies. Thorough understanding and quantification of the effects of high temperature are very important to obtain maximum system efficiencies.

Due to the above factors, it becomes quite challenging to predict the performance-efficiency of CPV systems. Most concentrator cells are characterized under standardized uniform illumination and temperature conditions. However, in practicality, the cells are subjected to nonuniform illumination and temperature profiles. CPV optics also exert a significant influence on system efficiencies. Transmission losses, chromatic aberrations and losses due to current mismatch greatly affect the performance of multijunction solar cell, therefore affecting CPV system efficiencies. New approaches to the design of the cell and the optics are therefore required in order to achieve high module efficiencies at high concentrations. Hence, evaluation, quantification and mitigation of these effects requires a thorough quantitative analysis which can lead to the enhancement of CPV system efficiencies and successful development and deployment of CPV systems worldwide.

Modeling and simulation provide powerful tools to attain these objectives. Reliably developing models for such devices and systems is an important part of photovoltaic systems research. The goals of this thesis work are motivated by the need for methodical studies

and experimental work that describe various physical processes affecting the performance of high-concentration photovoltaic systems. In this thesis, several new methods of modeling important effects in multijunction solar cells are proposed for quantitative analysis with an ultimate aim to enhance overall system efficiencies. A distributed circuit modeling technique, integrated with an opto-electrical approach, to understand and quantify the effects of realistic conditions on multijunction solar cells is proposed and implemented. Industry accepted tools have been used for simulations, and experimental results are presented, where feasible and attainable, within the facilities at the University of Ottawa.

In summary, the main objectives of this thesis can be briefly stated as follows:

- Quantification and comparative analysis of efficiency losses due to nonuniform illumination profiles under concentrations for various multijunction solar cell designs considering the impact of series resistances in a distributed manner.

- Identification and implementation of loss mitigation techniques to obtain efficiency enhancements under uniform and nonuniform illumination conditions.

- Analysis and comparative evaluation of different lens-based CPV optics and quantification of optical efficiency for each design.

- Integrated optimization of multijunction solar cell designs with CPV optics to determine loss penalties due to nonuniformities and to determine system efficiencies under realistic illumination conditions.

- Evaluation of effects of temperature nonuniformities on cell efficiency.

1.5 Thesis Outline

After this introductory chapter which provides a motivation and context for this thesis, the remainder of this thesis is divided into 5 chapters followed by a conclusion. The outline of the thesis is as follows:

Chapter 2 discusses, briefly, the theory of operation of solar cells, electrical parameters which define the solar cell and state-of-the-art, high-efficiency, multijunction solar cells. Numerical modeling of three and four-junction solar cells using drift-diffusion simulators is discussed, and simulation results are presented.

Chapter 3 deals with the distributed circuit modeling technique for simulating solar cells, beginning with a historical review of electrical circuit models. A distributed resistance model parametrized for three and four-junction solar cells is proposed and is applied to the analysis of nonuniform, distributed effects. The effect of luminescent coupling on multijunction cells, specifically under nonuniform illumination profiles, is also studied.

Chapter 4 is devoted to the design of optical systems using a commercially available ray-tracing software. A detailed analysis of Fresnel lens-based designs at two concentrations, with and without the secondary optical element, is presented. Simulation results from a case study performed with an advanced, industrial, Fresnel-Köhler CPV system are also discussed.

In Chapter 5, an integrated opto-electrical modeling approach is proposed. Ray tracing is combined with distributed circuit modeling, in order to independently quantify the losses due to spectral and spatial nonuniformities. Optimization of designs is performed

and manufacturing tolerances are determined. On-sun, acceptance angle measurements from similar refractive systems are also presented.

The main emphasis of Chapter 6 is to determine the effect of temperature on CPV systems. Temperature effects are quantified via both modeling and experimental techniques, specifically for three-junction monolithic design and single-junction, dilute-nitride based cells. The effect of nonuniform temperature distribution is also studied for a four-junction solar cell design.

Finally, Chapter 7 summarizes the contributions of this thesis and also presents ideas for future work.

Chapter 2

Concentrator solar cells

2.1 Introduction

Concentrator solar cells have definitive design requirements tailored to attain maximum efficiency under direct insolation at a specific concentration. The use of silicon concentrator cells is typically restricted to low concentration applications while multijunction solar cells dominate the high-concentration market. This is because MJSCs have achieved the highest efficiencies among the current photovoltaic technologies with reported cell efficiencies exceeding 46% [3]. Such high efficiencies are primarily attributed to the reduction in thermalization and absorption losses in solar cells, caused due to the additional p-n junctions. The initial development of MJSCs was targeted towards space applications, where cell cost was not the factor limiting usability. In the flat-panel market, however, the prospect of using MJSCs was considered marginal, due to the prohibitive costs of manufacturing large active area cells. Hence, the idea of using smaller cells, with inexpensive optics for focusing

sunlight, received significant attention and led to the development of concentrator MJSCs for terrestrial applications.

In this chapter, firstly the solar resource is described, followed by a brief theory on the operation of a solar cell. Thereafter, loss-mechanisms in a solar cell and solar cell electrical characteristics are discussed. For a detailed discussion on the theory of semiconductors and the working of a solar cell, the reader is referred to [25] and [26]. Since the focus of this thesis is on highly concentrated PV systems, silicon-based CPV systems are not included. State-of-the-art MJSC technologies and challenges faced for high concentration applications are discussed. Numerical modeling results for three and four-junction solar cells are detailed towards the end of the chapter.

2.2 The solar resource

In order to understand the working of a solar energy conversion device, it is imperative to understand the solar resource. Two important parameters which influence the working of a PV device are: the amount of incident power, referred to as *irradiance*, and the spectral characteristics of sunlight. Outside the earth's atmosphere the solar irradiance value is 1365 W/m^2, referred to as the solar constant [27]. After being filtered through the atmosphere this value is reduced to 1000 W/m^2. The relationship between solar irradiance and solar spectrum is established by the *air mass*. Air mass (AM) refers to the amount of air, a beam of sunlight must pass through before reaching the PV device. It can be calculated using the following equation:

$$AM = \frac{1}{\cos\theta} \tag{2.1}$$

The angle, θ, is the angle which the sun makes with the normal to the earth. This angle is assumed to be 48.19 ° for the purposes of standard solar measurements and the spectrum is thus referred to as the AM1.5 spectrum. Scattered sunlight that reaches the earth's surface is called diffuse radiation, while parallel rays that are incident on earths surface are referred to as direct radiation. Therefore at a given air mass, two components, direct and diffuse, constitute the global spectrum. The direct component of the AM1.5 spectrum is typically used to characterize concentrated PV systems, and is denoted as AM1.5D, and for flat-plate photovoltaic systems the total global AM1.5 spectrum is used as the standard spectrum and is denoted as AM1.5G. Figure 2.1 shows both the AM1.5G and AM1.5D spectrum as a function of wavelength [28]. The troughs in the solar spectrum are attributed to the absorption bands of atmospheric elements such as water, carbon-dioxide, ozone and oxygen. Complete attenuation below 300 nm is primarily caused due to the presence of ozone.

The solar spectrum determines the number of photons which can contribute to photocurrent in a solar cells. The wavelength dependent spectrum can be converted into photon energy using the following relationship:

$$\text{Photon Energy} = \frac{hc}{\lambda} = \frac{1.239}{\lambda(\text{in } \mu\text{m})}[\text{in eV}] \tag{2.2}$$

where λ is the wavelength, h is Planck's constant and c is the speed of light. A photon at a wavelength of 550 nm thus has an energy of approximately 2.2 eV. Whether this energy is

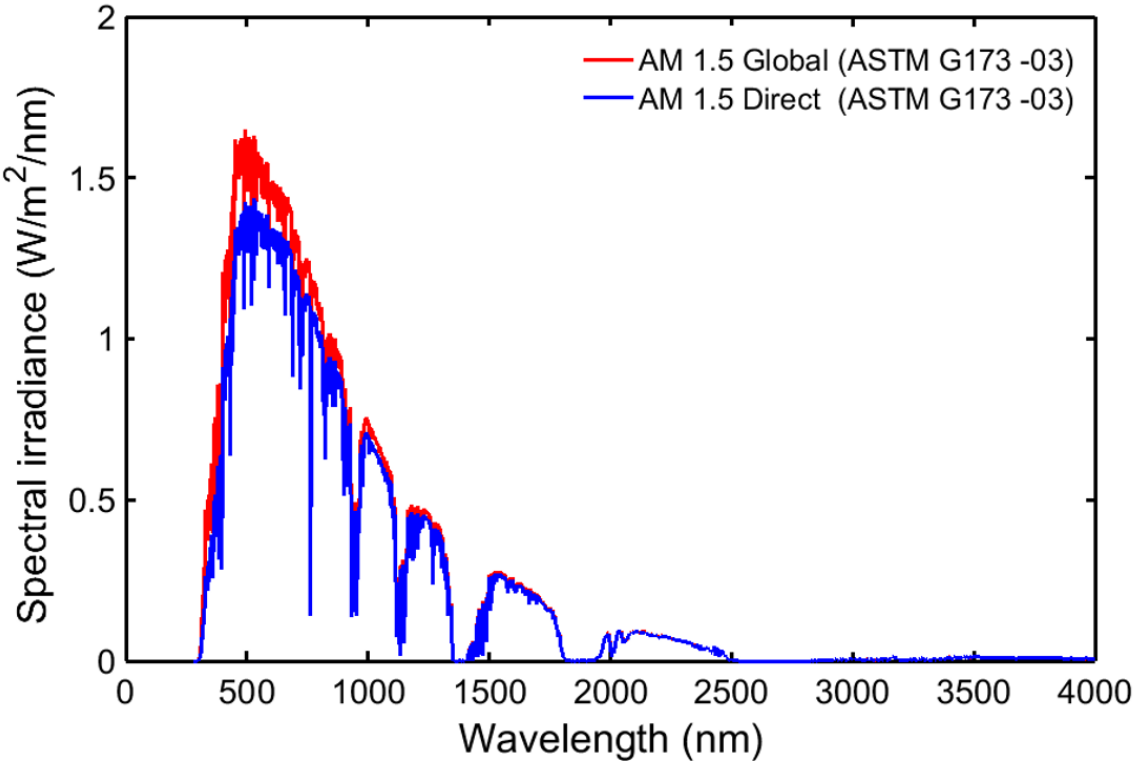

Figure 2.1: *Air mass (AM) 1.5 spectrum shown as a function of wavelength. AM1.5D refers to the direct component of solar irradiance while AM1.5G refers to the global irradiance including the diffuse component. Concentrators can only focus the direct component of solar irradiance.*

sufficient to excite an electron from its ground state or not is determined by the bandgap of the material(s). The principle of operation of a PV device including the process of photon absorption is briefly explained in the following section and can be found in detail in [25].

2.3 Solar cell : theory of operation

A typical solar cell consists of a *p-n* junction made up of semiconductor material(s) with specific bandgap(s). The operation of a solar cell is guided by two main mechanisms:

generation and *recombination* [25]. The process of generation refers to the generation of photocurrent in a solar cell and is composed of two main processes: absorption of photons and collection of charge carriers. Photons with energy above the bandgap get absorbed leading to the generation of an electron-hole pair, which is spatially separated by the electric field across the p-n junction. This charge carrier separation leads to a flow of photocurrent. An electron-hole pair generated closer to the surface recombines quickly, and does not contribute to the photocurrent. While the generation rate of electron-hole pairs and the probability of collection of the carriers determines the photocurrent through the cell, the photovoltage is determined by the wavelength of incident light and the bandgap of the solar cell material.

2.4 Solar cell characteristics

2.4.1 Quantum Efficiency

Quantum efficiency refers to the probability of collection of the charge carrier when a photon of a given energy is incident on it. If all the minority charge carriers generated by photons of a specific energy are collected, the quantum efficiency at that wavelength is 1 [25]. In reality, recombination losses reduce the collection probability and therefore the quantum efficiency of a solar cell. Quantum efficiency may be defined either by the *internal quantum efficiency* (IQE) or the *external quantum efficiency* (EQE). The EQE refers to the quantum efficiency of the cell when the reflection (R) and transmission (T) losses are taken into account while the IQE ignores these losses and so the IQE is typically greater

than the EQE of the cell. The IQE can be calculated from the EQE using the following equation:

$$IQE = \frac{EQE}{1 - R - T} \tag{2.3}$$

Figure 2.2 shows the external quantum efficiency of Si, GaAs and Ge solar cells [29]. It can be seen that GaAs has a high EQE for the high photon region of the solar spectrum. While GaAs and Si both absorb photons with lower wavelengths, Ge absorption extends far into the infra-red region. The EQE gives an idea about the bandgap of the device as well as the photocurrent obtainable under a particular spectrum.

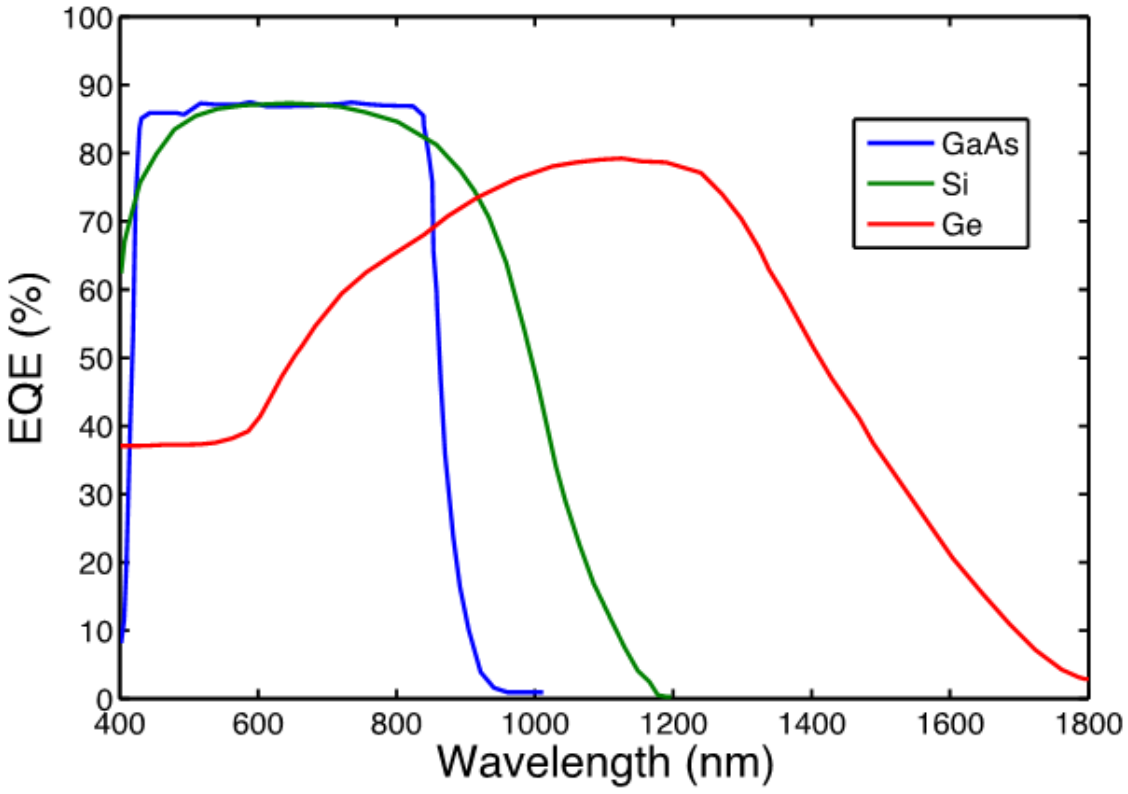

Figure 2.2: *External quantum efficiency of a Si, Ge and a GaAs solar cell. Reproduced with permission from [29].*

2.4.2 Photocurrent

If the terminals of the solar-cell are connected under illumination, the photocurrent thus generated is referred to as *short-circuit current*. The photocurrent density, J_{sc}, is related to the incident spectrum and the quantum efficiency by the following relation:

$$J_{sc} = q \int \phi(\lambda).EQE(\lambda)d\lambda \tag{2.4}$$

where q is electronic charge, $\phi(\lambda)$ is the incident photon flux and λ is the wavelength.

2.4.3 Dark current and open-circuit voltage

Under dark conditions, solar cells follow diode characteristics. Under an applied bias, the current generated between solar cell terminals flows in opposition to the photocurrent. This is referred to as the *dark current*. The dark current density, J_d at temperature T, for an ideal diode is given by:

$$J_d(V) = J_0(e^{qV/k_bT} - 1) \tag{2.5}$$

where J_0 is the saturation current, T is the temperature in Kelvin, and k_b is Boltzmann's constant.

The summation of the dark current and the photocurrent gives the overall current response of the solar cell as follows:

$$J(V) = J_{sc} - J_d \tag{2.6}$$

When the solar cell terminals are isolated, the potential difference across the cell is given by the *open-circuit voltage*. This can be calculated by:

$$V_{oc} = \frac{kT}{q} \ln \left(\frac{J_{sc}}{J_0} + 1 \right) \tag{2.7}$$

2.4.4 Current-Voltage characteristics

Electrically, a solar cell can be represented as a current source in parallel with an ideal diode as shown in Figure 2.3. The current-voltage (I-V) characteristics of a solar cell are represented by equation.

$$J(V) = J_{sc} - J_0(e^{qV/k_bT} - 1) \tag{2.8}$$

In the presence of parasitic resistances, namely the *series*(R_s) and the *shunt* (R_{sh}) resistances, the equation for a solar cell with area A becomes:

$$J(V) = J_{sc} - J_0(e^{q(V+JAR_s)/k_bT} - 1) - \frac{V + JAR_s}{R_{sh}} \tag{2.9}$$

The series resistance is attributed to the resistance of the metal contacts and the contact between the semiconductor material and the metal. The shunt resistance arises from current leakage around device edges. For an ideal cell, the series resistance is 0 and the shunt resistance is infinite.

Figure 2.4 shows the dark and illuminated I-V curves of a silicon cell generated using Simulation Program with Integrated Circuit Emphasis (SPICE) using circuit parameters

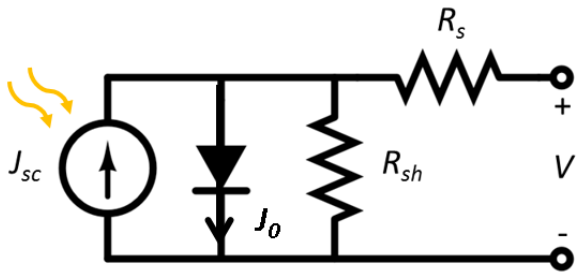

Figure 2.3: *Equivalent circuit of a solar cell including parasitic resistances.*

obtained from [30]. The short-circuit current is assumed to be positive and varies linearly with illumination. There is a net increase in the open-circuit voltage with an increase in illumination intensity.

2.4.5 Maximum power point, fill-factor and efficiency

The maximum power point of the solar cell is determined from the current-voltage characteristics where the product of current and voltage is maximized as given in equation 2.10.

$$P_{Max} = \text{Max}(I.V) \tag{2.10}$$

where I is the current, which can be determined from the current density times the area of the cell.

The fill factor defines the squareness of the IV curves and is calculated using equation 2.11.

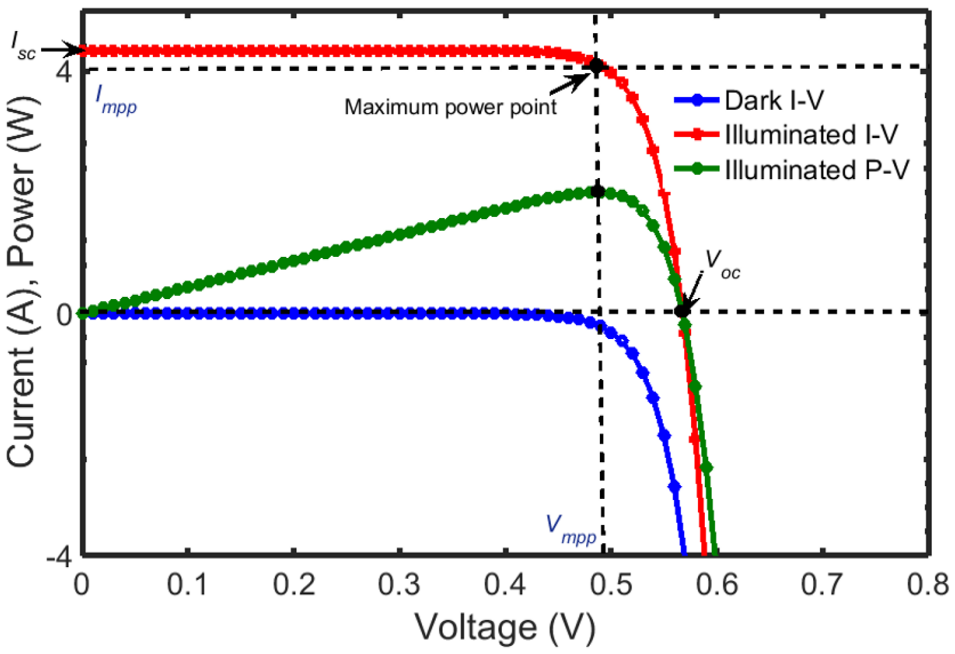

Figure 2.4: *Dark and illuminated current-voltage curves, and illuminated power-voltage (PV) curve of a silicon cell indicating the short-circuit current, the open-circuit voltage and the maximum power point. The curves have been generated using SPICE simulations for a silicon cell.*

$$FF = \frac{I_{mpp}V_{mpp}}{I_{sc}V_{oc}} \tag{2.11}$$

I_{mpp} and V_{mpp} refer to the current and voltage at the maximum power point. I_{sc} stands for the short-circuit current which can be obtained from the product of the short-circuit current density and the cell area.

The efficiency, η, of the solar cell is the ratio of the maximum power obtained to the incident power P_{in}.

$$\eta = \frac{I_{mpp}V_{mpp}}{P_{in}} \tag{2.12}$$

The efficiency, fill-factor, the short-circuit current and the open-circuit voltage constitute the four key performance parameters for a solar cell. The efficiency of an ideal solar cell should be 1, but loss penalties reduce this efficiency by a significant amount.

2.5 Loss mechanisms in solar cells

Solar cells suffer from various losses which reduce their efficiency significantly [26], [31]. In this section, the primary loss mechanisms are briefly described and various techniques, which have been used to mitigate these losses, are presented.

1. Non-absorption: The efficiency of a solar cell is strongly dependent on the material bandgap (E_g) as photons with energy below the bandgap ($E < E_g$) do not get absorbed as shown in Figure 2.5 (a). For a single-junction device under a fixed spectrum, there is an optimum bandgap where the efficiency reaches a maximum. For the standard AM1.5 spectrum according to the Shockley-Queisser limit, a maximum efficiency of 33% at a bandgap of 1.4 eV is theoretically predicted [4]. Hence, non-absorption of sunlight exerts a significant impact on the solar cell efficiency.

2. Thermalization: Photons with energies much greater than the bandgap ($E > E_g$) are strongly absorbed by the device with the excess energy above the bandgap lost as heat [26] as illustrated in Figure 2.5 (a).

3. Recombination: If the charge carriers recombine before reaching the solar cell contacts, the absorbed energy gets lost as a photon (*radiative*) or a phonon (*non-radiative*) or as kinetic energy to another free carrier (*Auger*). Recombination may

occur in the bulk material or at the surface. Techniques such as surface passivation and the use of back-surface field are often employed to reduce recombination [25].

4. Reflection: Fresnel reflections due to the air/semiconductor interface lead to substantial losses in a solar cell as shown in Figure 2.5 (b). These losses which are refractive index dependent can be minimized by using optimal anti-reflective (AR) coatings. The AR coating material and thickness is chosen for maximum photocurrent generation at relevant incident angles. In addition, a rear reflector is often used to increase absorption by reflecting the light into the cell for potential reabsorption.

5. Shading: Metallization of contacts leads to areas with no current generation. Contact patterns optimization is thus performed to minimize shading. Back contacted solar cells and transparent electrodes are also used to reduce shading losses.

6. Series resistance losses: Ohmic or resistive losses occur due to the photocurrent flowing through the device and the resistive metal contacts. These losses can be partly mitigated by optimized doping concentrations to improve carrier collection [25].

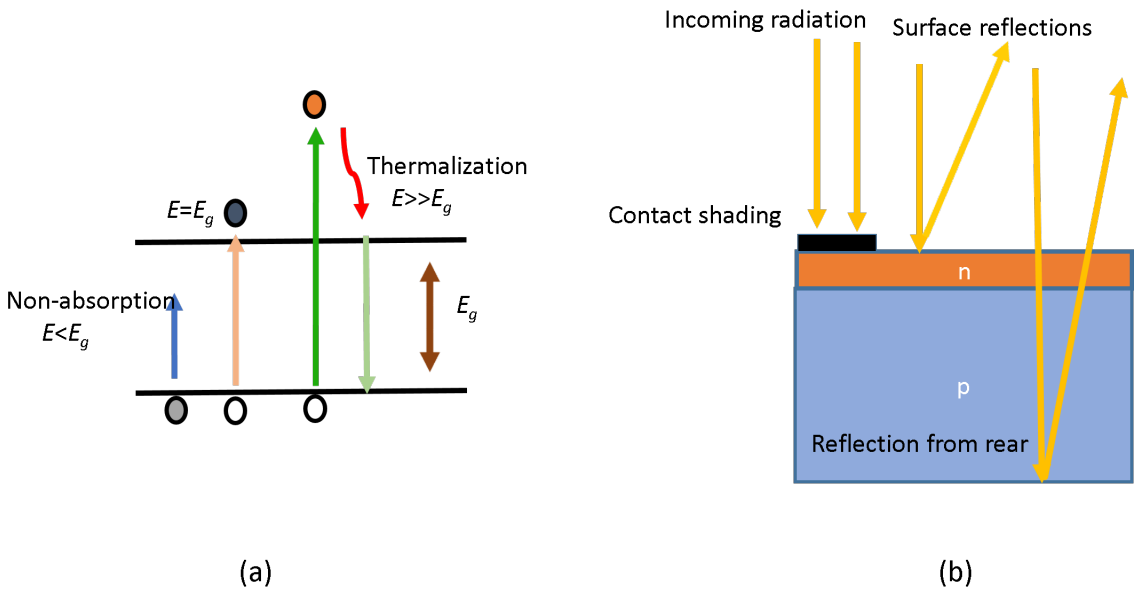

Figure 2.5: *(a) Thermalization and non-absorption in a photovoltaic cell and (b) optical losses due to contact shading and Fresnel reflections.*

2.6 Mitigating losses using multijunction solar cells

While single-junction solar cell efficiencies have been on the rise and are reaching closer to the theoretical maximum, a significant portion of the solar energy is wasted due to non-absorption or thermalization, as discussed in the previous section. Hence, using a broadband converter to absorb sunlight is a natural choice. Using multiple p-n junctions to absorb different portions of the solar spectrum has led to the development of what is termed as a *multijunction solar cell*. MJSCs have been realized by using a stacked, series-connected approach or an optically parallel, spectral-splitting approach. The series-connected approach dominates the commercial market and is the focus of this thesis. For

more details on the spectrum-splitting approach, the reader is referred to [32].

Series-connected MJSCs are typically composed of stacked p-n junctions of material with different bandgaps. The highest bandgap material is stacked at the top with the lower bandgap materials to follow [33]. Figure 2.6 shows a tandem MJSC with three junctions [34]. The highest bandgap material, stacked at the top, absorbs the shorter wavelengths from the solar spectrum while the longer wavelengths are absorbed by the bottom subcells. The higher bandgap materials remain transparent to the photons below their bandgap and transmit those photons to the lower bandgap material(s).

In addition to mitigation of absorption and thermalization losses, MJSCs also promise lower ohmic losses due to an overall reduction in photocurrent as compared to a single-junction solar cell. While three-junction or triple junction cells have entered the commercial market already, adding more junctions to improve efficiencies without increasing system cost is a target CPV industry is marching towards.

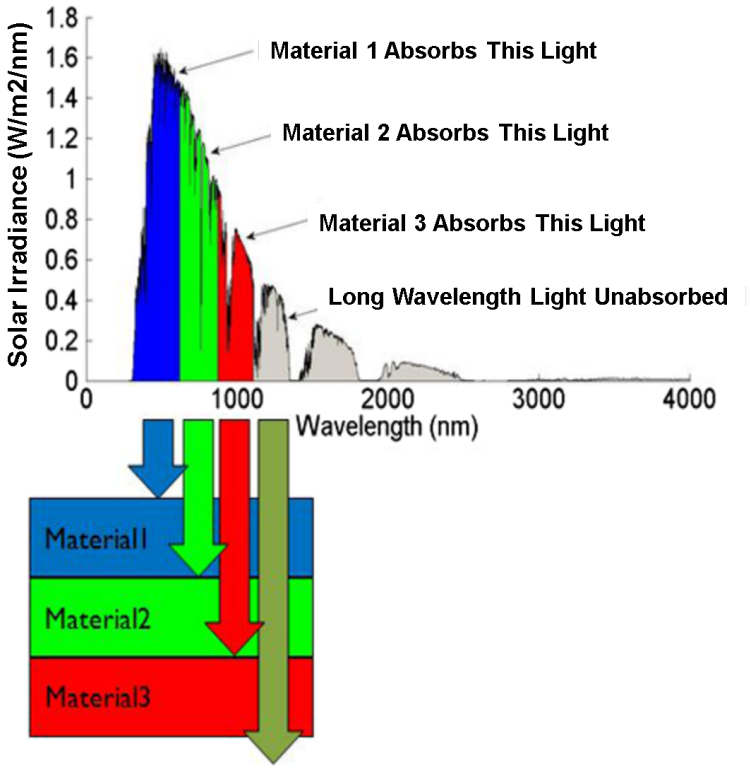

Figure 2.6: *A multijunction solar cell with three junctions absorbing different portions of the solar spectrum. Material with the highest bandgap is stacked on the top followed by a lower bandgap material. Reproduced with permission from [34].*

2.7 High-efficiency solar cell structures

2.7.1 Lattice-matched

A lattice-matched, monolithic structure is the most common design approach used by MJSC manufacturers primarily due to the ease of integrating different junctions using tunnel junctions. Three-junction, lattice matched designs are widely available with a typical structure composed of GaInP/GaAs/Ge materials. Greater than 41% device efficiency

has been achieved under concentration with this design [35]. A monolithic, three-junction cell is grown typically on Ge wafer using metalorganic chemical vapor deposition method. Since Ge is lattice matched to InGaAs and GaInP subcells, the growth is considerably free from defects. However,a less than optimal bandgap of Ge causes current overproduction and hence large current mismatch between the top two subcells and the Ge subcell.

Figure 2.7 (a) shows a typical three-junction, lattice matched MJSC with Ge bottom subcell. The corresponding equivalent circuit diagram is shown in Figure 2.7 (b). A triple junction solar cell is modeled by using a current source in parallel with two diodes for each subcell. The subcells are typically connected via low-resistance tunnel junctions (TJ). Parasitic series and shunt resistances are also typically included. Figure 2.7 (c) shows the current-voltage curves for each subcell as well as for the entire structure. While the top two subcells are current matched, the bottom subcell typically overproduces in a typical three-junction MJSC.

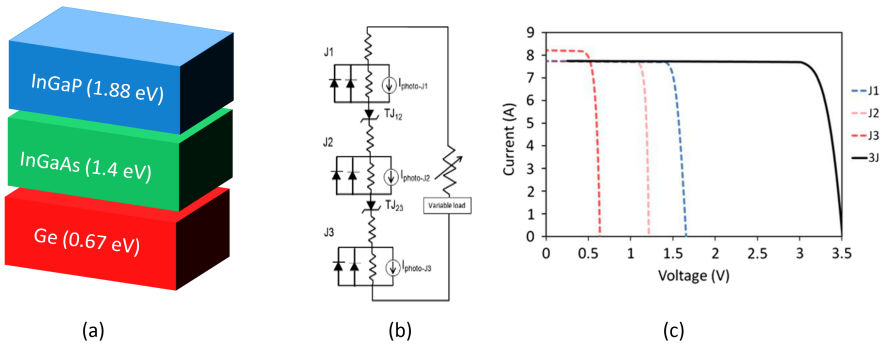

Figure 2.7: *(a) A lattice-matched, three-junction solar cell with Ge as the bottom subcell (b) The equivalent circuit diagram for a triple-junction solar cell. Photocurrent is modeled by a current source flowing in the opposite direction of the forward current flow of the diodes. Subcells are connected via tunnel junctions. (c) Current-voltage characteristics of the subcells within a triple-junction solar cell along with the overall current-voltage characteristics. Parts (b) and (c) reproduced with permission from [34].*

Although the three-junction designs are commercially available, there is a significant interest in adding more junctions to harness the solar spectrum more efficiently. Four junction cells promise $> 50\%$ theoretical efficiency under concentration. Monolithic four junction designs have been developed by adding another junction with a bandgap of 1eV above the Ge subcell.

Hence, four-junction monolithic designs are also making way through the efforts of companies such as Soitec, which in collaboration with the Fraunhofer institute holds the record of the highest efficiency solar cell thus far [36].

2.7.2 Upright and inverted metamorphic

The prime issue with the monolithic design is the lattice-matching constraint which limits the choice of materials required to manufacture MJSCs. Ge being the typical choice for a bottom cell, current mismatch cannot be avoided. In order to lower the current mismatch in the bottom subcell, one option is to lower the bandgap energies of the top two junctions. By changing the indium concentration, the bandgap of the top two subcells can be lowered. This, however, causes a lattice mismatch with the Ge subcell. Figure 2.8 shows the bandgap as a function of lattice constant [37]. Lattice mismatch with Ge can lead to dislocations which reduce carrier collection probability.

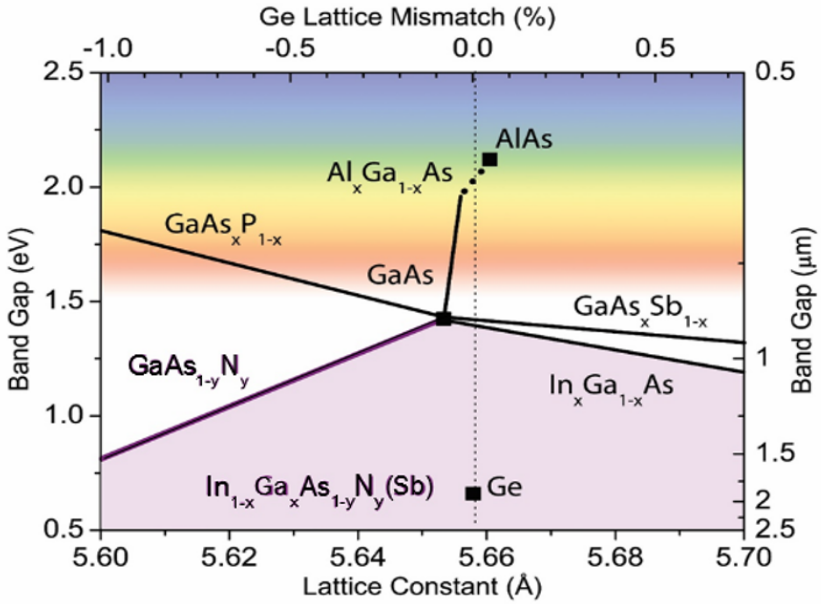

Figure 2.8: *Bandgap as a function of lattice constant for GaAs-based materials and related dilute nitrides at room temperature. Solid (dashed) lines indicate direct (indirect) bandgaps [37].*

Structures grown using lattice-mismatched materials are called *metamorphic* structures [38]. This approach offers access to bandgaps which encompass high irradiance

fragments of the solar spectrum, permitting new bandgap combinations in MJSCs, and increasing both theoretical and practical efficiency limits for concentrator solar cells [39]. Table 2.1 shows the optimum bandgap combination for a blackbody spectrum at 6000 K under concentration. The limiting efficiency in the unconstrained case is higher than that achievable using the series-connected configuration. This efficiency increase is more pronounced with an increase in the number of junctions.

Table 2.1: *Optimum bandgap combination for unconstrained and series-connected cells under a blackbody spectrum at 6000 K under concentration.*

No. of junctions	**Design**	**Optimal bandgap(s)**	**Limiting efficiency (%)**
1	Unconstrained	1.11	40.7
1	Series-connected	1.11	40.7
2	Unconstrained	0.77/1.70	55.8
2	Series-connected	0.77/1.55	55.5
3	Unconstrained	0.62/1.26/2.10	63.8
3	Series-connected	0.61/1.15/1.82	63.2
4	Unconstrained	0.52/1.03/1.61/2.41	68.7
4	Series-connected	0.51/0.94/1.39/2.02	67.9
5	Unconstrained	0.45/0.88/1.34/1.88/2.66	72.0
5	Series-connected	0.44/0.81/1.16/1.58/2.18	71.1
6	Unconstrained	0.40/0.78/1.17/1.60/2.12/2.87	74.4
6	Series-connected	0.38/0.71/1.01/1.33/1.72/2.31	73.4

Designs growth monolithically with lattice-mismatched materials have been referred to as *upright* metamorphic designs. Record efficiency of 41.1% at 454× concentration with a three-junction, upright, metamorphic cell has been reported [40].

The second strategy to achieve current matching can be by increasing the band gap of the bottom subcell. For the triple junction case, the Ge subcell can be replaced with a 1eV InGaAs bottom cell [41]. As shown in Figure 2.8, the lattice mismatch between GaAs and InGaAs (1eV) can be high in this case leading to threading dislocations and difficulty in fabrication. In order to avoid the problems associated with the growth of such a metamorphic structure, an *inverted* configuration has been developed. The top subcell is grown first followed by the bottom subcells. Figure 2.9 shows the upright and the inverted metamorphic design with transparent buffer layers included for transitioning from one lattice constant to the other. Highest efficiency of 44.4% at 302× concentration has been reported with a three-junction, inverted metamorphic design.

Both the upright metamorphic and inverted metamorphic designs have gained popularity in the past decade due to the freedom they offer in the choice of materials [39], [42]. Concentrator four junction metamorphic structures have also been developed with reported efficiencies of 45.7 ± 2.3% at 234 suns concentration under AM1.5D spectrum [43].

2.7.3 Wafer bonded structures

Another technique used to combine non-lattice-matched materials, without creating dislocations, is the wafer bonding technique [44], [45]. It allows for the integration of subcells from a dissimilar substrate into a single structure. The lattice-matching constraint is re-

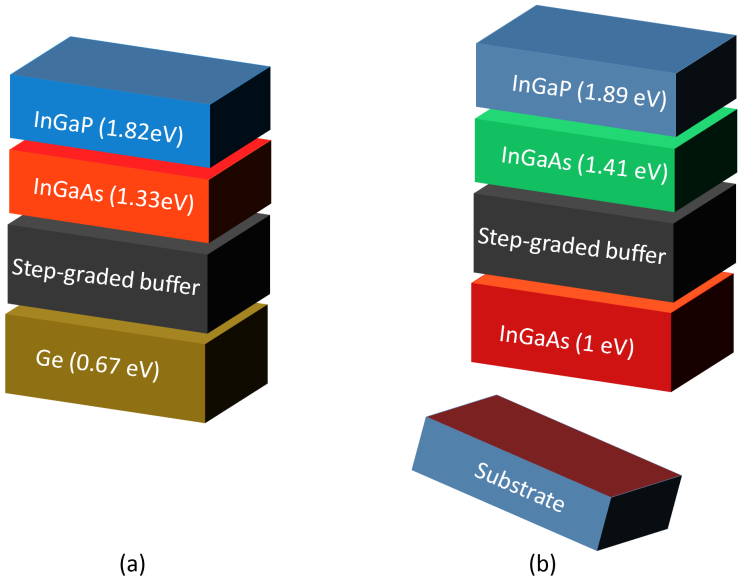

Figure 2.9: *(a) An upright metamorphic design with a buffer layer included for reducing lattice defects and (b) an inverted metamorphic design with a buffer layer. The growth direction in this case is from the top subcells to the bottom subcell.*

laxed making materials such as GaInPAs and Si, feasible to be used as 1 eV subcell in concentrator cells. The technique involves bringing two crystal structures, with low surface roughness, together to form atomic bonds. Two and three-junction wafer bonded structures have been realized with a efficiencies exceeding 30% [46]. An efficiency of >44% has been obtained with a four-junction solar cell with a $Ga_{0.51}In_{0.49}P$/ GaAs top tandem bonded to a $(Ga_{0.16}In_{0.84})(As_{0.31}P_{0.69})$/ $Ga_{0.47}In_{0.53}As$ bottom tandem solar cell [47] as shown in Figure 2.10.

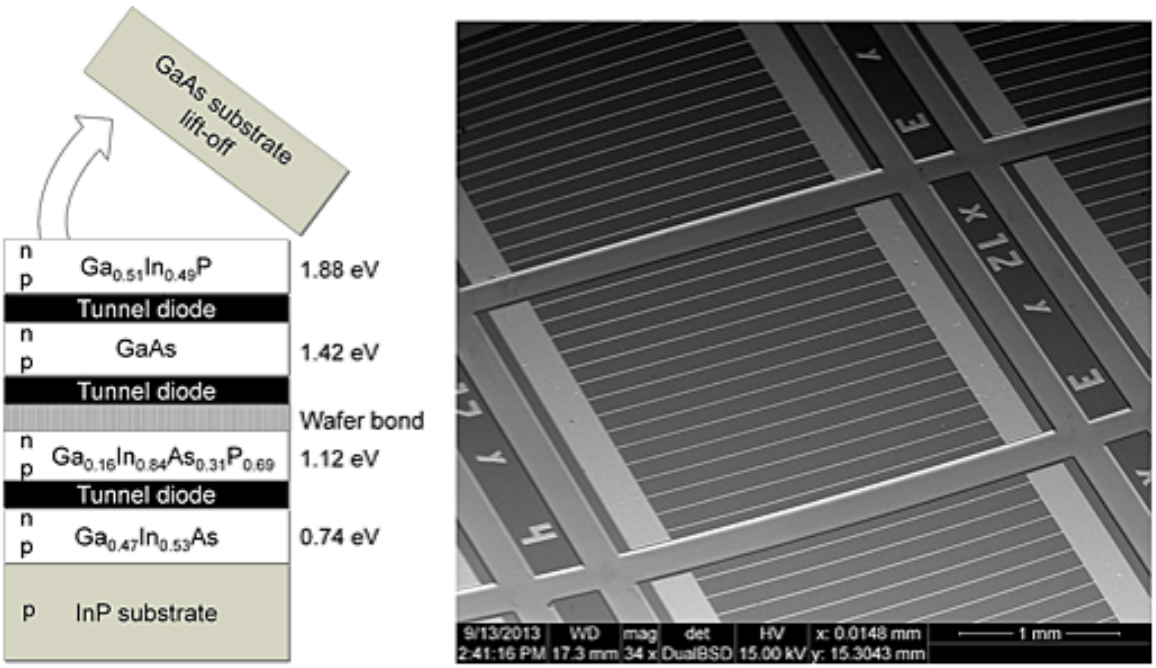

Figure 2.10: *(a) Layer structure of the fourjunction wafer bonded solar cell indicating the composition of the subcell materials with bandgap energies (b) Scanning electron microscopy image of the concentrator cell design with parallel grid fingers and two rectangular shaped busbars. Reproduced with permission from [47].*

2.7.4 Other approaches

Other design approaches for efficiency improvement which have garnered the attention of the CPV industry is the use of quantum wells or quantum dots to manipulate the effective band gap of an MJSC [48]. A quantum well essentially works as another photocurrent generator in parallel with the solar cell. Structures containing quantum dots have been reported as well [49]. In addition, mechanically stacked structures [50] with an efficiency of 30% under concentration and bi-facial epitaxial growth structures [51] with 42.3% efficiency under concentration have also been developed.

2.8 Multijunction solar cells under concentration

The benefits of using MJSCs under concentration is two-fold: (a) The reduction in system cost and (b) an increase in efficiency. While the economics of CPV have been discussed in Chapter 1, a detailed discussion on the second aspect is presented here.

An increase in solar cell efficiency under concentration is primarily attributed to an increase in the *open-circuit voltage*, V_{oc}, given by

$$V_{oc} = \frac{nkT}{q}\left[\ln\left(\frac{I_{sc}}{I_d}\right) + \ln\ X\right] \tag{2.13}$$

where I_{sc} is the short-circuit current, I_d is the dark saturation current and X is the concentration in suns. While the photocurrent is typically assumed to linearly increase with concentration, V_{oc} increases logarithmically. In the case of high-injection conditions with low series resistance, the photocurrent may increase super-linearly with concentration [52]. While further studies are required to quantify this effect, one study has reported linearity in GaAs solar cells for upto 1000 suns. For the analyses in this thesis, the short-circuit current is assumed to be linearly proportional to incident radiation.

2.9 Numerical modeling of multijunction cells

The availability of sophisticated numerical modeling tools for simulating semiconductor devices has significantly aided in process of modeling MJSCs. Numerical simulations provide a reasonable mathematical estimation of the various complex physical processes which

govern photovoltaic device behavior. Such simulations are a valuable tool for evaluation of devices at a design stage and allow for considerable flexibility to optimize newer designs. In addition to the thickness, doping densities and material properties for each layer, the knowledge of operating conditions including the temperature, incident spectrum and electrical bias are also required for setting up the simulations. Physical models governing generation, recombination, and conduction may also be defined within the software.

Once the device parameters are defined, a set of nonlinear equations for each layer in the structure need to be solved, with the boundary conditions for each interface. These equations include:

1. Poisson Equation: The Poisson equation relates the charge density to the electrostatic potential in a semiconductor and is defined as:

$$\nabla.\epsilon E = \rho \tag{2.14}$$

Here, ϵ is the permittivity, E is the electric field (related to the electrostatic potential as $E = \nabla.(\varphi)$), and ρ is the charge density.

Given that the charge density in a doped semiconductor is given by:

$$\rho = q\ (p - n + N_d - N_a) \tag{2.15}$$

where p is the hole concentration, n is the electron concentration, N_A and N_D are the acceptor and donor concentrations respectively, assuming 100% ionization.

The final equation can be written as:

$$\nabla(.\epsilon\nabla.\varphi) = -q\ (p - n + N_d - N_a) \tag{2.16}$$

2. Electron and hole continuity equations: These equations are based on the law of conservation of charge.

   For the electrons, it is given by:

$$\frac{\partial n}{\partial t} = \frac{1}{q}\nabla . J_n + G - \ U \tag{2.17}$$

   And for the holes, it is described by:

$$\frac{\partial p}{\partial t} = \frac{1}{q}\nabla . J_p + U - \ G \tag{2.18}$$

   where J_n and J_p are current-densities of holes and electrons, respectively, G refers to optical generation rate of the corresponding charge carrier, and U refers to the recombination rate.

   Under steady state conditions, the net change in flow of charge carriers, $\frac{\partial n}{\partial t} = \frac{\partial p}{\partial t} = 0$.

3. Drift-diffusion approximations: Current flow in a semiconductor is established by drifting of electrons due to electric field or by diffusion of carriers due to a concentration gradient. Combining the drift-diffusion contributions, the current-density for each carrier are obtained as:

   For electrons:

$$J_n = q(D_n \nabla n + n\mu_n E) \tag{2.19}$$

   For holes, it is given as:

$$J_p = q(D_p \nabla n + n\mu_p E) \tag{2.20}$$

D_p and D_n are the diffusion coefficients, and μ_n and μ_p are the mobilities of electrons and holes, respectively.

Solutions to the above equations can be calculated by using technology Computer-Aided Design (TCAD) tools. Commercially available drift-diffusion simulators such as Synopsys by Sentaurus [53], ATLAS by Silvaco [54], Crosslight by APSYS and COMSOL Multiphysics along with freely distributable software such as the PC1D developed at the University of New South Wales in Australia, ADEPT developed at Purdue University and AMPS developed at Pennsylvania State University have previously been used to simulate multijunction structures. Current-voltage curves and the quantum efficiencies are typically extracted from numerical simulations.

2.9.1 Simulation results

In this work, results obtained from the design of three and four junction solar cells are presented. Synopsys by Sentaurus has been used for numerical modeling. Using standardized material parameters, three MJSC designs have been developed within our research group. The first design is a typical lattice-matched three-junction solar cell (3JLM) with series-connected subcells composed of GaInP, InGaAs and Ge layers on a Ge substrate similar to [8]. The second design, a lattice-mismatched three-junction solar cell (3JIMM), has an inverted metamorphic configuration with a InGaP top layer, an InGaAs (1.4 eV) middle layer, and an InGaAs (1 eV) bottom layer [23]. The third design, four-junction, lattice-matched (4JLM) structure, is composed of GaInP, AlGaAs, and dilute nitride material on a doped Ge substrate, all series-interconnected using low-resistance tunnel junctions [16].

Each of the structures include an optimized anti-reflection coating and a metal contact. A small-symmetrical element of the cell has been simulated for each device. The material compositions, layer thicknesses, and doping concentrations for the 3JLM, 3JIMM and the 4JLM design is shown in Tables 2.2, 2.3 and 2.4 respectively. The front and back surface fields have been abbreviated as 'fsf' and 'bsf', respectively.

Table 2.2: *Layer structures for the three-junction, lattice-matched design.*

Layer name	**Material**	**Thickness** (μ**m**)	**Doping concentration** (**cm**$^{-3}$)
Subcell 1 fsf	n-$Al_{0.5}In_{0.5}P$	0.03	1.00E+19
Subcell 1 emitter	n-$Ga_{0.5}In_{0.5}P$	0.1	5.00E+18
Subcell 1 base	p-$Ga_{0.5}I_{0.5}P$	0.75	1.00E+17
Subcell 1 bsf	p-$(Al_{0.25}Ga_{0.75})_{0.5}In_{0.5}P$	0.12	1.00E+18
Tunnel junction	p-$Al_{0.15}Ga_{0.85}As$	0.02	6.00E+19
Tunnel junction	n-$Al_{0.15}Ga_{0.85}As$	0.02	3.00E+19
Subcell 2 fsf	n-$Ga_{0.5}In_{0.5}P$	0.03	5.00E+18
Subcell 2 emitter	n-$In_{0.01}Ga_{0.99}As$	0.08	1.00E+18
Subcell 2 base	p-$In_{0.01}Ga_{0.99}As$	3.5	1.00E+17
Subcell 2 bsf	p-$Ga_{0.5}In_{0.5}P$	0.1	1.00E+19
Tunnel junction	p-$Al_{0.3}Ga_{0.7}As$	0.05	4.00E+20
Tunnel junction	n-GaAs	0.05	2.00E+19
Subcell 3 buffer	n-$In_{0.01}Ga_{0.99}As$	0.2	2.00E+18
Subcell 3 fsf	n-$Ga_{0.5}In_{0.5}P$	0.02	5.00E+19
Subcell 3 emitter	n-Ge	0.1	1.00E+19
Subcell 3 base	p-Ge	170	2.00E+17

Table 2.3: *Layer structures for the three-junction, lattice-mismatched, inverted metamorphic design.*

Layer name	**Material**	**Thickness** (μ**m**)	**Doping concentration** (**cm**$^{-3}$)
Subcell 1 fsf	n-$Al_{0.5}In_{0.5}P$	0.05	1.00E+19
Subcell 1 emitter	n-$Ga_{0.5}In_{0.5}P$	0.04	2.00E+18
Subcell 1 intrinsic	p-$Ga_{0.5}In_{0.5}P$	0.3	1.00E+16
Subcell 1 base	p-$Ga_{0.5}In_{0.5}P$	0.41	1.00E+17
Subcell 1 bsf	p-$(Al_{0.25}Ga_{0.75})_{0.5}In_{0.5}P$	0.1	1.00E+18
Tunnel junction	p-$Al_{0.3}Ga_{0.7}As$	0.03	2.00E+19
Tunnel junction	n-$Al_{0.3}Ga_{0.7}As$	0.03	2.00E+19
Subcell 2 fsf	n-$Ga_{0.5}In_{0.5}P$	0.03	5.00E+18
Subcell 2 emitter	n-$In_{0.01}Ga_{0.99}As$	0.07	3.00E+18
Subcell 2 intrinsic	p-$In_{0.01}Ga_{0.99}As$	0.5	5.00E+15
Subcell 2 base	p-$In_{0.01}Ga_{0.99}As$	1.8	1.00E+17
Subcell 2 bsf	p-$Ga_{0.5}In_{0.5}P$	0.1	1.00E+19
Tunnel junction	p-$Al_{0.3}Ga_{0.7}As$	0.03	2.00E+19
Tunnel junction	n-GaAs	0.03	2.00E+19
Subcell 3 buffer	n-$Ga_{0.99}In_{0.01}As$	0.2	1.00E+18
Subcell 3 buffer	n-$Ga_{0.51}In_{0.49}P$	0.25	5.00E+15
Subcell 3 buffer	n-$Ga_{0.47}In_{0.53}P$	0.25	5.00E+15
Subcell 3 buffer	n-$Ga_{0.43}In_{0.57}P$	0.25	5.00E+15
Subcell 3 buffer	n-$Ga_{0.39}In_{0.61}P$	0.25	5.00E+15
Subcell 3 buffer	n-$Ga_{0.35}In_{0.65}P$	0.25	5.00E+15
Subcell 3 buffer	n-$Ga_{0.31}In_{0.69}P$	0.25	5.00E+15
Subcell 3 buffer	n-$Ga_{0.27}In_{0.73}P$	0.25	5.00E+15
Subcell 3 buffer	n-$Ga_{0.22}In_{0.78}P$	0.25	5.00E+15
Subcell 3 buffer	n-$Ga_{0.25}In_{0.75}P$	0.25	5.00E+15
Subcell 3 emitter	n-$Ga_{0.7}In_{0.3}As$	0.1	1.00E+18
Subcell 3 base	p-InGaAs	4	1.00E+16

Figure 2.11 shows the EQE as extracted using Sentaurus. Solar cell EQEs are less than 1 due to optical transmission and reflection losses. The third and fourth subcells in the four-junction structure have reduced EQEs due to photon sharing between them. It can

Table 2.4: *Layer structures for the four junction, lattice-matched design.*

Layer name	**Material**	**Thickness** (μ**m**)	**Doping concentration** (**cm**$^{-3}$)
Subcell 1 fsf	n-$Al_{0.5}In_{0.5}P$	0.025	6.00E+18
Subcell 1 emitter	n-$Ga_{0.5}In_{0.5}P$	0.1	5.00E+18
Subcell 1 base	p-$Ga_{0.5}In_{0.5}P$	0.65	8.00E+16
Subcell 1 bsf	p-$Al_{0.5}In_{0.5}P$	0.05	3.00E+19
Tunnel junction	p-$Al_{0.3}Ga_{0.7}As$	0.03	2.00E+20
Tunnel junction	n-$Ga_{0.5}In_{0.5}P$	0.03	6.00E+19
Subcell 2 fsf	n-$Al_{0.8}Ga_{0.2}As$	0.03	1.00E+19
Subcell 2 emitter	n-$Al_{0.05}Ga_{0.95}As$	0.1	3.00E+18
Subcell 2 base	p-$Al_{0.05}Ga_{0.95}As$	2	1.00E+17
Subcell 2 bsf	p-$Al_{0.04}Ga_{0.96}As$	0.08	1.00E+19
Tunnel junction	p-$Al_{0.3}Ga_{0.7}As$	0.03	1.20E+20
Tunnel junction	n-$Al_{0.05}Ga_{0.95}As$	0.03	6.00E+19
Subcell 3 fsf	n-GaAs	0.05	1.00E+19
Subcell 3 intrinsic	n-$In_{0.11}Ga_{0.89}AsN$*	0.65	2.00E+15
Subcell 3 bsf	p-GaAs	0.05	1.00E+19
Tunnel junction	p-$Al_{0.3}Ga_{0.7}As$	0.03	1.20E+20
Tunnel junction	n-GaAs	0.03	6.00E+19
Subcell 4 fsf	n-GaAs	0.05	7.00E+17
Subcell 4 emitter	n-Ge	0.1	5.00E+18
Subcell 4 base	p-Ge	170	1.00E+18

be seen that optical interference effects from the multiple layers above the lower subcells cause oscillations in the EQE, specifically in the bottom two subcells. Since 3JLM cells have been commercially available for some years, these cells have been used as a reference design for comparative evaluation of the more novel 3JIMM and 4JLM designs [24].

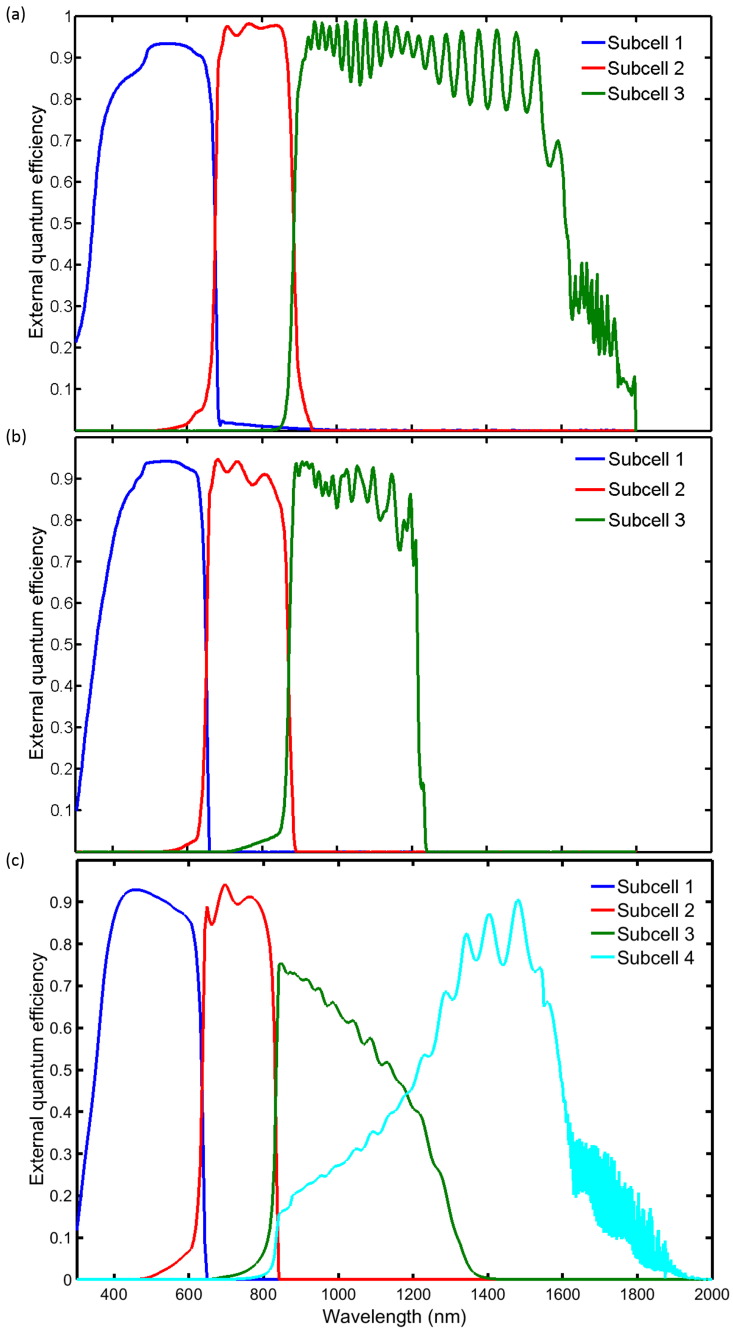

Figure 2.11: *External quantum efficiencies for the (a) 3JLM, (b) the 3JIMM, and (c) the 4JLM as simulated using the structures described in the tables above.*

These designs have been used throughout this thesis for evaluation of various param-

eters. Subcell I-V curves are generated by Sentaurus Device using the virtual contact method, under uniform illumination by the normalized spectrum of the smallest two-dimensional symmetry element of the MJSC. Figure 2.12 shows the current-density vs. voltage curves for the three designs. Under 1 sun, the top two subcells are current matched at 13.6 mA/cm^2 while the bottom subcell overproduces at 22.5 mA/cm^2 in the 3JLM design. For the 3JIMM design, all subcells are almost fully current matched at 14($\pm$0.3) mA/cm^2 while for the 4JLM the top and bottom subcells are almost current matched at 12.9 mA/cm^2. The second subcell (AlGaAs) slightly underproduces 12.7 mA/cm^2 while the dilute nitride subcell overproduces at 13.3 mA/cm^2. Current overproduction in the dilute nitride subcell is required in order to compensate for its poor fill-factor. Cell efficiencies under 1000 suns are 37%, 42.5% and 43.4% for the 3JLM, the 3JIMM and the 4JLM design, respectively.

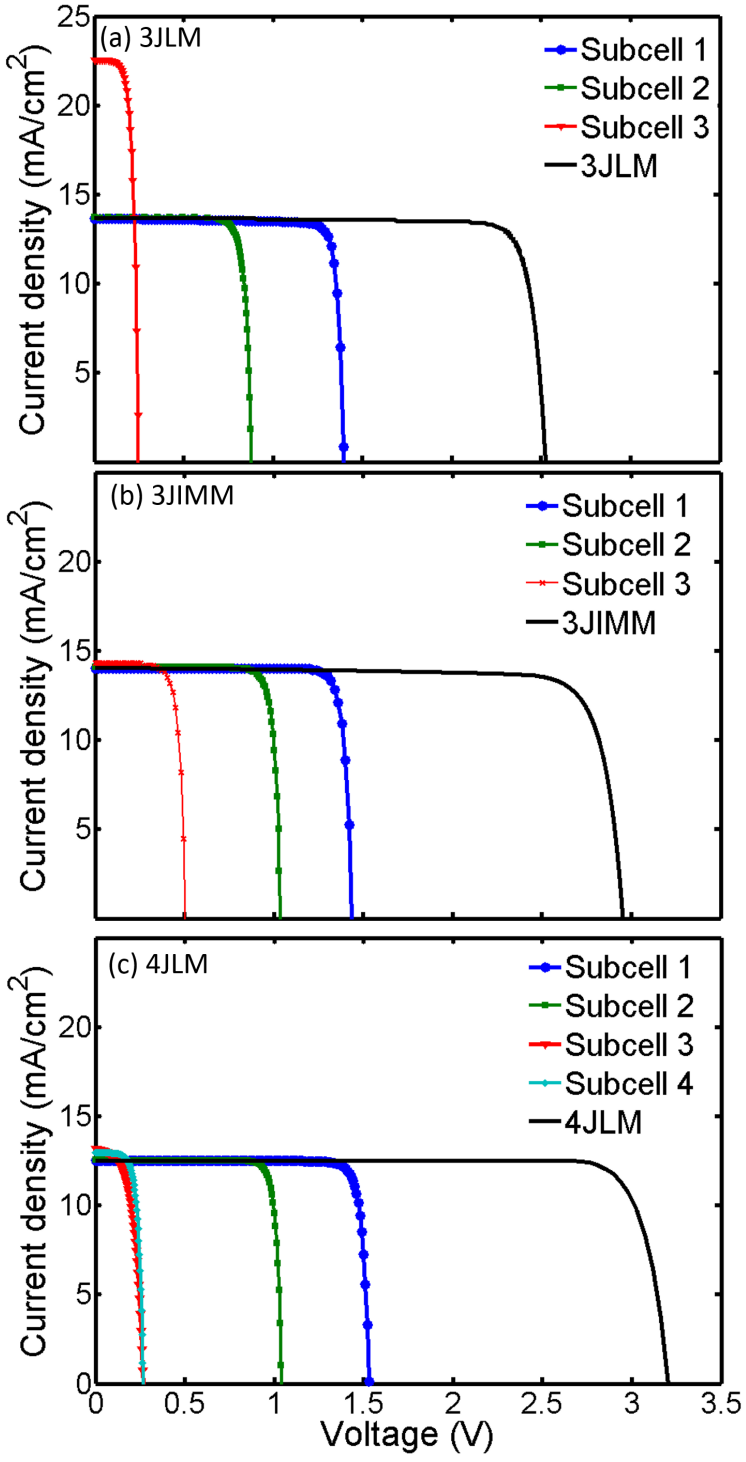

Figure 2.12: *Current-density as a function of voltage for (a) the 3JLM, (b) the 3JIMM, and (c) the 4JLM design at 1 sun.*

2.9.2 Challenges of numerical modeling

Numerical modeling, although useful for semiconductor device simulation, is limited in its ability to simulate distributed effects. Computational time puts a significant restraint on the simulation of the device. Typically, small elements with a width half that of the finger spacing are modeled, ensuring that lateral current flows are accurately determined while minimizing computational time.

2.10 Summary

Multijunction solar cells are specially suited for CPV applications due to their record high efficiencies. An efficiency increase under concentration due logarithmic increase in the open-circuit voltage aids in the application of MJSCs for high concentration systems. While three-junction, lattice-matched approaches have established a place in the commercial CPV market, the advancement in technology is leading to improved designs with higher number of junctions. In order to understand the underlying processes governing the MJSC, drift-diffusion simulations have been successfully used. Three different designs with specific layer structures have been modeled using TCAD tools and corresponding EQEs and subcell I-V curves have been obtained. Although, these numerical modeling tools provide valuable knowledge about MJSC performance, such tools are limited in their ability to simulate nonuniform, distributed effects. High computational times limit their usage to the simulation of small area, symmetrical MJSC elements. Therefore, a means to model MJSCs, for performance analysis under nonuniform illumination, is required.

Chapter 3

Distributed circuit models

Everything should be made as simple as possible,

but not simpler.

Albert Einstein

Understanding the performance characteristics of concentrator solar cells is critical for the design of CPV systems. Concentrator solar cells may operate over a range of illumination conditions, typically from few hundred to more than 1000 suns, and under a variety of illumination profiles, depending on the CPV optics. Defining the performance of MJSCs based on these operational parameters is hence necessitated. Although experimental procedures can be adopted for determining device efficiencies under variable operating conditions, such experimental procedures can be expensive and complex to implement. Modeling and simulation, therefore, play an important role in understanding device behaviour specially under nonuniform illuination conditions. Numerical modeling allows for

detailed device simulations and is an important tool for understanding the physical device processes. The drawback of the approach, however, is that it is complex to implement and requires high computational resources, making it unsuitable for implementation at the system level. Therefore, usage of numerical models is limited to the simulation of small symmetrical elements of the solar cell under normal, uniform illumination conditions.

In order to conduct more realistic simulations of a CPV system, analytical models are often employed. Assuming accuracy penalties, a one- diode or two-diode equivalent circuit model is often used for simulating an MJSC. Recombination and photogeneration in individual layers is ignored and tunnel junction effects are also neglected in such models. However, oversimplification of solar cell layers and neglect of distributed effects make such analytical models limited in their application.

If the fundamental one-diode or two-diode model is considered to be valid at a microscale where distributed effects are negligible, the solar cell can be divided into small functional units, each unit represented by a one or a two-diode equivalent circuit. These functional units can be interconnected to form the entire area of the solar cell. Such models have been termed as *distributed* models. Since these models may include hundreds and thousands of interconnected electrical components, simulations have to be performed using circuit simulators such as Simulation Program with Integrated Circuit Emphasis tools. SPICE tools are widely available and have been used in a variety of applications to verify the integrity of circuit designs and to predict circuit behavior. By modeling solar cells in terms of their equivalent circuits, the need to solve complex transcendental equations for quantitative analysis is eliminated.

In this chapter, a brief review of the distributed circuit models is presented. An improved, parametrized distributed circuit model for three and four junction solar cells is proposed and the applications of the proposed model for performance analysis at varying concentrations and illumination profiles are detailed. A comparative analysis is performed thereafter and effects of nonuniform illumination are quantitatively determined. The effect of luminescent coupling on performance efficiencies is also determined.

3.1 Background of distributed circuit models

The inadequacy of lumped analytical models to simulate distributed effects has led to the development of distributed circuit models. In this section, a review of distributed circuit models, in the order of increasing degree of complexity, is presented. The simplest of the circuit models is the one-dimensional model (1-D). 1-D models can be effectively used to simulate cell characteristics for a variety of conditions. 1-D models assume spatial homogeneity for every cell layer and provide good approximations under normal conditions, assuming uniform illumination for a well-designed solar cell. In some cases, 1-D models are modified to incorporate distributed effects by the addition of extra diodes and resistors. A 1-D model to simulate the distributed series resistance effects was first presented in the early 1980s [55]. Another 1-D model was presented by Zekry [56] to model nonhomogenous current distribution. This model uses the small-signal parameters as shown in Figure 3.1 and requires experimentally obtained dark IV characteristics and small-signal impedance measurements. These models however, mostly aimed to simulate silicon solar cells, are limited in their capability to simulate spatially varying effects.

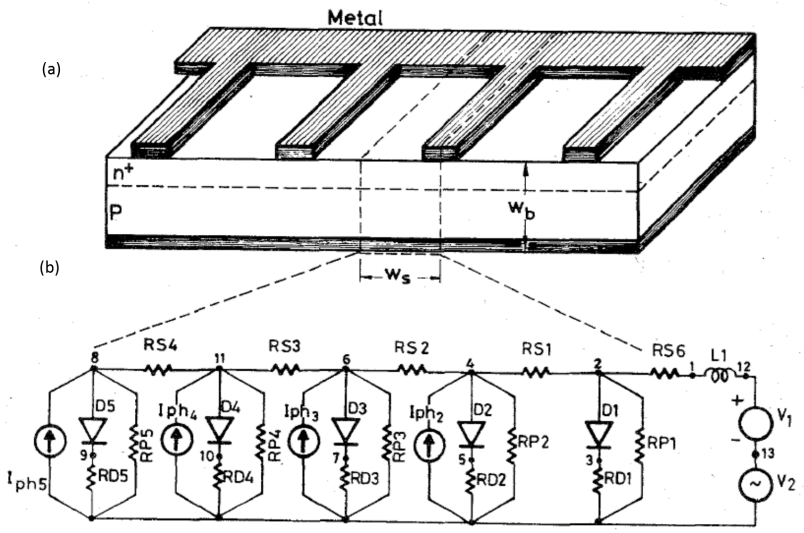

Figure 3.1: *A one-dimensional distributed resistance model for a solar cell using small signal parameters ©1996 IEEE.*

The two-dimensional (2-D) modeling approach was first adopted by Araki [57] and Nishioka [58]. Figure 3.2 shows the 2-D model developed by Nishioka for a three-junction solar cell. The model uses a one-diode equivalent circuit for simulating each junction. Equivalent circuits for shaded areas underneath the contacts are not included in the model. The model, although useful for simulating spatial effects, neglects the dark areas underneath the contacts. This implies that the lateral resistances of the shaded areas is ignored. Hence, it may not provide accurate results at higher concentration where lateral resistance effects are more prominent.

The succeeding model, in terms of complexity, is the three-dimensional (3-D) model. A 3-D scheme was developed by Galiana *et al.* in 2006 [59]. This model was initially validated for a single-junction GaAs solar cell and was later extended to three-junction solar cells. It was also improved to add tunnel junction based effects [60]. Figure 3.3 shows

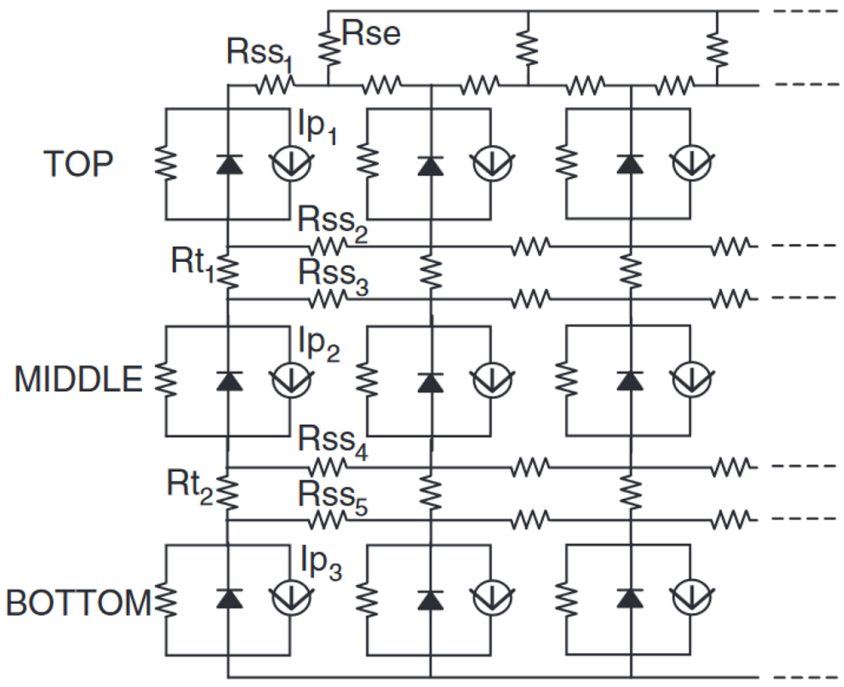

Figure 3.2: *A two-dimensional, distributed resistance model for a triple-junction solar cell. Reproduced with permission from [58].*

the 3-D model of a single junction solar cell, with the details of the elementary units.

Although, such a model is necessary for simulating non-linear contact grids and unsymmetrical illumination profiles, the downside of sophisticated 3-D models is the amount of time and resources required for the simulation. The CPU calculation time, according to [59], to calculate each I-V point is βN^{α} where the author suggested a β value of 10^{-9} s and α of 2.8. N refers to the number of nodes. For a dual junction device, a total of 18000 nodes was suggested [61]. For a circuit with 18000 nodes the CPU calculation time will be about 14 minutes for every point on the I-V curve. If the voltage sweep is run between 0 to 4V with 0.01 V interval, 400 such points will be required for simulating one I-V curve. This would then imply a total calculation time of about 93 hours to simulate a two-junction

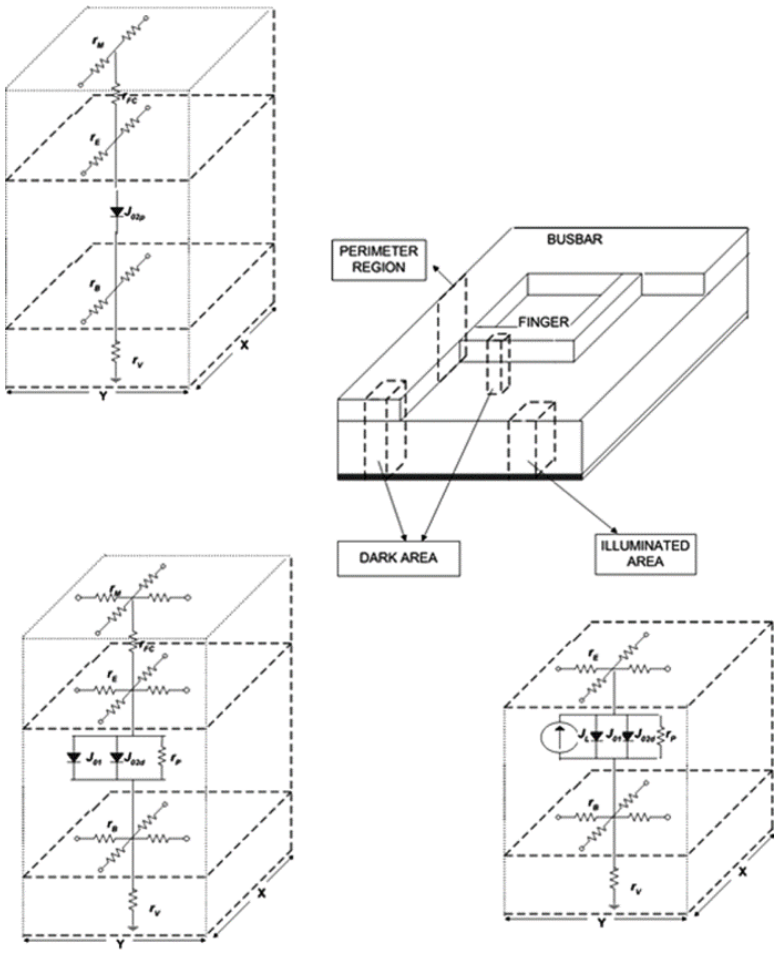

Figure 3.3: *Three-dimensional distributed model for a single-junction solar cell with the definition of the different types of functional units ©2005 IEEE.*

solar cell. It can be also assumed that such a model will require atleast double the amount of time to simulate a four-junction solar cell.

3.2 Proposed distributed circuit model

In light of the high computational time required for a 3-D model as described in the section above, an improved 2-D distributed circuit model is proposed in this thesis. The

proposed model is composed of two-diode equivalent circuits for each subcell in the MJSC. This model is an improvement over the 2-D model illustrated in [58] due to the fact that the equivalent circuits for shaded or dark areas underneath the metal contact have been included. The inclusion of equivalent circuits for non-illuminated areas may not significantly affect cell efficiency under uniform illumination but may have more of an impact under non-uniform illumination specifically at high concentrations. Figure 3.4 shows the model of one functional block and the electrical circuit in SPICE used to simulate the distributed resistance model. LTSPICE by Linear Technology Corporation [62] was used as the SPICE simulator. A functional block in this model is considered to be a combination of the subcells connected via tunnel junctions. The proposed model has been developed both for a three-junction as well as a four-junction solar cell.

The proposed 2-D model incorporates:

1. Two-diode equivalent circuit models for each subcell (SC) of the MJSC. In Figure3.4, this is represented electrically as two diodes in parallel with the current source (representing the light-generated current) and a shunt resistance.

2. Lateral resistance connecting cells across the rows in the model and is obtained from the sheet resistance values for each layer. Given a specific finger spacing (S_f) and finger length (L_f), the total lateral resistance (R_L) for each of the layers has been calculated on the basis of the following equation derived from [63]:

$$R_L = R_{Illuminated} + R_{Dark} \tag{3.1}$$

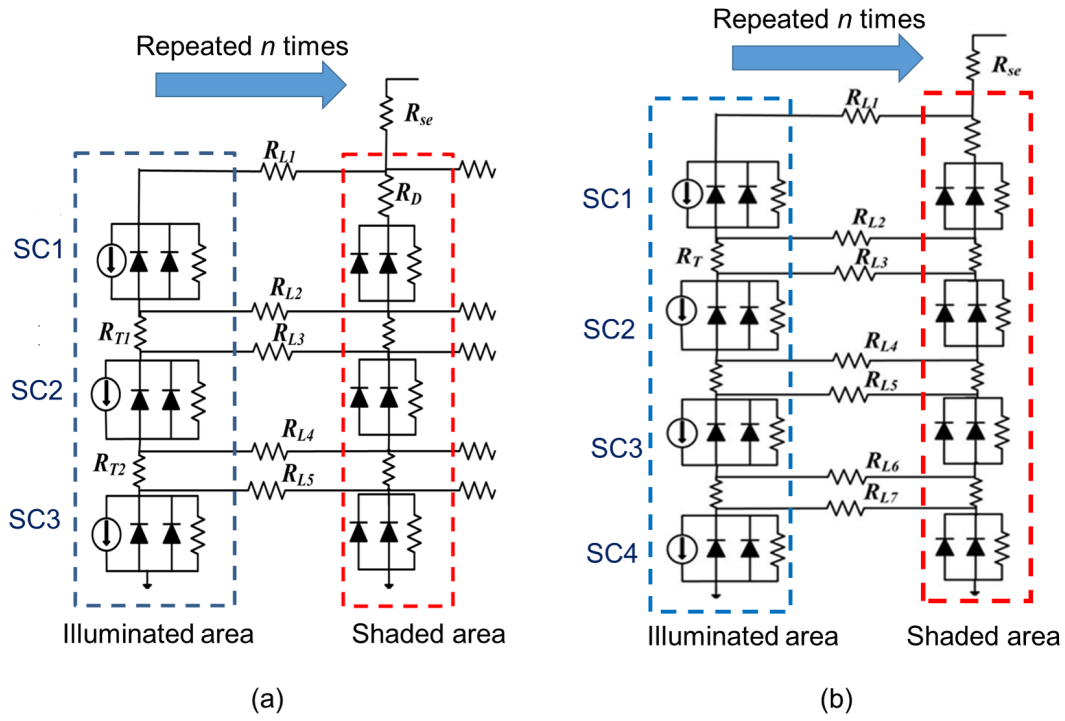

Figure 3.4: *2-D distributed resistance model developed in SPICE showing the two-diode equivalent circuits for each of the subcells (SCs) where subcells are connected in series using low-resistance tunnel junctions. An illuminated and a shaded unit form a complete functional block that is repeated n times. (a) shows the model for a three-junction solar cell and (b) shows the extension of the model to a four-junction cell.*

For the illuminated area,

$$R_{Illuminated} = R_{Sheet} \times \frac{S_f}{2} \times L_f \tag{3.2}$$

For the area under the electrodes, the lateral resistance is determined as

$$R_{Dark} = R_{Sheet} \times \frac{W_f}{2} \times L_f \tag{3.3}$$

where W_f is the finger width.

The number of function blocks for a fixed cell dimension determines the spacing between fingers [63], [64].

$$\text{Number of functional blocks} = \frac{\text{Unit cell area}}{(S_f + W_f).L_f} \tag{3.4}$$

3. Low resistance tunnel junctions: Since the peak current density is typically designed to be several times higher than the peak current density of the MJSC [65], the tunnel junctions in this model are assumed to be resistive (R_T). The resistance is fixed at < 1 mΩ.

4. The electrode resistance is denoted by R_{se} and can be varied on the basis of metal resistances. Since electrode resistance forms the largest component of the series resistance, effects originating due to electrodes resistance will dominate and may mask the effects of lateral resistances. In order to assess the impact of lateral resistance variations (which originate from MJSC layer structures), electrode resistances are assumed to be negligible in our simulations.

Finger widths are fixed at 5 μm for all simulations. The model accounts for shading losses due to the fingers and Ohmic losses due to series resistances. Bus bars are assumed to be outside the active cell area and are not included in the model.

3.2.1 Justification for a 2-D distributed circuit model

(a) Computational resources and computational time

As calculated earlier, computational times are significantly long with 3-D models even for small sized, three-junction devices. The times calculated in the previous section rise significantly with the number of nodes and have been primarily calculated under uniform conditions for two-junction cells. Such times will worsen if the model is expanded to include more junctions. In addition, effects of nonuniform illumination, varying temperatures and radiative coupling would add further complexity to the model, draining computational resources and augmenting simulation time. In contrast, the 2-D model proposed in this thesis is significantly faster and provides valuable quantitative results for realistic irradiance distributions. Hence, there is a trade-off between computational time and accuracy. Figure 3.5 shows the computational time as a function of number of functional units (one functional unit consisting of one illuminated and one shaded unit) required to simulate a three and a four-junction solar cell using an Intel core i5 processor. The data shown corresponds to the total CPU time for simulating a 1 cm^2 solar cell at 13 different concentrations. I-V curves are generated over a range of 0 to 4 V with a 0.01 V step-size for each concentration. It can be seen that the computational time increases geometrically with the number of functional units. Comparative analysis shows an increase of CPU calculation time by 1.5× with a four-junction device as compared to a three-junction device. This indicates that the 2-D model is significantly more efficient in terms of computational time than the 3-D model even for the three-junction cell.

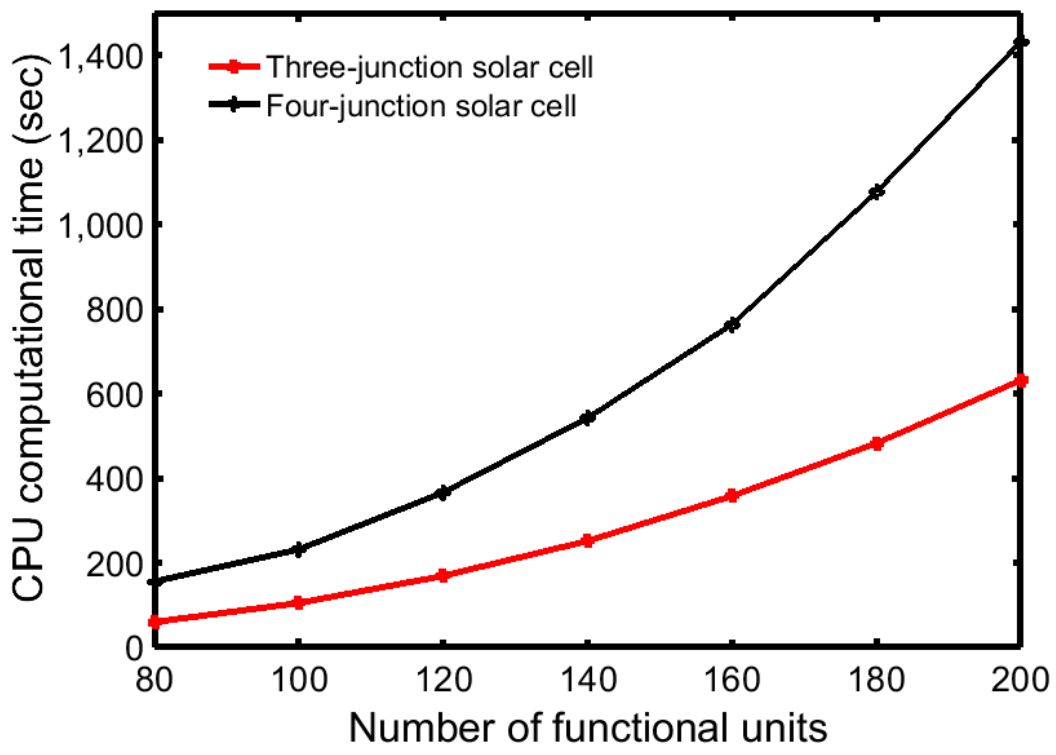

Figure 3.5: *CPU computational time as a function of the number of functional units, as obtained using LTSPICE for a three-junction and a four junction solar cell.*

(b) Modeling the grid

Commercially available 10 mm side and 5 mm side solar cells and their isotypes typically use a comb-like linear metal finger pattern as the top contact [66]. Figure 3.6 shows a photograph of a Spectrolab triple junction cell with a linear grid. Using a linear grid implies that further modeling complexities can be avoided and a 2-D model will suffice for simulation.

In comparison to a 1-D model, which is inadequate for simulation of distributed effects, a 2-D model provides a means to simulate realistic non-homogenous scenarios, without exhausting computational resources and without having exceedingly high computational

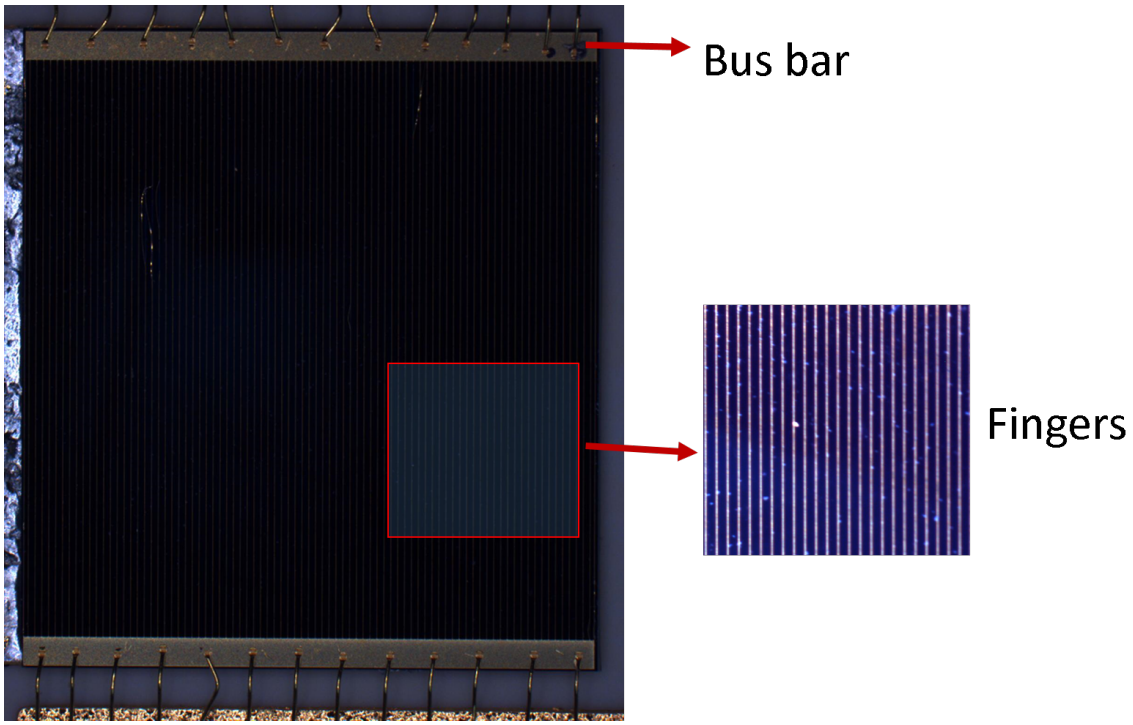

Figure 3.6: *Top view of a Spectrolab triple junction solar cell with a linear grid. Bus bars are located at the two ends while metalized fingers are spaced linearly throughout the cell. A zoomed in view of the fingers is also presented.*

times. Hence, a 2-D approach is adopted for simulations throughout this thesis.

3.2.2 Parameter extraction

A important step in setting up the model is the parameter extraction step. Solar cell parameters have to be obtained using I-V curves. Both subcell I-V curves and complete MJSC I-V curves are required in order to extract parameter values using this method. In order to simulate a single subcell within a multijunction solar cell, either a one-diode or a two-diode equivalent circuit can be used. A two-diode equivalent circuit model has been used in this thesis, as it is known to yield more accurate results under concentration than a

one-diode model [67]. Parameter extraction has been done using MATLAB's *curve-fitting* toolbox [68]. Solar cell parameters have been determined for each subcell by curve-fitting the subcell I-V curves to

$$I = I_L - I_{D1} - I_{D2} - \frac{(V + IR_S)}{R_{sh}}, \tag{3.5}$$

where the individual diode equations are

$$I_{D_1} = I_{01}\left[exp\left(\frac{q(V + IR_S)}{kT}\right) - 1)\right], \tag{3.6}$$

$$I_{D_2} = I_{02}\left[exp\left(\frac{q(V + IR_S)}{2kT}\right) - 1)\right]. \tag{3.7}$$

I_L is the light-generated current (which it is directly proportional to the solar irradiation), I_{01} and I_{02} are reverse saturation currents, q is the electronic charge, k is the Boltzmann constant, R_S is the series resistance, R_{sh} is the shunt resistance, V is the output voltage and I is the output current of the solar cell.

The values of I, V are obtained from the I-V curves and the values for R_S are known from the sheet resistances of the TJSC structure. Sheet resistance values have been calculated from the mobility and thickness values of each layer. The remaining unknowns, I_L, I_{01}, I_{02} and R_{sh}, have been determined by curve-fitting using the least-squares method [64]. The

Subcell I-V curves are required in order to perform the parameter extraction step. These curves can be obtained by numerical modeling using drift-diffusion simulators as

demonstrated in Chapter 2 or by using experimental values. In order to extract the equivalent circuit parameters for multijunction cells, the isotype reference cells are used. Isotype cells from Spectrolab have been used to obtain subcell I-V curves for a triple junction lattice matched cell. Figure 3.7 shows the I-V curves obtained using an in-house Newport Oriel solar simulator. The simulator is capable of concentrations up to 150 suns. The extracted parameters have very similar values both with numerically modeled and experimentally obtained data for three junction, lattice-matched designs. However, parameters for the three-junction inverted metamorphic and the four-junction lattice-matched designs are solely obtained from TCAD simulation results presented in Chapter 2.

This thesis focuses primarily on the following three MJSC designs. In the rest of this chapter, the I-V curves (detailed in Chapter 2) obtained by numerical modeling of the three designs have been used for parameter extraction. The designs are enumerated again here:

1. Three-junction, lattice-matched solar cell (3JLM)

2. Three-junction, inverted metamorphic, lattice-mismatched solar cell (3JIMM)

3. Four-junction, lattice-matched solar cell (4JLM)

Table 3.1 shows the extracted parameter values for the three designs as obtained using MATLAB.

The diode current values are determined by the open-circuit voltages for each subcell at 1 sun. In the case of the 3JLM and 3JIMM, the middle cell open circuit voltages are 0.88 and 1.04 V respectively, hence the difference in the recombination current values. The sheet

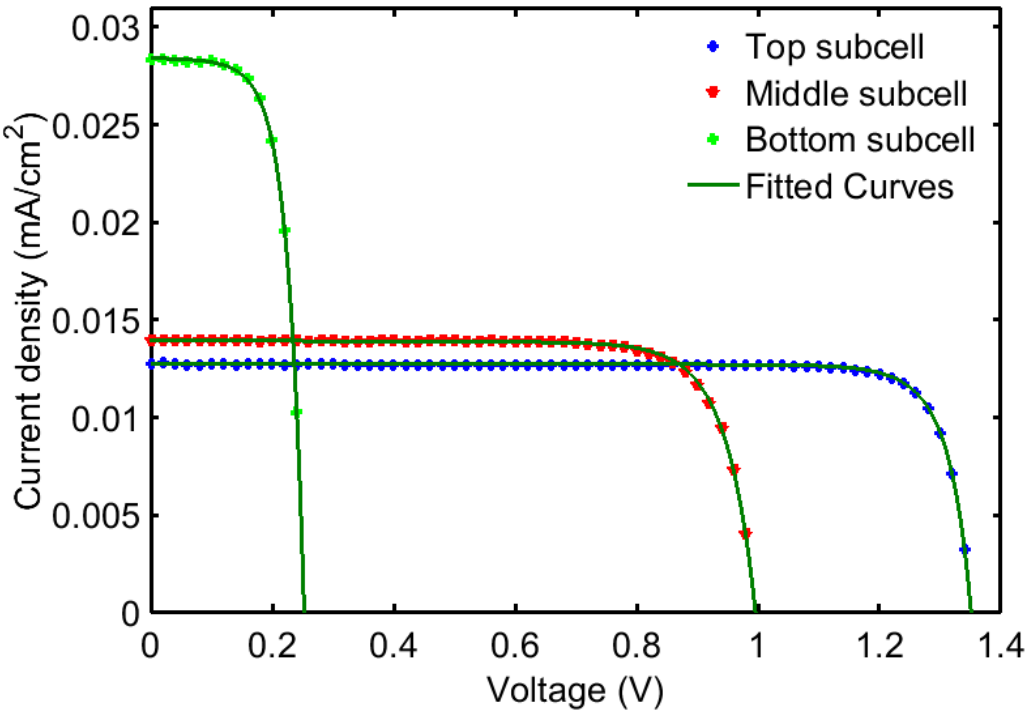

Figure 3.7: *Data fitted to experimental values obtained from subcell isotypes. Both numerical modeling and experimental approaches can be adopted for parameter extraction and yield similar design parameters for the 3JLM design.*

Table 3.1: *The SPICE parameters for the three MJSC designs extracted from subcell IV curves for 5% shading on a 1cm^2 solar cell at 300K. The parameters correspond to the MJSCs developed using numerical modeling as described in Chapter 2.*

3JLM	$\mathbf{I}_{01}$ **(A)**	$\mathbf{I}_{02}$ **(A)**	$\mathbf{R}_{sh}$ **(kΩ)**	$\mathbf{R}_L$ **(Ω)**
Top subcell	5.5×10^{-26}	4.3×10^{-15}	4	R_{L1}= 1.1 , R_{L2} = 27.0
Middle subcell	2.0×10^{-17}	1.5×10^{-10}	4	R_{L3} = 1.1 , R_{L4} = 2.7
Bottom subcell	1.4×10^{-6}	2.2×10^{-5}	4.6	R_{L5} = 0.2
3JIMM				
Top subcell	3.0×10^{-27}	2.5×10^{-14}	4	R_{L1}= 2.2 , R_{L2} = 42.1
Middle subcell	4.3×10^{-20}	8.7×10^{-12}	3	R_{L13} = 0.6 , R_{L4} = 13.2
Bottom subcell	3.7×10^{-11}	2.1×10^{-7}	2	R_{L5} = 1.3
4JLM				
Top subcell	7.1×10^{-29}	4.0×10^{-16}	6	R_{L1}= 1.3 , R_{L2} = 7.6
Middle subcell 1	3.0×10^{-20}	1.0×10^{-12}	3.4	R_{L3} = 0.6 , R_{L4} = 4.2
Middle subcell 2	2.2×10^{-8}	6.0×10^{-5}	7.3	R_{L5} = 0.4 , R_{L6} = 6.3
Bottom subcell	3.5×10^{-7}	2.9×10^{-12}	1	R_{L7}= 0.4

resistance of the 3JIMM top subcell is adjusted to fit to the I V curves of the Sentaurus model at various concentrations. In the case of the 3JLM and 3JIMM designs Also, tunnel junctions have been designed specifically for individual structures using AlGaAs, InGaP and GaAs materials and have been optimized such that they are optically transparent to the layer beneath.

3.3 Results

Using the parameters extracted for the three designs, simulations are performed for different scenarios with the three designs. Performance is evaluated by calculating efficiencies at the maximum power point, assuming 1 sun = 1000 W/m^2

3.3.1 Impact of high concentration under uniform illumination

The impact of concentration has been evaluated using the improved 2-D model by assuming a linear relationship between the short-circuit current-density and geometric concentration as below.

$$J_{sc_x} = X.J_{sc}, \tag{3.8}$$

It is also assumed that the recombination current-densities (J_{01} and J_{02}) and the ideality factor do not vary with concentration. Simulation results for the three designs assuming a cell area of 1 cm^2 and 5% shading due to gridlines are presented in Figure 3.8. Efficiencies peak at thousands of suns for all the three designs. Departure from the optimal concentration leads to an efficiency reduction in all cases. An absolute efficiency decrease of 0.6%, 1.7% and 0.2% is seen if the concentration is increased from 1250 to 2500 suns for the 3JLM, 3JIMM and 4JLM designs respectively. The rate of efficiency decrease with higher than optimal concentrations is much greater for the 3JIMM as compared to the other two designs. While the 3JLM and 4JLM designs perform better at concentrations higher than optimal (>1000 suns) as compared to the 3JIMM design, the efficiency decrease of the

3JIMM design is lesser than the other two designs at concentrations lower than optimal (<500 suns).

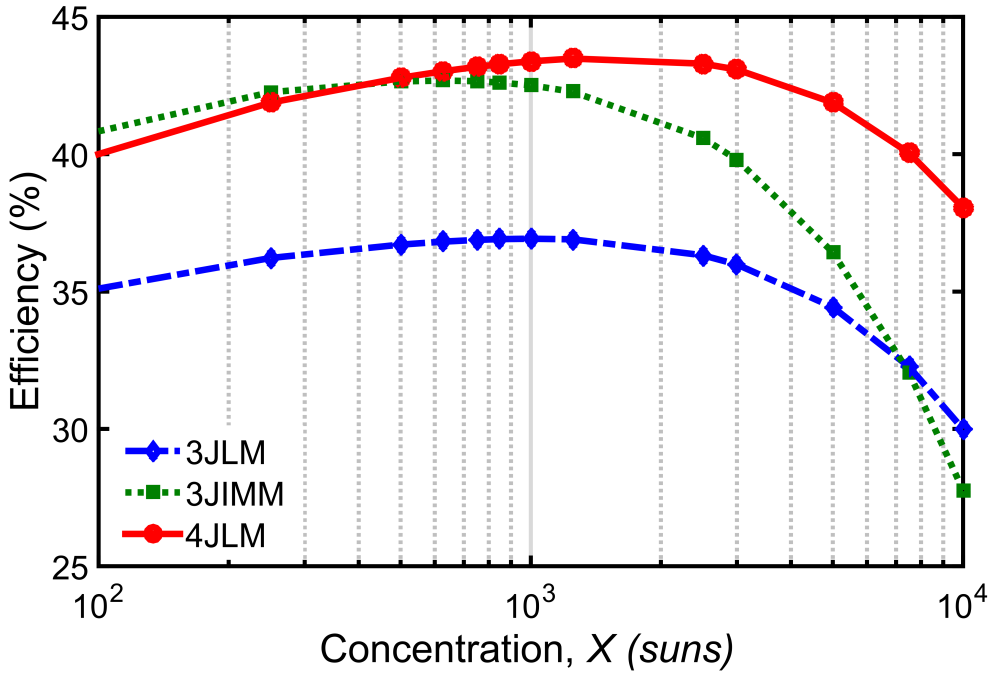

Figure 3.8: *Absolute efficiency obtained as a function of concentration from 100 to 10000 suns for the (a) the 3JLM (b) the 3JIMM and (c) the 4JLM design. All the simulations are performed under uniform illumination conditions with 5% shading.*

3.3.2 Effect of spatially nonuniform illumination

Concentration optics often create non-uniform profiles on solar cells which are not effectively flattened by secondary optic solutions [69]. Concentrator PV system optics often generate profiles that peak sharply at the center of the cell and follow a Gaussian distribution [70]. Peak-to-average irradiance ratios (PAR) typically range between 2 and 10 [71], but greater PARs are not unknown [72]. The non-uniformity in irradiance leads to a non-

uniformity in current production that can decrease cell efficiency [73], [74]. Decrease in cell performance becomes increasingly evident at higher concentrations, where increasing current densities drive higher series resistance (I^2R) losses. The impact of these I^2R losses is a reduction in fill factor and therefore a reduction in conversion efficiency [25].

In order to model nonuniform illumination conditions, Gaussian profiles with varying peak-to-average irradiance ratios (PARs) are chosen. A greater PAR value implies a higher degree of spatial nonuniformity. Spectral nonuniformities are neglected in these simulations and all the subcells in the distributed model receive the same irradiance which varies spatially. Figure 3.9 shows a sample of Gaussian irradiance profiles used for the simulations.

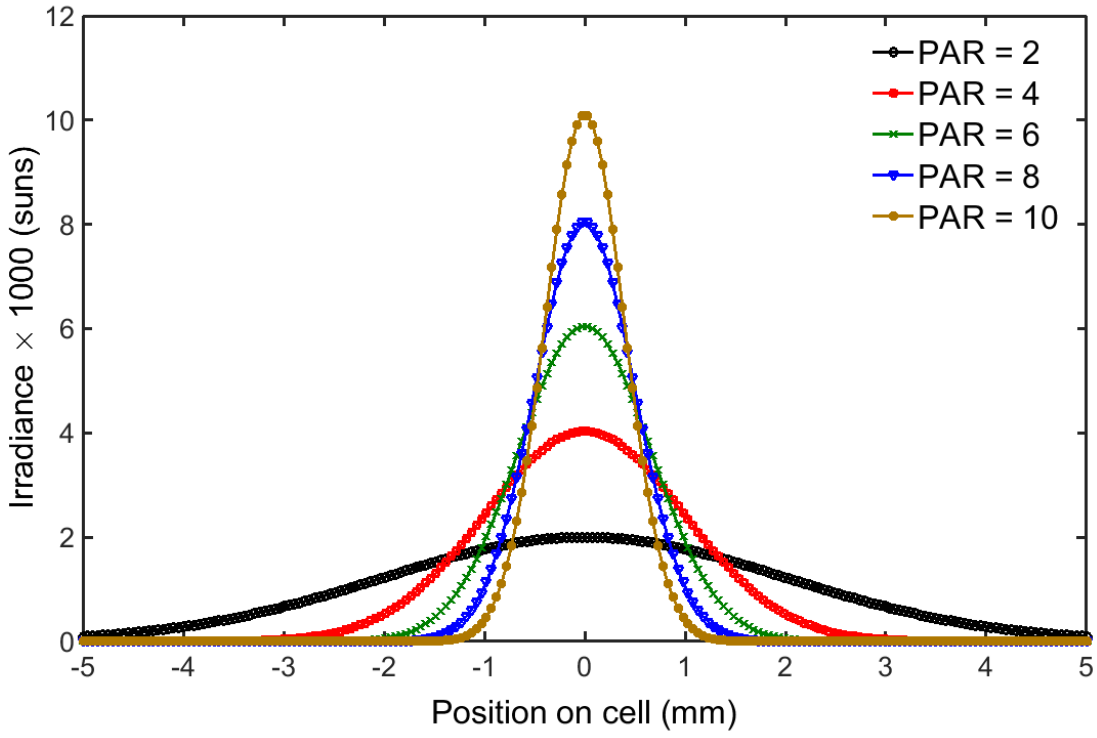

Figure 3.9: *Gaussian illumination profiles with varying peak-to-average irradiance ratios to represent different types of CPV optics.*

Figure 3.10 shows the effect of nonuniform illumination on all the three designs. Contour plots are used to show the variation in efficiency with changes in the degree of nonuniformity (in terms of PARs) and with changes in concentration.

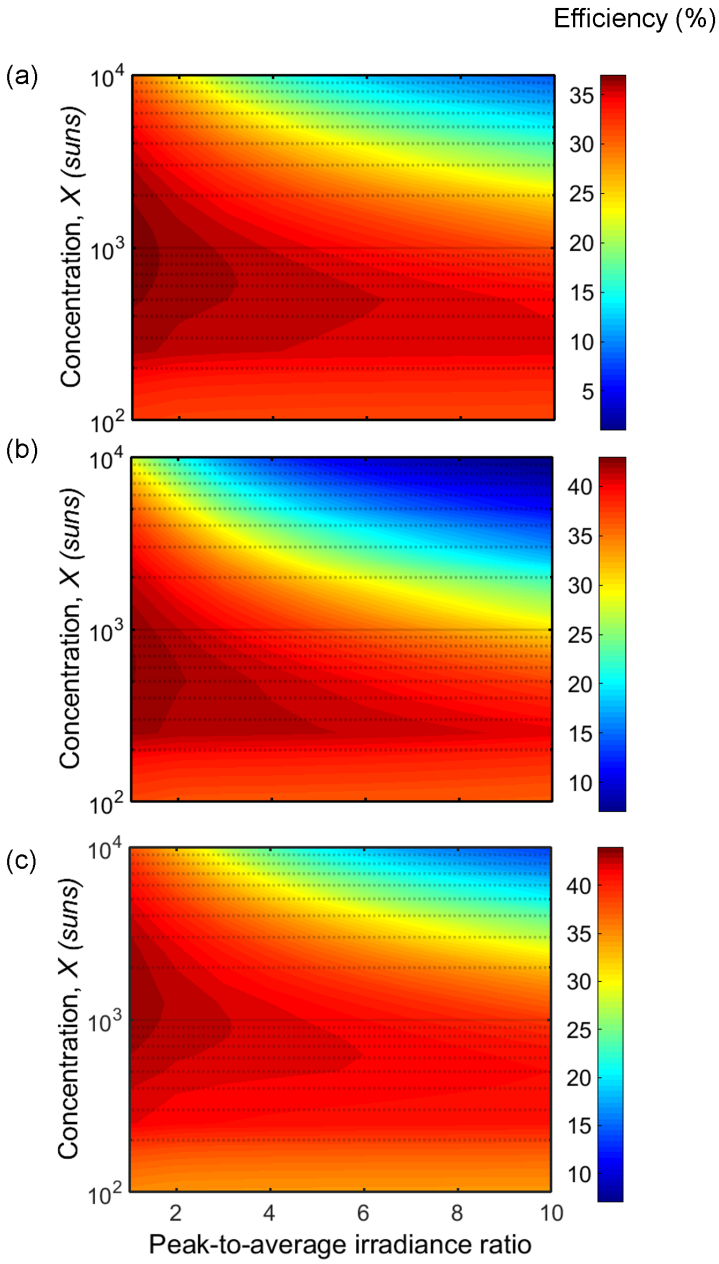

Figure 3.10: *Effect of nonuniform illumination profiles under concentrations from 100 to 10000 suns for (a) 3JLM (b) 3JIMM, and (c) 4JLM designs. The degree of nonuniformity varies with peak-to-average irradiance ratios. All simulations are done for a 1 cm^2 area cell with 5% shading.*

The results indicate a reduction in efficiency with an increase in the degree of nonuni-

formity (PAR values) for all the designs. This reduction is further pronounced with an increase in concentration, pointing to an increase in the series-resistance losses with an increase in the peak, localized current densities. The effect is more noticeable in the case of the 3JIMM cell (Figure 3.10 (b)), where there is $> 10\%$ drop in absolute efficiency at PARs > 6 for concentrations above 1000 suns. The 3JLM shows the least sensitivity to nonuniform illumination with an efficiency reduction of $< 5\%$ at the same PAR. The 4JLM efficiency drops by about 7% under the same conditions. This implies that the reduction in efficiency based on the degree of nonuniformity is design-dependent and concentration-dependent.

3.3.3 Effect of spectrally varying spatial profiles

Typical MJSC structures are optimized for operation under the standard AM1.5D spectrum. However, concentrating optics tend to modify the spectral input, thereby affecting the performance of MJSCs. Spectrally nonuniform profiles can be also generated due to the material properties of the optical system components. For example variation in refractive index with wavelength can lead to chromatic aberration effects which vary the focal point and lead to current mismatch. This is specifically seen in designs using refractive Fresnel lenses [75].

In this section, the sensitivity of the three designs to nonuniform spectral profiles is evaluated. While the same profile was used for all subcells within the MJSC to simulate spatial nonuniformities (in the previous section), Gaussian illumination profiles with different PARs on each subcell have been used to simulate spectrally varying spatial profiles

within an MJSC. This allows for the representation of various types of CPV optics and its effect on the performance of MJSCs.

Figure 3.11 shows the results with the 3JLM design. The bottom subcell is significantly overproducing in this design, so its effects have been ignored. PARs of 2 and 3 are chosen for the top two subcells in order to depict a realistic CPV optic, potentially using a homogenizer which is not flattening the illumination profile completely. Typically, for a lens-based CPV optic, subcell 1 would receive an illumination profile with a higher PAR than subcell 2 if the cell is placed closer to the lens than optimal. Similarly, as the cell is moved away from the lens, the PAR on the middle subcell will be increased [76]. Simulation results indicate that the efficiency is equally sensitive to variations in profiles over subcells 1 and 2, implying that the optics could work in either of the scenarios equally effectively without incurring a significant loss in efficiency.

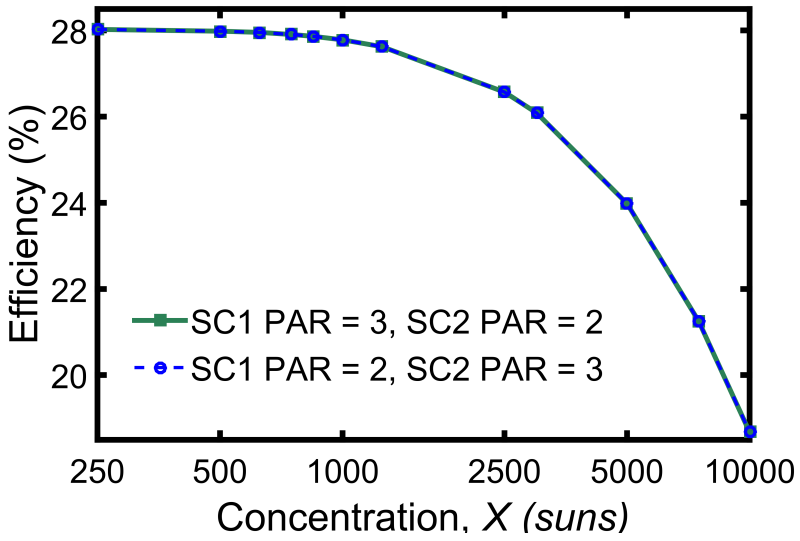

Figure 3.11: *Impact of a spectrally varying spatial profile on the 3JLM cell. Since the bottom subcell is overproducing, its effect is neglected and a uniform profile is assumed. PARs are varied for subcell 1 (SC1) and subcell 2 (SC2). Lines are a guide to the eye.*

Figure 3.12 shows the response of the 3JIMM cell to different profiles. In this case, all the three subcells are almost current-matched, so the response of the bottom subcell cannot be ignored. Different combinations of PARs have been simulated for the three subcells. While all the illumination profiles produce similar results, the response of the profile with PAR = 3 on the middle subcell and PAR= 2 on the bottom subcell is remarkable and requires further investigation. The simulations indicate that series resistance effects dominate even at 250 suns concentration, supressing the efficiency to be lower than the other profiles.

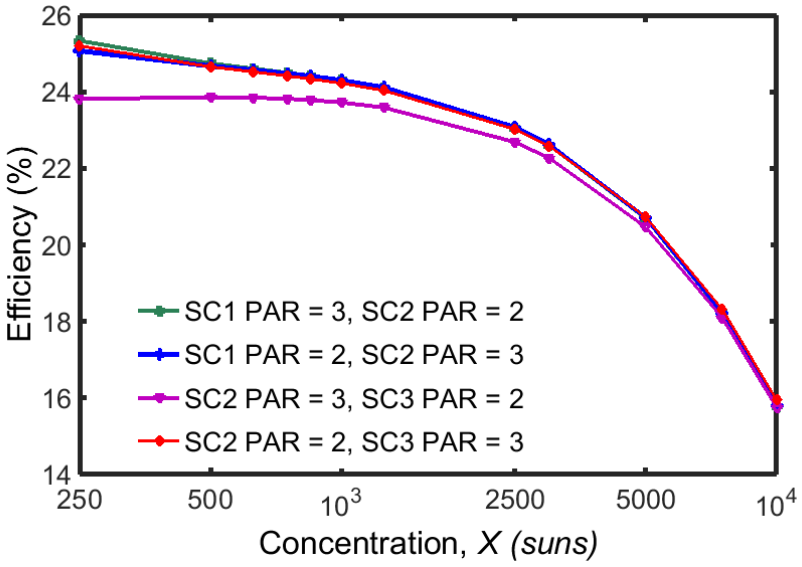

Figure 3.12: *Impact of a spectrally varying spatial profile on the 3JIMM cell. Since all the subcells are current matched, PARs are varied for all the three subcells to determine sensitivities to spectral variations.*

In order to analyze this further, the sheet resistance of the middle subcell has been reduced. Efficiencies at 1/2, 1/4 and $1/8^{th}$ of the initial middle subcell sheet resistance are presented in Figure 3.13. An increase in efficiencies when decreasing is evident from the simulations, indicating that an enhancement in efficiency $> 0.7\%$ absolute is possible for concentrations up to 1000 suns if the sheet resistances of the middle cell are reduced to an eighth of the original value. Reducing the sheet resistance of the bottom subcell (R_{SC3}) by to $1/8^{th}$ of the initial values does not impact the overall cell efficiency. Since the profile on the top-subcell is uniform, and the bottom subcell receives a PAR of 2 and has no impact on overall efficiency, it is evident that the middle subcell is the limiting subcell. It can be inferred that reducing the sheet resistance of the current-limiting subcell

would imply reduced loss penalties due to spectrally varying spatial profiles. The need to optimize cell structures assuming nonuniform spectral and spatial variations is therefore emphasized. An important aspect to highlight is the overall reduction in efficiency from 42.5% under uniform illumination at 1250 suns to about 25% under this profile. While the spatial profiles (PAR=3) alone caused an absolute efficiency reduction of 3.5%, the spectrally varying profile caused an 11% further reduction. This indicates that focal point changes with wavelength, causing a spectrally varying profile, should be avoided to prevent these loss penalties.

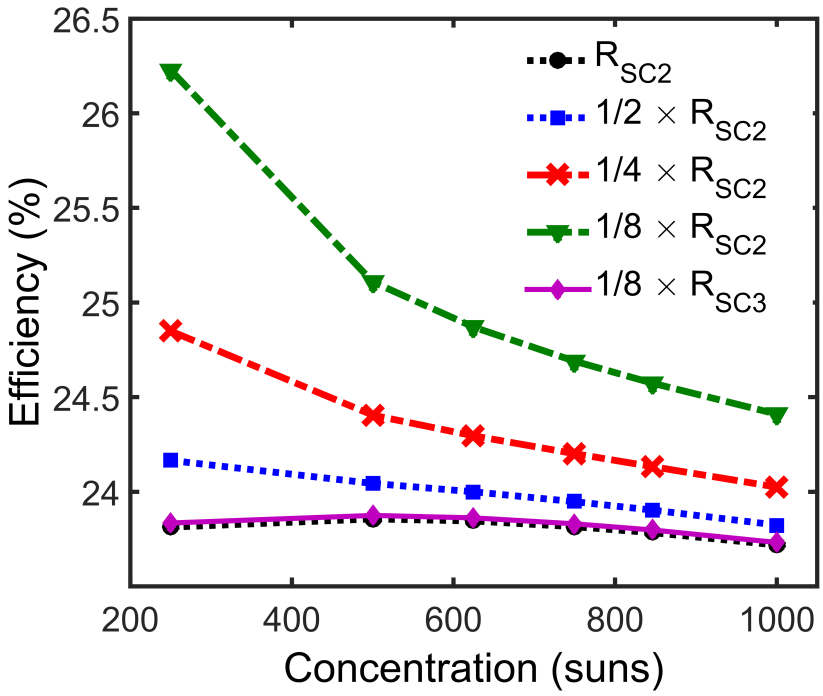

Figure 3.13: *Impact of varying the sheet resistance of the 3JIMM middle subcell. Both the emitter and base resistances of the subcell 2 are varied simultaneously. Impact of varying the sheet resistance of subcell 3 is also plotted for comparison.*

Lastly, the 4JLM design is analyzed for spectrally varying spatial profiles. Figure 3.14

illustrates that since subcell 4 is current matched with subcell 1, the bottom subcell limiting conditions cannot be ignored for this design as well. A PAR = 3 seems to affect SC1 the least and so this is the desired configuration to minimize losses. All the other combinations have greater penalties than this configuration. Again, the loss penalty is > 18% from uniform illumination conditions at 1250 suns.

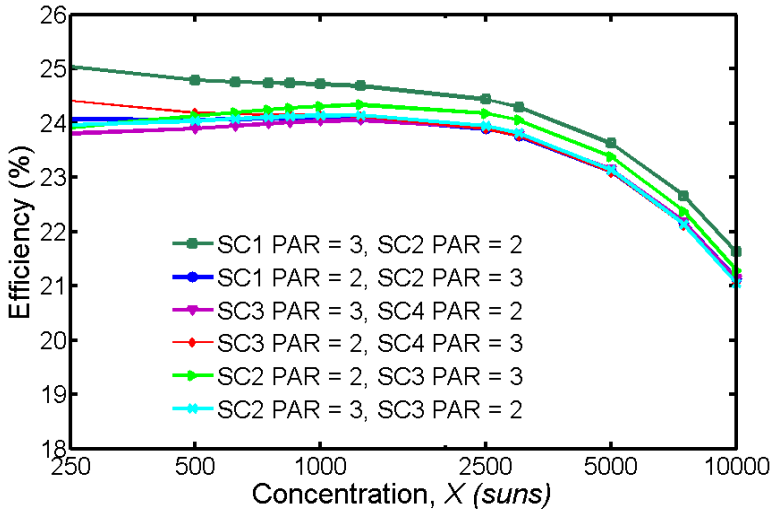

Figure 3.14: *Impact of a spectrally varying spatial profile on the 4JLM cell. In order to see the effect of spectral variations on all subcells, PARs are varied for all the four subcells.*

3.3.4 Optimization of finger spacing

Electrical contacts on a solar cell are realized by using metallic bus bars on the edges and metal *fingers* perpendicular to the bus bar. These contacts create shaded areas underneath with no photocurrent generation. In the areas devoid of electrical contacts, lateral resistances play an important role in current conduction. Larger finger spacing implies higher losses due to lateral resistance, leading to a loss in efficiency. An increase in the number

of fingers implies a larger shaded area. Therefore, a trade-off exists between shading and series resistance losses, and so optimization of finger spacing is necessitated to maximize efficiencies. For uniform irradiance, a linear grid with even finger spacing achieves maximum extraction efficiency regardless of such losses. This is not the case for non-uniform irradiance, where the consequent non-uniform current production within each subcell also leads to lateral currents that exacerbate carrier recombination. In this section, an approach to optimize finger spacing in order to enhance system efficiencies is proposed, both under uniform and nonuniform illumination.

In order to optimize finger spacing, the solar cell conversion efficiency is assumed to be a unimodal objective function with one maximum. A derivative-free optimization approach is adopted to maximize cell efficiency. In order to reduce the number of iterations and for a faster convergence, a Golden-section search algorithm is used. Finger spacings range from 50 μm to 300 μm, for a shading range of $\sim$2% to 10%, which is typical for solar cell designs. Finger width is fixed at 5 μm. Convergence of the optimization process is ensured by requiring the absolute change in efficiency to be less than 0.01%; spacing increments are 3 μm. Eight to ten iterations are sufficient to achieve convergence. The optimization process under both uniform and nonuniform illumination is presented under varying concentrations.

(a) Under uniform illumination

Under uniform illumination, all the subcells receive the same amount of irradiance. Spectrally varying profiles are ignored in these simulations. Figure 3.15 shows efficiency as a

function of finger spacing at concentrations from 250 to 2500 suns under a uniform illumination profile. The contour plots for each design reveal that cell efficiency reaches a maximum value at each concentration for a specific finger spacing.

Figure 3.15 (a) shows the efficiency as a function of concentration and finger spacing for the 3JLM design. The optimal finger spacing at 500 suns is found to be 120 μm. However, at 1000 suns the optimal finger spacing is reduced to 95 μm. It is evident that this cell can perform near optimally, without much loss in efficiency ($< 0.2\%$), at both 500 and 1000 suns if the fingers are spaced from 95 to 120 μm. At 2000 and 2500 suns, however, the cell needs to be designed with more closely spaced fingers (optimal spacing is 75 μm and 72 μm respectively) in order to get the best possible efficiency. A similar trend is reported in an NREL technical report [77]. An increase in the "blue" area in the contour plot at higher concentration indicates that the penalty for using a non-optimal spacing is greater at higher concentrations (2000 and 2500 suns) than at lower concentrations (500 and 1000 suns). If the cell is designed with a 120 μm spacing and operated under uniform illumination at a concentration of 2500 suns, a 1.3% absolute loss in efficiency is observed as compared to that obtained with the optimal spacing.

Amongst all the three MJSC designs, the 3JIMM design (figure 3.15 (b)) shows a greater sensitivity to variation in finger spacing. This sensitivity increases even further, with an increase in concentration, as compared to the other two designs. This design also favors a lower optimal spacing at all concentrations, with 95 μm optimal spacing at 500 suns, decreasing to $<$65 μm at 2500 suns. If the TJIMM is designed with a 95 μm spacing and operated under uniform illumination at a concentration of 2500 suns, a $>$1.7% absolute

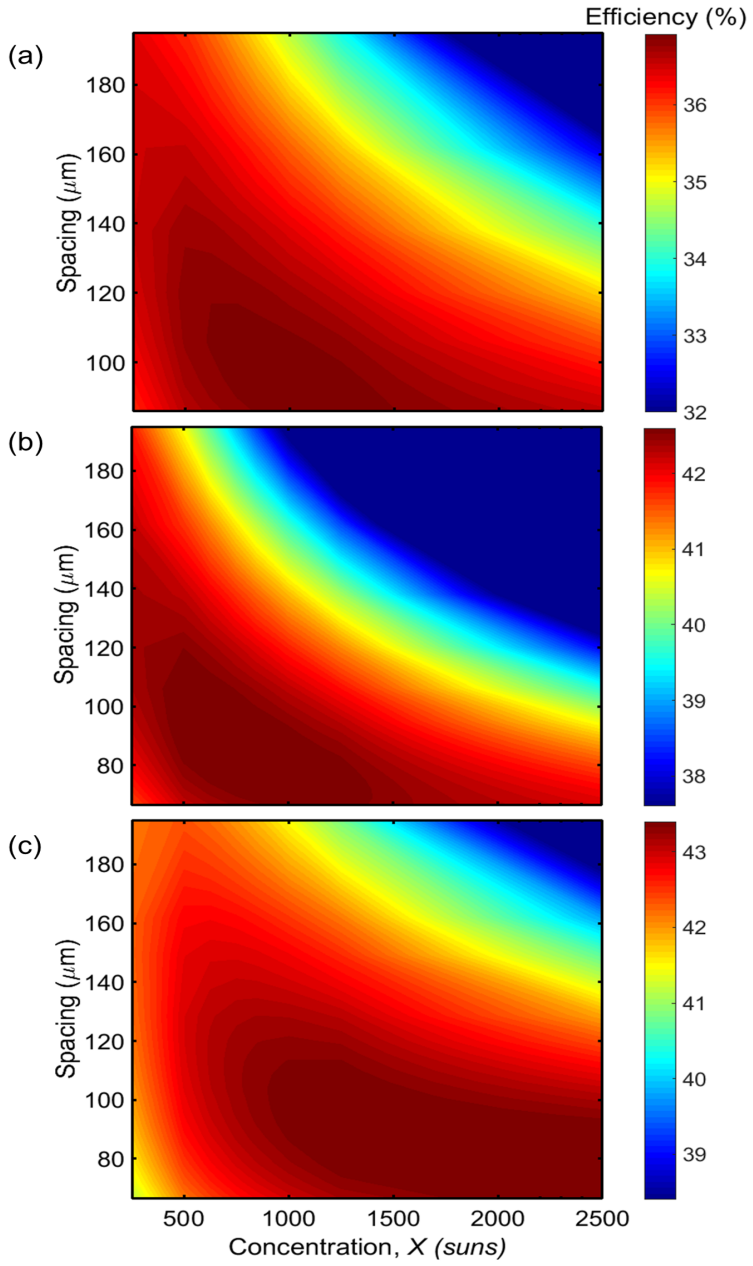

Figure 3.15: *Contour plot showing efficiency as a function of finger spacing and concentration under uniform illumination under 250 to 2500 suns for (a) the 3JLM , (b) the 3JIMM and (c) the 4JLM design. The color bars indicate cell efficiencies over a 5% range.*

loss in efficiency is observed as compared to that obtained with the optimal spacing.

The 4JLM shows trends similar to the 3JLMM with optimal spacings being 120 μm, 100 μm and 72 μm at 500, 1000 and 2500 suns respectively. The loss penalty for using a cell, optimized for 500 suns and operated under 2500 suns, is 1.2% absolute.

These results also indicate that the identical spacings can be used for a 4JLM and the 3JLM designs as long as these MJSCs are operated under uniform illumination, indicating that the same shadowing mask can be used for both the designs. The optimal spacing differs though in the case of the 3JIMM indicating that a specifically optimized mask is required for this design to achieve maximum efficiency.

(b) Under nonuniform illumination

Grid designs and finger spacings are typically optimized for operation under uniform illumination, although the profiles are nonuniform in reality. Continued reliance on uniform irradiance grid designs are therefore cause for concern [73], motivating analyses of more realistic scenarios.

(i) Uniform spacing under nonuniform illumination

To model nonuniform illumination, Gaussian profiles with different PARs are used to represent different types of concentrating optics. Efficiency optimization is performed for PARs of 3, 6 and 10 at various concentrations across the range of finger spacings for all the three designs. A PAR of 1 represents uniform illumination by an ideal concentrating system, while a PAR of 10 may represent a system with extremely high degree of nonuniformity.

An intermediate case of PAR = 5 may occur if the CPV optics consist of only a primary Fresnel lens element and no secondary homogenizer. Note that while the total intensity of each irradiance profile is kept constant, chromatic aberration effects are ignored in the optimization. This implies that current mismatch between top, middle and bottom subcells is neglected.

Since the 3JIMM design showed maximum sensitivity to finger spacing, the performance of this design is determined between 250 to 2500 suns. Figure 3.16 shows pseudocolor plots (p-plots) for this TJIMM design. Efficiency varies as a function of spacing and concentration for 3 different illumination profiles. While PAR = 1 represents an ideal, uniformly illuminated case, PAR = 3 may represent an optic which is not fully homogenizing the illumination profile. PAR = 6 may represent an optical train with a refractive Fresnel without a secondary homogenizing element.

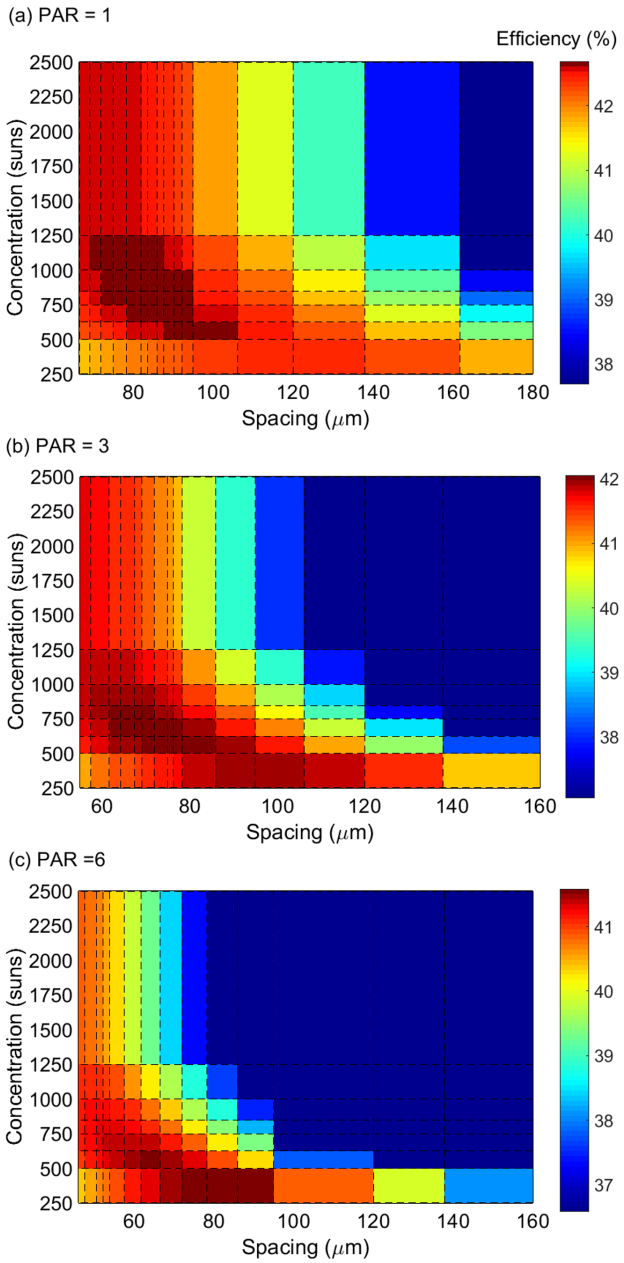

Figure 3.16: *Pseudocolor plots, for the 3JIMM design, showing efficiency as a function of finger spacing and concentration under PARs of 1, 3, and 6. PAR =1 represents uniform illumination while a PAR =6 shows an extreme case of nonuniformly illuminated cell. Color bars represent efficiency over a 5% range. While the concentration values are similar among all the plots, the spacing range varies, in order to indicate that the optimal spacing shifts towards lower values at higher PARs.*

These plots clearly indicate the optimal spacing trends across different PARs. The optimal spacing is seen to decrease with both increasing nonuniformity and increasing concentration, and the efficiency is likewise reduced. Comparing the plots at PAR = 1 and PAR = 3, at 500 suns, the optimal spacing decreases from 95 to 78 μm, while at 1250 suns it drops from 71.9 to 57.5 μm. At 500 suns, for a PAR = 6 (figure 3.16(c)), the efficiency at the spacing optimized for uniform illumination (95 μm) is about 1.2% absolute lower than it would be at its optimal 66.4 μm spacing; at 1000 suns, the efficiency at the optimal uniform spacing of 78.3 μm is about 2.2% absolute lower than it would be at its optimal 50.5 μm spacing. This implies that efficiency enhancement is possible if the finger spacing is optimized on the basis of the nonuniform illumination profile instead of the ideal uniform illumination profile.

Similar studies have been done for the 3JLM and the 4JLM designs. Since 4JLM and 3JLM showed similar sensitivities to variations in finger spacing, the 4JLM data is reported in Figure 3.17 for the sake of brevity. The data is shown under different concentrations and for varying degrees of nonuniformity. Details on the 3JLM optimization have been included in [64].

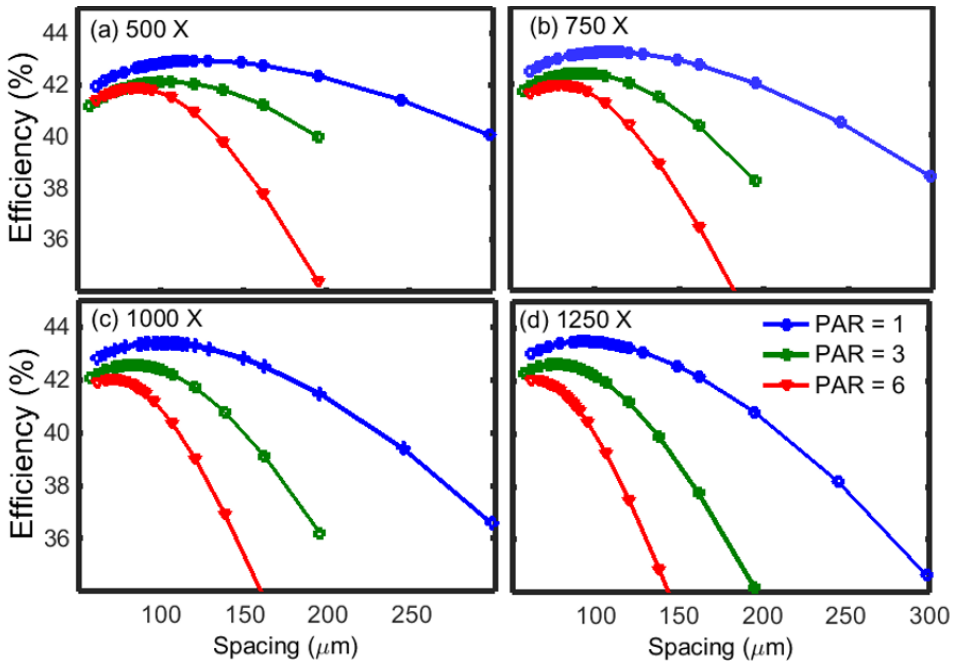

Figure 3.17: *Efficiency as a function of finger spacing under PARs of 1, 3, and 6 at four different concentrations for the 4JLM design.*

Table 3.2 presents the optimal finger spacings for the 3JIMM and the 4JLM designs under different PARs.

Table 3.2: *Optimal finger spacings for the 3JIMM and the 4JLM designs under varying degrees of nonuniform illumination and concentration (X). A PAR = 10 has been included to illustrate an extreme case of nonuniform illumination.*

Optimal finger spacing (μm)				
(a) 3JIMM				
***X* (suns)**	**PAR = 1**	**PAR = 3**	**PAR = 6**	**PAR = 10**
500	95.0	78.3	66.4	53.8
625	92.1	75.0	61.6	50.6
1000	78.3	61.6	50.6	41.5
1250	71.9	57.5	45.0	37.5
(b) 4JLM				
***X* (suns)**	**PAR = 1**	**PAR = 3**	**PAR = 6**	**PAR = 10**
500	120.0	106.1	95.0	82.0
625	112.7	97.0	85.9	75.0
1000	100.3	82.0	71.9	59.5
1250	92.0	75.0	66.4	53.8

In the case of the 4JLM, at 500 suns, for a PAR = 6 (Figure 3.17), the efficiency at the optimal uniform spacing of 120 μm is about 0.4% absolute lower than it would be at its optimal 95 μm spacing; at 1000 suns, the efficiency at the optimal uniform spacing of 100 μm is about 1.4% absolute lower than it would be at its optimal 72 μm spacing. The results clearly illustrate that an increase in concentration and in nonuniformity have an increasingly significant effect on the conversion efficiency of the solar cell but the loss penalties can be partly mitigated by the use of an optimal finger spacing customized for a

specific nonuniform illumination profile.

It can also be seen that the design sensitivities to nonuniform illumination may govern the optimal spacing for an MJSC. Comparing the 3JIMM and the 4JLM designs, it can be observed that the 3JIMM design favours narrower spacings than the 4JLM design and is more sensitive to deviations from optimal spacing. This implies that the 3JIMM would benefit more by use of optimal spacings based on the degree of nonuniformity. For the 3JIMM, an efficiency enhancement of >5.5% absolute is possible under 1250 suns and a PAR =10, if the optimal spacing corresponding to the nonuniform illumination profile is used instead of the spacing suggested under uniform spacing for this concentration. For the 4JLM, however, the enhancement is 3.3%.

(ii) Nonuniform finger spacing under nonuniform illumination

In order to further improve the efficiency of the cell exposed to a nonuniform irradiance profile, a nonuniform grid spacing is investigated to ascertain if unevenly spaced fingers enhance cell efficiency. For this analysis a comparison of the 3JLM and the 3JIMM design is performed at different concentrations.

To reduce computational complexity, the cell is virtually divided into a number of segments of equal area. Spacing is uniform within a segment but differs between segments. For example, consider a solar cell virtually divided into ten segments (say, S_1 to S_{10}). Since the segments closest to the center of the cell will receive higher illumination, the fingers should be more narrowly spaced at the center of the cell than at the edges. Also, since Gaussian irradiance profiles have been used to represent nonuniform illumination, a

symmetric spacing distribution can be used. For example, the spacing for the two outermost segments, S_1 and S_{10} are the same.

Simulations show a negligible change in efficiency (<0.01%) when the number of segments is increased beyond ten. Therefore, ten segments are used for our model. Each segment consists of a number of functional blocks given by

$$Y = m * SegN + C, \tag{3.9}$$

where $SegN$ is the segment number for the symmetric left half of the cell, m is the slope of the linear profile, and C is a constant.

By varying the values of m and C, the number of functional blocks, and hence the finger spacing, is varied. Changing m varies the spacing between segments more drastically than changing C. In order to implement this in SPICE, recalculation of resistance values for each segment, and for intermediate areas between segment transitions, is required.

Maximum slope ($MaxM$) and constant ($MaxC$) values are set to 10, and maximum efficiencies are obtained as the values of m and C are varied between 1 and 10, yielding optimal configurations for all irradiance profiles and concentrations. Figure 3.18 shows results for the 3JLM with a Gaussian irradiance profile of PAR = 6 at 1000 suns and 2000 suns. At 1000 suns, a maximum efficiency (η_{max}) of 35.6% is obtained at $m = 2$ and $C = 4$. In this case the spacing varies from 162 μm at the cell edges to 66 μm at the cell center. At 2000 suns, $\eta_{max} = 35.3\%$ is obtained at $m = 3$ and $C = 4$. In this case the spacing varies from 137 μm at the cell edges to 48 μm at the cell center.

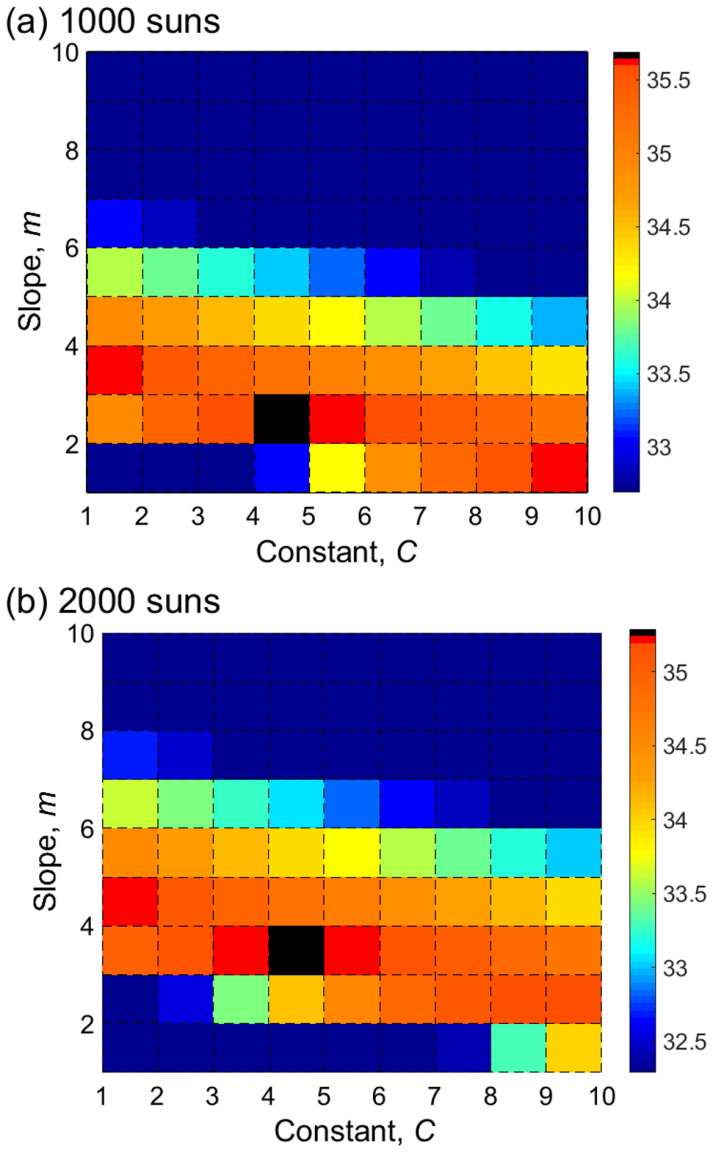

Figure 3.18: *Efficiency as a function of slope* m *and constant* C *under a Gaussian irradiance distribution (PAR = 6) at (a) 1000 and (b) 2000 suns for the 3JLM design. The color bar indicates the efficiency values(%) obtained with each combination and spans over a 3% range.*

Figure 3.19 shows the results for the 3JIMM with the same degree of nonuniformity at 1000 and 2000 suns. In this case, at 1000 suns, a maximum efficiency (η_{max}) of 41.3% is

obtained at m and $C = 3$. In this case the spacing varies from 162 μm at the cell edges to 51 μm at the cell center. At 2000 suns, $\eta_{max} = 35.3\%$ is obtained at $m = 4$ and $C = 3$. In this case the spacing varies from 137 μm at the cell edges to 38 μm at the cell center.

A comparison of the 3JLM and 3JIMM results suggests that the 3JIMM design favors a more narrower spacing at the center of the cell. It is also evident that at higher concentrations the spacing towards the center of the cell is narrower even with the same PAR values. More results for a 3JLM design obtained using this technique have been published in [78] and have not be included in this thesis for the sake of brevity.

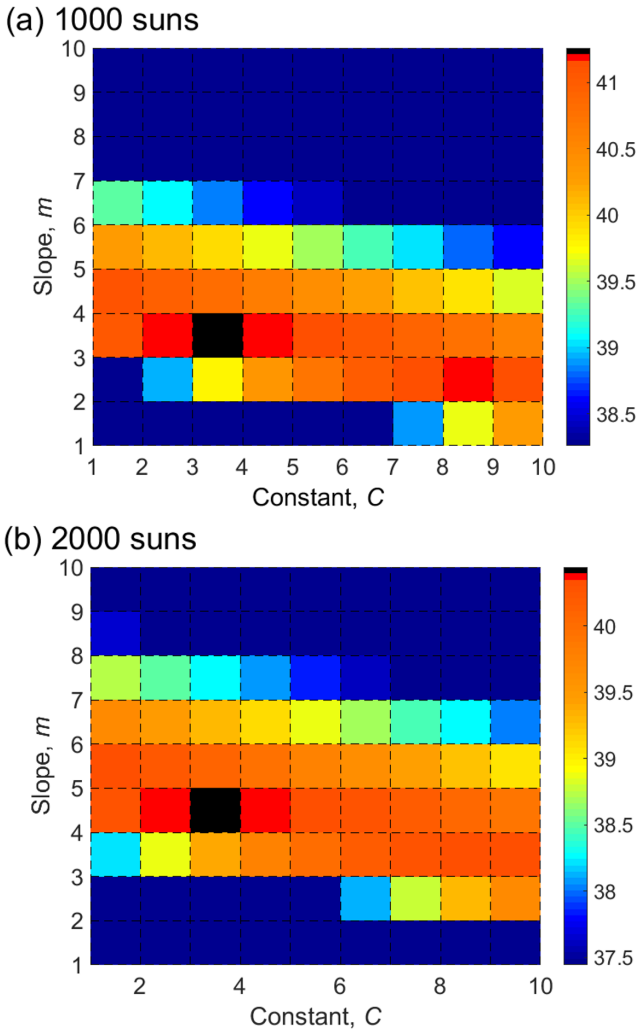

Figure 3.19: *Efficiency as a function of slope* m *and constant* C *under a Gaussian irradiance distribution (PAR = 6) at (a) 1000 and (b) 2000 suns for the 3JIMM design. The color bar indicates the efficiency values(%) obtained with each combination and spans over a 3% range.*

Figure 3.20 shows the optimal spacing profile as a function of segment position under nonuniform irradiance profile with a PAR = 6 at concentrations of 1000 and 2000 suns for the 3JLM and the 3JIMM designs.

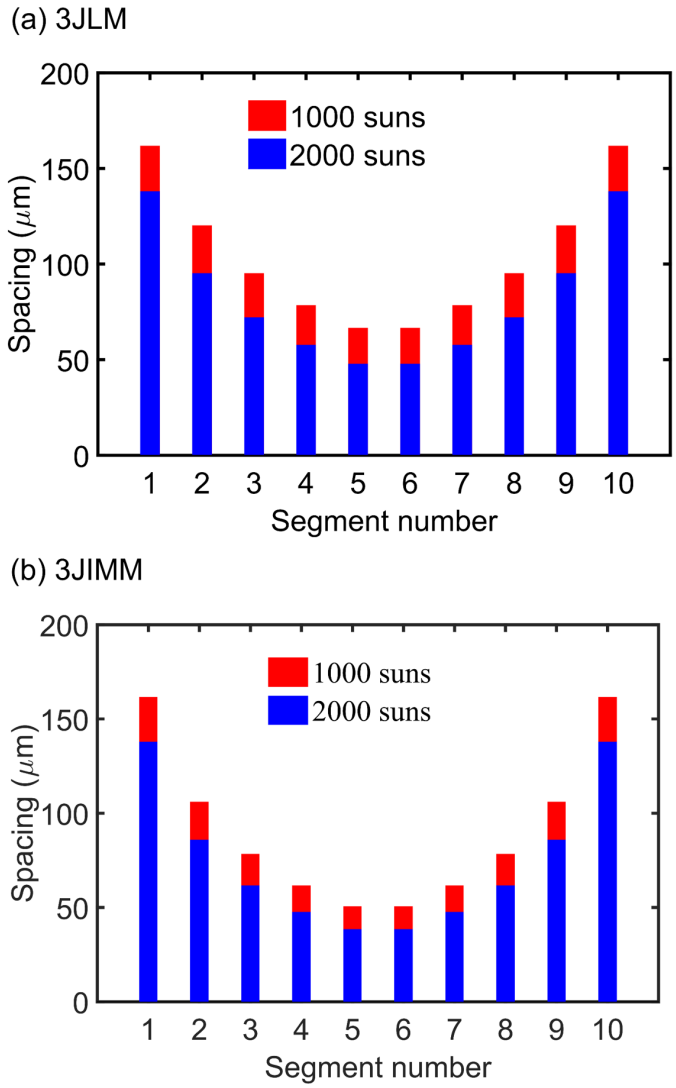

Figure 3.20: *Optimal nonuniform spacing profile at 1000 suns and 2000 suns under a Gaussian irradiance profile (PAR = 6) with the solar cell divided into ten equal segments for (a) the 3JLM and (b) the 3JIMM design.*

Similar simulations have been carried out for illumination profiles with PAR = 3. Table 3.3 shows the maximum efficiency for Gaussian profiles having a PAR of 3 and 6 at various concentrations with the 3JIMM design.

Table 3.3: *Maximum efficiency (η_{max}) comparison with uniform and nonuniform spacing under PAR = 3 and PAR = 6 at various concentrations (X) for the 3JIMM*

	PAR = 3		**PAR = 6**	
X	η_{max} **Uniform spacing** [%]	η_{max} **Nonuniform spacing** [%]	η_{max} **Uniform spacing** [%]	η_{max} **Nonuniform spacing** [%]
500	42.0	42.1	41.5	41.6
1000	41.9	42.0	41.0	41.3
2000	41.3	41.5	39.9	40.4

For lower concentrations and lower PAR values, the penalty for using uniform spacing is minimal. A similar result has been reported in [79] at 1000 suns. However, at a PAR $= 6$, a 0.3% and 0.5% absolute efficiency gain is observed at 1000 and 2000 suns respectively. This indicates that non-negligible efficiency enhancements are possible if nonuniform spacing is used for a nonuniform illumination profile. Not only does nonuniform illumination require a spacing optimized for a specific PAR but an added benefit can be obtained if nonuniform spacing is used corresponding to a particular profile, especially at high concentrations and high PARs.

3.3.5 Effect of smaller cell areas

With the intent of reducing costs and obtaining ultra-high efficiencies, CPV manufacturers are targeting MJSCs at very high concentrations. In order to minimize series resistance

losses, short-circuit currents need to be reduced. This can be achieved by using cells with smaller active areas. Simulations with uniform illumination profiles have been presented by Nishioka [63], with efficiency improvements with smaller cell areas. In this section, a brief set of results is presented to show the impact of smaller cell areas on cell efficiency, when the cell is illuminated with more realistic nonuniform illumination profiles. Two different cell areas are chosen for this simulation at two different concentrations. The 3JIMM design is chosen with cell areas of 1 cm^2 and 0.25 cm^2. The choice of the design is based on the previous results where the 3JIMM shows maximum sensitivity to nonuniform illumination profiles. The purpose of performing these simulations is to analyze if an enhancement in efficiency would be possible even at higher PAR ratios.

Figure 3.21 shows the simulation results with comparison of efficiencies for square 3JIMM cells with 10 mm and 5 mm sides. The finger spacings have been kept at 120μm and the results are presented at concentrations of 1000 and 2000 suns. It can be seen that >3% efficiency enhancement can be obtained at a PAR =3 at a concentration of 1000 suns. Loss penalties due to nonuniform illumination are partly mitigated by using smaller cell areas. The efficiency enhancements are more pronounced at 2000 suns. This indicates that smaller cell sizes can be used for very high concentration systems, even with high PARs. These results validated with cell measurements can be a valuable tool to minimize loss penalties at higher concentrations.

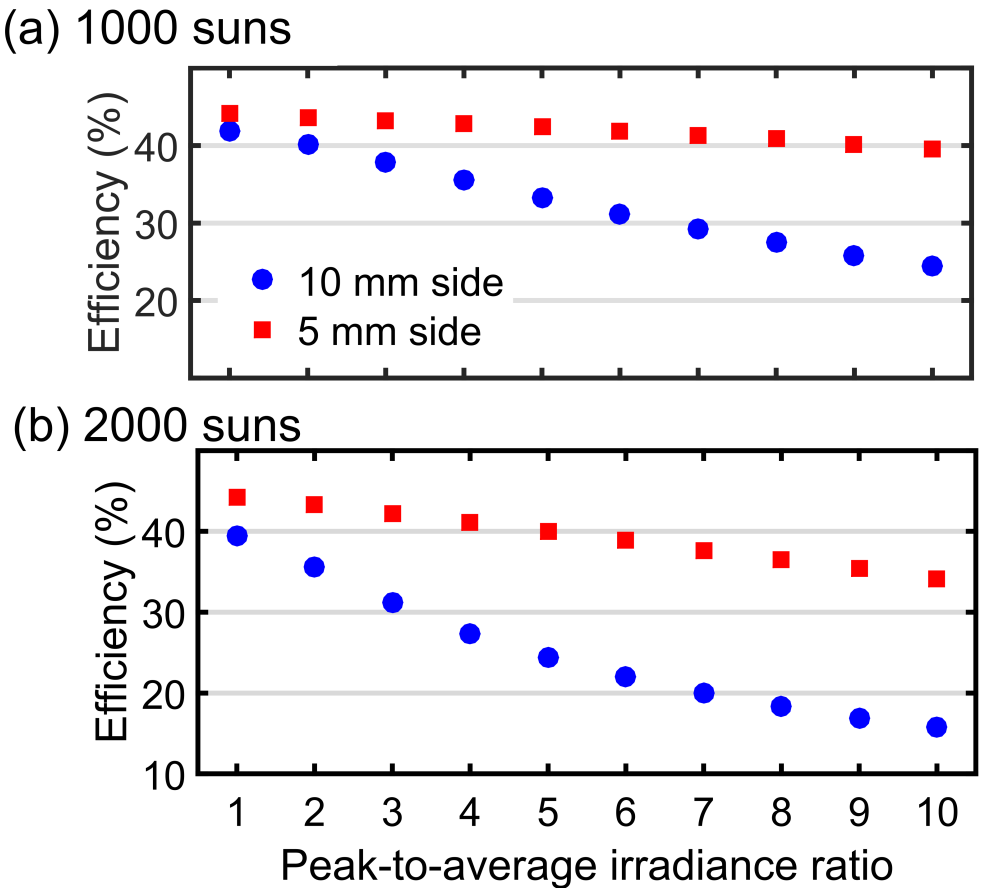

Figure 3.21: *Efficiency as a function of the peak to average irradiance values for 3JIMM cells of 2 different sizes at (a) 1000 and (b) 2000 suns concentration.*

3.3.6 Effect of luminescent coupling

Performance enhancement in solar cells can be also achieved by reducing radiative losses. Emitted radiation from higher bandgap junction can be captured by a subsequent lower bandgap junction. This coupling of light from one junction to another is referred to as *luminescent* or *radiative coupling*.

It is known that radiative recombination dominates over non-radiative in a good-quality

solar cell with the emission of light at the band edge of the material. The emissions can escape, get reabsorbed by the emitting junction or get coupled into the subsequent junction. If the emitted photons get reabsorbed in the adjacent junction, the photocurrent of that junction would be increased [80]. This is illustrated in Figure 3.22 for a three-junction solar cell. Luminescent coupling may significantly affect the process of cell design and optimization [81]. It may aid in reducing the impact of spectral mismatch and may consequently have a favourable impact on cell performance at high concentrations [82].

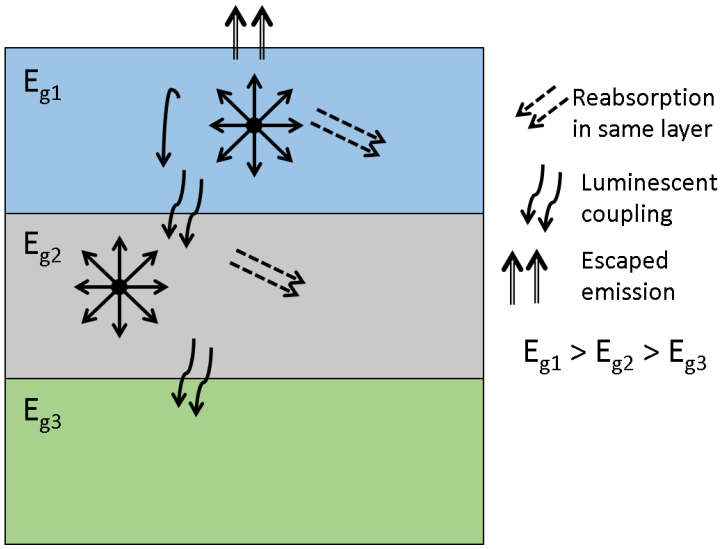

Figure 3.22: *Luminescent coupling in a three junction solar cell.*

Inclusion of the effects of luminescent coupling may improve efficiencies. In order to quantify the effects of luminescent coupling, the 2-D model has been modified as shown in Figure 3.23. The effect of luminescent coupling has been modeled by adding a voltage-dependent current source in parallel with the recombination diodes as proposed by [83]. These current sources have been added to subcells 2 and 3. The model allows to simulate radiative emissions from subcell 1 to be reabsorbed in subcell 2 and from subcell 2 to

subcell 3. The current through this source is defined as:

$$I_{LC} = \eta_c . I_{0_{hbg}} . e^{qV_{hbg}/KT} \tag{3.10}$$

I_{LC} is the current through the source, $I_{0_{hbg}}$ is the saturation current through the recombination diode of the higher bandgap subcell above and V_{hbg} is the voltage across the diode of the higher bandgap cell. η_c is the coupling coefficient. The maximum measured value of the coupling coefficient is 0.5 for three-junction cells [80] but the simulations are limited to 0.3 to present a realistic scenario. Reabsorption has been restricted to the subcells directly above to simplify modeling and reduce computational times.

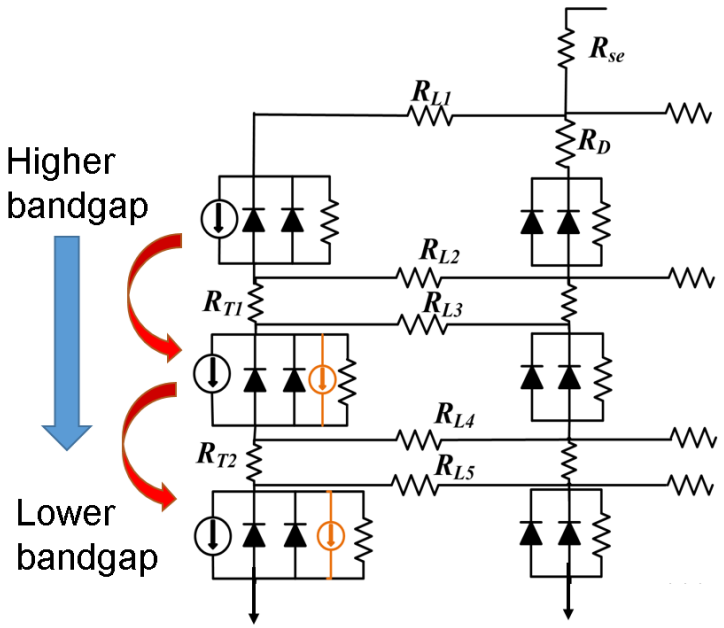

Figure 3.23: *Implementation of luminescent coupling in the distributed circuit model for a three junction solar cell. Photons emitted due to radiative combination from the higher bandgap subcell are absorbed by the lower bandgap subcell. An additional current source is added to the second and third subcell circuits to implement luminescent coupling.*

In order to evaluate the effect of luminescent coupling, I-V curves are calculated under two spectrally varying spatial profiles for the 3JIMM design at 1250 suns. The 3JIMM design is chosen as all the subcells are almost current matched under the AM1.5 spectrum and so any of these subcells can be the current-limiting subcell in this design depending on the illumination profile and may potentially benefit due to the coupling. For the first profile, the top subcell receives a PAR = 2 and the middle subcell a PAR = 3. The bottom subcell receives uniform illumination. The coupling coefficient between subcell 1 and 2 (η_{12}) is varied from 0 to 0.3. Figure 3.24 shows the I-V curves generated with different coupling

coefficients. Inset shows the Gaussian profiles used for the two subcells. The I-V curve under uniform illumination with no coupling is also included for comparison. If the spectral variations are neglected and all cells receive the same irradiance profile with PAR = 3, a reduction in fill-factor and V_{oc} is observed. With the spectral variations included, for a profile with subcell 1 receiving a PAR =2 and subcell 2 receiving a PAR = 3, a large drop in J_{sc} is seen. This is primarily due to current-limiting by the cell with a higher PAR arising because of the series connection. If the lateral resistances are low, this effect can potentially be reduced. However, higher lateral resistances for the 3JIMM cell increase loss penalties. With the coupling coefficient changed to a non-zero value, there is a significant increase in the J_{sc} value. The effect of the luminescent coupling manifests by reducing the effective PAR of the profile and increasing the J_{sc}. In addition, since the recombination current is increased there is an increase in the open-circuit voltage as well.

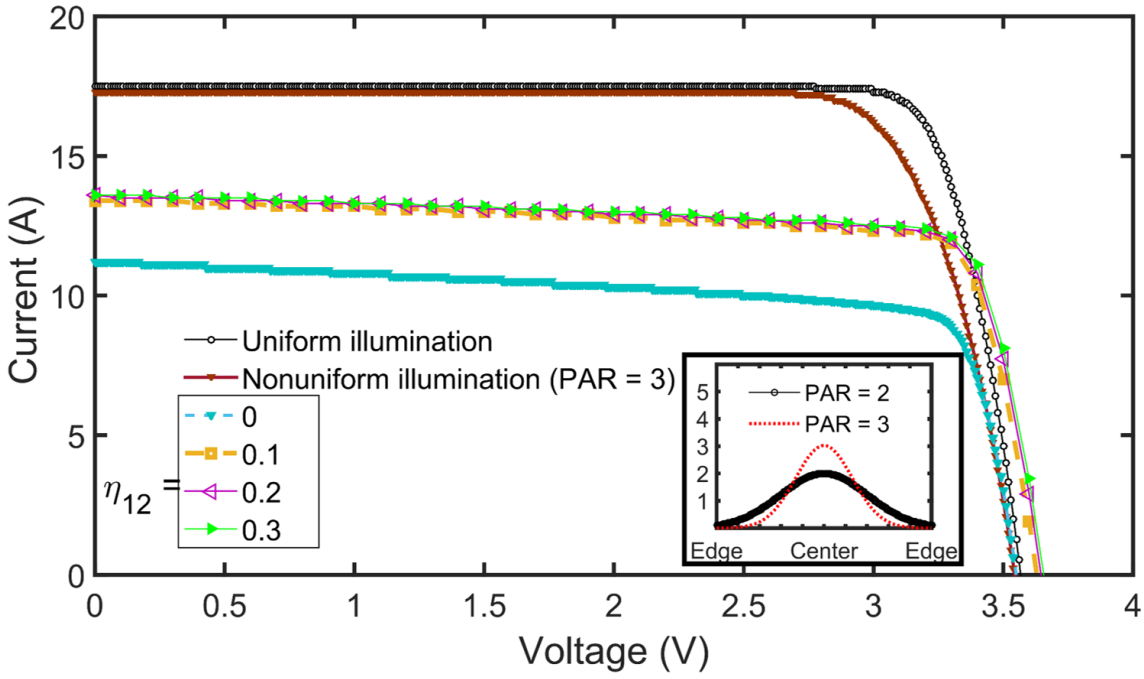

Figure 3.24: *I-V curves under uniform illumination and various nonuniform illumination profiles for the 3JIMM design under 1250 suns with the coupling efficiency from SC1 to SC2 (η_{12}) varied between 0 and 0.3. Inset shows the Gaussian irradiance profiles with PAR = 2 and PAR = 3. Higher PAR ratios imply higher localized currents towards the centre of the cell and almost no current generation towards the edges, making the corresponding subcell the current-limiting subcell in those localized areas.*

The second profile has the middle subcell receiving a PAR = 3 and the bottom cell receiving a PAR = 2. Figure 3.25 shows the I-V curves generated under this profile with the coupling coefficient between subcell 2 to subcell 3 (η_{23}) varying from 0 to 0.3. Again, since the bottom subcell is almost current-matched to the top two subcells, a PAR = 3 on the bottom subcell implies a localized current-reduction by this subcell towards the cell edge. The benefit of the luminescent coupling is observed again on the current as well as

the voltage values. The fill-factor is also improved.

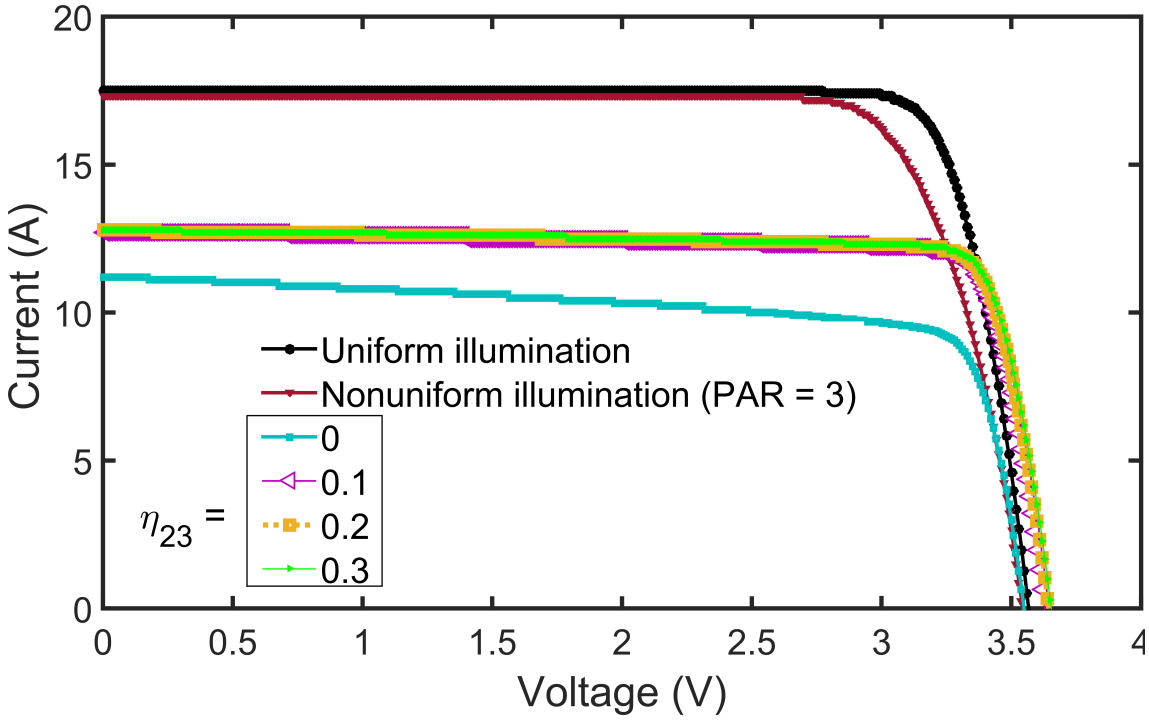

Figure 3.25: *I-V curves under uniform illumination and various nonuniform illumination profiles for the 3JIMM design under 1250 suns.*

Overall, absolute efficiency enhancements of >5% are obtained for both the illumination profiles at a coupling coefficient = 0.3. This efficiency enhancement is similar to the one calculated by Derkacs et al. [80] for a three-junction cell and could be specially beneficial for designs using a single-stage Fresnel lens only system, as the losses due to material dispersion are more pronounced in such systems leading to a focal point variation and varying spatial profiles depending on wavelength.

3.4 Summary

The most significant conclusions drawn from previous discussions are summarized here:

1. Distributed circuit modeling is a means to assess the effects of nonuniform illumination cause by CPV optics. While 1-D models are limited in their abilities to simulate distributed effects, the 3-D models, potentially very powerful, use high computational resources and time. Therefore, a 2-D distributed circuit model parametrized for a three-junction lattice matched, three-junction lattice mismatched (inverted metamorphic) and four-junction, lattice matched design is proposed.

2. MJSCs are affected by spatial and spectral variations depending on the design, with the design having higher lateral resistances suffering from significant loss penalties.

3. The application of 2-D model to nonuniform illumination profiles shows a reduction in efficiency based on the degree of nonuniformity (PAR values) for all the three MJSC designs, with the 3JIMM design being the most sensitive to nonuniform illumination.

4. It can be concluded that reducing the sheet resistance of the current-limiting subcell would minimize loss penalties due to spectrally varying spatial profiles. Therefore, cell structures should be optimized depending on the localized current distributions due to the optics.

5. Our results indicate that under uniform illumination, the finger spacing needs to be optimized for the specific system concentration. An unoptimized cell can lead to a high loss penalties due to series resistance effects.

6. Under nonuniform illumination, the effect of finger spacing on solar cell efficiency can be significant, particularly at high concentrations. Efficiency enhancements can be achieved if finger spacing is optimized on the basis of the specific nonuniform illumination profiles targeted for a specific MJSC design.

7. Nonuniform finger spacings can be used for nonuniform illumination conditions. At lower concentrations, the penalty for using evenly spaced fingers is negligible. However, very high concentration CPV systems with high peak-to-average ratios can benefit from a customized, nonuniform finger spacing.

8. Efficiency enhancements are potentially possible under nonuniform illumination profiles if smaller sized cells are used.

9. The inclusion of luminescent coupling leads to >5% absolute efficiency enhancement for the 3JIMM design, implying that losses due to spectrally varying spatial profiles can be partly mitigated by designing structures which allow for luminescent coupling to the lower bandgap subcells.

Chapter 4

CPV optics

4.1 Introduction

Mass deployment of the CPV technology is contingent on the high efficiency, greater reliability and a lower cost of its modules. Concentrating optics play a major role in achieving these targets. Achieving high concentrations to reduce system costs is certainly an important function of the optics, but it is not the only requirement for its design. Features such as a high acceptance angle and uniform irradiance distribution impact module efficiencies significantly and limit concentration. Even if such limitations are avoided, concentration is limited due to the very nature of geometric optics.

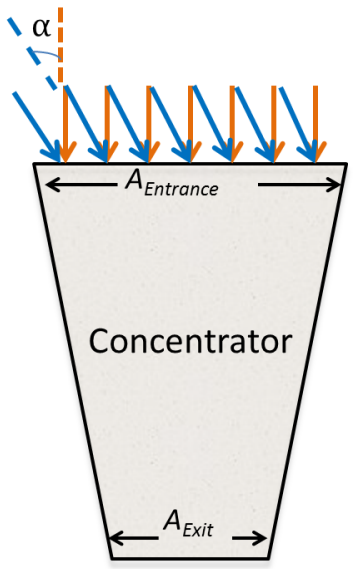

Figure 4.1: *A concentrator showing the incident rays entering the entrance aperture. The concentrator focuses sunlight on to the exit aperture where the solar cell is placed. Rays incident at non-normal angles (α) may still be captured by the concentrator depending on its acceptance half-angle.*

4.2 Limits to concentration

Concentrating systems focus light on to smaller area solar cells thereby increasing the incident flux on the cell by a *geometric* concentration factor, X, or the number of *suns*, defined by the ratio of the entrance aperture area ($A_{Entrance}$) to the exit aperture area (A_{exit}). Figure 4.1 shows a concentrator collecting sunlight over a large area and focusing it on to a solar cell. The exit aperture area is a fixed parameter depending on the size of the solar cell. Going by the principles of geometric optics, concentration has the same impact as extending the angular range of the sun. This implies that the concentration ratio X can be assumed to increase the half-angle of the sun from θ_{sun} to θ_x and so for a spherical

concentrator the incident flux is enhanced by

$$X = \frac{\int_0^{2\pi} \int_0^{\theta_x} d\Omega}{\int_0^{2\pi} \int_0^{\theta_{sun}} d\Omega} \tag{4.1}$$

$$X = \frac{sin^2\theta_x}{sin^2\theta_{sun}} \tag{4.2}$$

Theoretically, maximum concentration occurs when θ_x =90° and so X=46050. In the same way, concentration limit for a cylindrical concentrator is given by

$$X = \frac{1}{sin\ \theta_{sun}} \tag{4.3}$$

In reality, however, concentration is limited by the performance of the optical system, existence of tracking errors and by the issue of coupling wide angle ray bundles into the small solar cell. Nonetheless, the promise of CPV technology has led to the development of both reflective and refractive concentrators at high geometric concentrations (X>200).

In this chapter, various aspects of optical design with regards to lens-based concentrator systems are studied. Figures of merit pertaining to a CPV system are discussed and ray-tracing-based optimization results are presented for single and double stage concentrator systems at concentrations of 846 and 1250 suns. The 846 suns concentration is chosen in order to compare system performance with a commercially available 846× CPV system. Since the MJSC designs presented in Chapter 2 are optimized for a 1000 suns concentration, assuming an 80% efficient optical system, the required geometric concentration for the

CPV optics would be 1250 suns. Therefore, the second system is designed for a 1250 suns geometric concentration.

4.3 Figures of merit

4.3.1 Optical efficiency

Optical efficiency is the most important figure of merit for a concentrating system due to its direct impact on module efficiencies. Optical efficiency is defined as the ratio of optical power obtained at the exit aperture of the concentrator (the PV cell) to the incident power on the entrance aperture [84]. It varies as a function of the incident spectrum, and by the efficiency of how the light ray is transmitted through the optical system. Optical efficiency measured as a function of incident wavelength is termed as the *optical transfer function* (OTF). Evaluation of the OTF on a design-by-design basis is essential to predict CPV system efficiencies and understand the losses. OTF is directly related to the system efficiencies, as it influences the as the short-circuit current as follows [85]:

$$J_{sc} = q \int EQE(\lambda).\ b(\lambda).\ OTF(\lambda)\ d\lambda \tag{4.4}$$

Here J_{sc} is the short-circuit current, q is electronic charge, $b(\lambda)$ is the incident photon flux density (incident spectrum is AM1.5D in this case) and OTF is the wavelength-dependent, optical transfer function.

This implies that a reduction in OTF lowers the number of photons falling on the cell, thereby lowering short-circuit current and consequently the system efficiency.

4.3.2 Illumination uniformity

Irradiance distribution at the exit aperture is also a key factor influencing the overall efficiency of the CPV system. MJSCs can suffer a non-negligible loss in efficiency due to nonuniform illumination [73]. Irradiance uniformity is determined in terms of the variation in peak-to-average (PAR) irradiance value as defined in Chapter 3. Analysis of irradiance uniformity is essential to optimally select an MJSC design suitable for a particular CPV optical system.

4.3.3 Acceptance angle

Acceptance angle is defined as the incident angle at which the system efficiency reduces to 90% of the maximum value [84]. It determines system tolerance to tracking errors, pointing to the need to use accurate tracking means, which in turn will influence the overall system cost. The design of the optical system puts a limit on the maximum acceptance angle attainable for a particular concentration. The concentration-acceptance angle product (CAP) stays constant for a specific design and puts a limit on the reduction in system costs achievable by deploying CPV systems. This implies that with increase in concentration the acceptance angle is compromised in order to keep the CAP constant. With the industry moving towards very high-concentration systems, the acceptance angle becomes an important metric for comparison of various CPV optical designs. Often, acceptance angle is quoted as a "half-angle" to include both directions. In this thesis, acceptance half-angle is denoted as α. The acceptance angle would therefore be twice this half-angle.

4.4 Design of concentrating optics

Understanding the design requirements for a CPV system is necessary and challenging due to the complex and varied nature of its components. To support these endeavors and to cut-down costs, modeling and simulation are indispensable tools, used by both academia and industry to predict the performance of such systems. Due to the diversity in the design, parameters and methods of optimization vary significantly across different designs. Lens-based optical systems have been popular among CPV companies worldwide [86] and therefore are a focus of this thesis. Systems using lens based primaries may or may not use a secondary optic for concentration. In the following sections, the three concentrator types, studied in this thesis, are described.

4.4.1 Classical concentrator : The Fresnel lens

Classical lenses use the optical property of refraction to bend incoming light. A refractive Fresnel lens is a classical optical element that is assumed to have been created from a plano-convex lens by removing the material that does not contribute to the bending of light to a common focal point. This reduction in material decreases the volume and weight of the lens. The small volume, light-weight, and low cost of refractive, plastic Fresnel lenses have made them the best choice for utilization in solar concentration applications [87]. Due to the simplicity of design, this single stage concentrator is still used by many companies. Soitec, using the technology developed by Concentrix, was employing this approach in its 500X CPV systems [24].

A Fresnel lens essentially consists of a chain of prisms that can focus light at a point

using refraction. As the focal length f is usually much greater than the thickness d of the lens, the Fresnel lens is approximated as a *thin lens*. The design of prisms in a Fresnel lens plays an important role in determining the performance of the lens. It is typically assumed that the size of the prism is much smaller than the absorber [88]. Fresnel lens parameters can also be specified in terms of an *f-number* or the focal length. The ratio of the focal length of the lens to its diameter is termed as the *f-number* of a lens. In solar concentrators, physical distance between the Fresnel lens and the PV cell is more important than the focal length of the lens and is typically referred to as the *working distance*. This working distance is usually optimized to yield the best possible efficiency within a given wavelength range. Optical efficiency variation with changes in working distance is an important metric to be analyzed when designing CPV systems in order to determine manufacturing tolerances.

In this chapter, the design of CPV optics with a Fresnel lens illuminating a bare cell is analyzed.

4.4.2 Nonimaging optics: A secondary optical element

A typical solar-concentrator design employs a Fresnel lens as the primary optical element (POE) often combined with a non-imaging secondary optical element (SOE) [89]. A non-imaging optic, by definition, is not designed to image the light source, but instead is designed for obtaining maximum optical efficiency at the exit aperture. The fundamentals of nonimaging optical design have been described elsewhere [90] and are not included in this thesis. SOEs not only act as homogenizers, improving the irradiance uniformity on the solar cell, but also aid in increasing the acceptance angle of the optics [69].

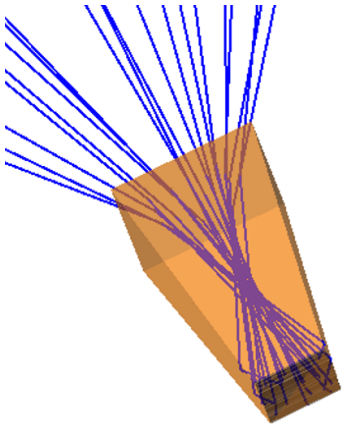

Figure 4.2: *Ray-trace of a truncated pyramid SOE in a two-stage CPV optical system. Rays from the primary fall on the SOE and are totally-internally reflected through the SOE material.*

In this thesis, a nonimaging optic solution using a truncated pyramid secondary, for use with a primary Fresnel lens, is described. Figure 4.2 shows the ray-trace of such an SOE with rays illuminating the SOE and converging on to the exit aperture of the SOE. Such dielectric-filled SOEs use the property of total-internal reflection to focus sunlight on to the solar cell.

Comparative analysis of reflective and refractive secondary optical elements has been performed by Victoria [89] under 1000× concentration. A refractive, truncated pyramid SOE has not been included as part of the study. In order to assess the performance of a concentrator with a truncated pyramid SOE, the Fresnel lens POE is combined with a truncated pyramid SOE in this thesis. Modeling methodology and detailed results are presented in following sections of this chapter.

4.4.3 Advanced concentrator designs

In order to improve the optical design further, advanced concentrator designs such as the Fresnel-Köhler (F-K) have also been adopted. This design, which is a combination of nonimaging and Köhler integration methods, is based on the edge-ray theorem described in detail elsewhere [91]. F-K concentrator is a double-stage system consisting of a square Fresnel lens divided into 4 sectors focusing rays on a Köhler SOE which is again divided into 4 parts. Each sector of the SOE images the corresponding POE sector on to the MJSC as shown in Figure 4.3. A standard version of this optics developed by companies Evonik and LPI, called Ventana [92]. The CPV system used for the F-K design in this thesis is based on the CAD files kindly provided by LPI for the 846× concentration.

4.5 Modeling methodology

There is a plethora of optical design software such as Zemax, Code V, OSLO, LightWave, OpticsLab, etc which can be used for optical design and analysis. Zemax OpticStudio has been chosen as a tool for ray tracing simulations in this thesis. Specifically, Zemax's non-sequential analysis has been used for optical design.

4.5.1 Modeling the emitting source

In order to emulate the Sun, the standard ASTM G173-03 AM1.5D spectrum is the standard for concentrating systems and has been used for these simulations. A solar disc angle of ± 0.267° is used [93]. Ray tracing is performed using the Monte-Carlo method with 1

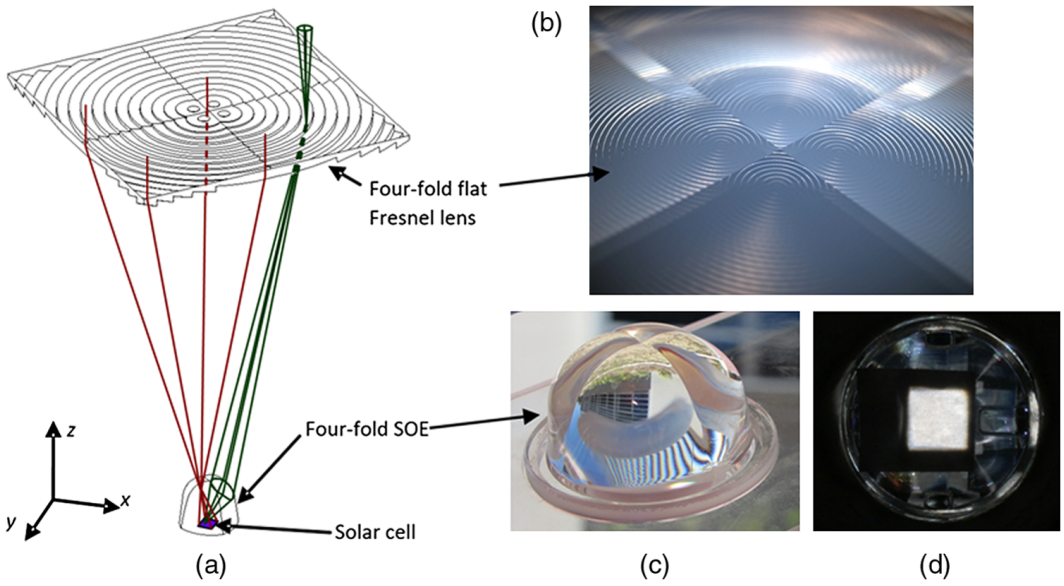

Figure 4.3: *The FK4 is an advanced fourfold Fresnel-Köhler concentrator. (a) The optical system is illustrated together with the edge-rays distribution. (b) Actual manufactured Fresnel lens POE and free-form SOE, both fourfold, are shown. (c and d) Actual CCD image of the cell plane under outdoor sun tracking. It is a white square illumination, indicating the excellent spatial and spectral uniformity provided (Figure and caption reproduced with permission from [24])*

.

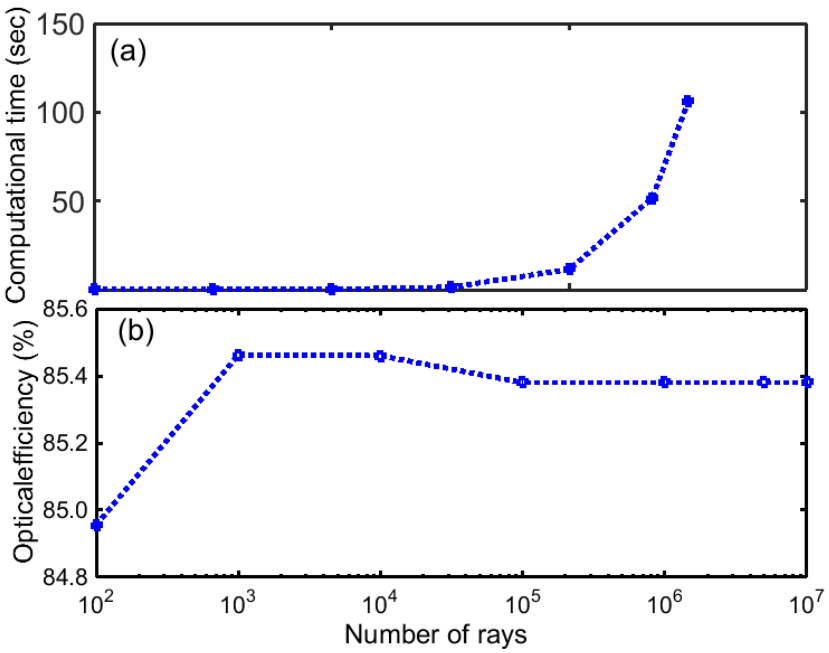

Figure 4.4: *(a) Computational time and (b) optical efficiency as a function of the number of incident rays with Zemax OpticStudio for a two-stage CPV optical system.*

million rays for every optical system. The number of rays traced has a significant bearing on the computational time for each simulation and so the computational time taken and the variation in values is optimized for the simulations. Figure 4.4 (a) shows the computational time as a function of the number of rays for a two-stage CPV optical train. The optical efficiency value as a function of the number of rays is shown in part (b).

It can be seen that while the computational time increases geometrically with an increase in the number of rays traced, optical efficiency does not vary significantly after 10,000 rays. This implies that 1 million rays would suffice considering the accuracy and computational time trade-off.

4.5.2 System components

Optical components arranged systematically from the entrance to the exit aperture of the CPV system is called the optical train. In this thesis, two lens-based optical trains have been modeled:

1. Fresnel lens primary and no secondary

2. Fresnel lens and a truncated pyramid secondary optical element

In addition, results from a case study performed with a commercial 4-fold Fresnel-Köhler design, at 846× concentration, are also presented for comparative analysis. Figure 4.5 shows the 3-D ray trace of three designs obtained at a wavelength of 550 nm and at a concentration of 846 suns. Also, surface scattering effects and Fresnel groove losses are ignored in order to simplify modeling.

4.5.3 Material properties

Material properties influence the absorption and dispersion in the CPV system and are required to be included to get realistic results with ray-tracing. We model the Fresnel lens in polymethylmethacrylate (PMMA) material [94] and the secondary optic in BK7 glass material. Surface scattering effects are neglected in our simulations, thus showing a 'worst' case scenario as scattering effects tend to lower the peaks obtained by the optical system [89].

Figure 4.6 (a) shows the transmission characteristics and Figure 4.6 (b) shows the dispersion characteristics of the PMMA and BK7 materials used for our simulations. Based

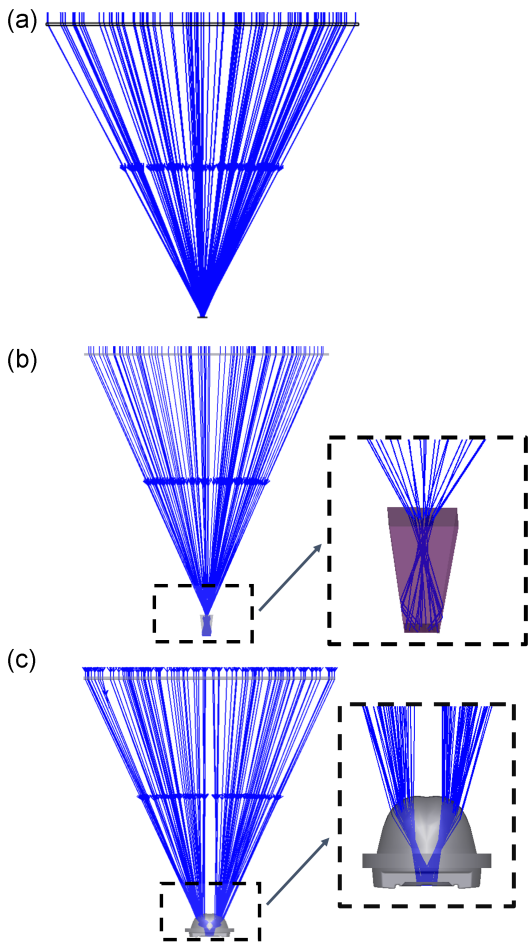

Figure 4.5: *Ray-tracing of CPV systems with (a) a Fresnel lens focusing light on a bare solar cell (b) Fresnel lens POE and a truncated pyramid SOE, and (c) a four-fold Fresnel Köhler design. A magnified view of the rays through the SOEs in both (b) and (c) is presented. While the truncated pyramid uses total-internal reflection to focus the incident rays, the Köhler SOE works on the principle of refraction through a denser medium.*

on the material properties it can be seen that the response of the optical system would be wavelength dependent. The absorption properties of the material causes troughs in the transmission characteristics, specifically in the case of the PMMA material. The change of refractive index with wavelength could result in wavelength-dependent focal point varia-

tions with the Fresnel lens. Since the BK7 material also shows a non-negligible amount of dispersion, the behavior of the rays inside the SOE could vary depending on wavelength. It is important to analyze material properties to make a coarse prediction of optical system's performance over the wavelength range.

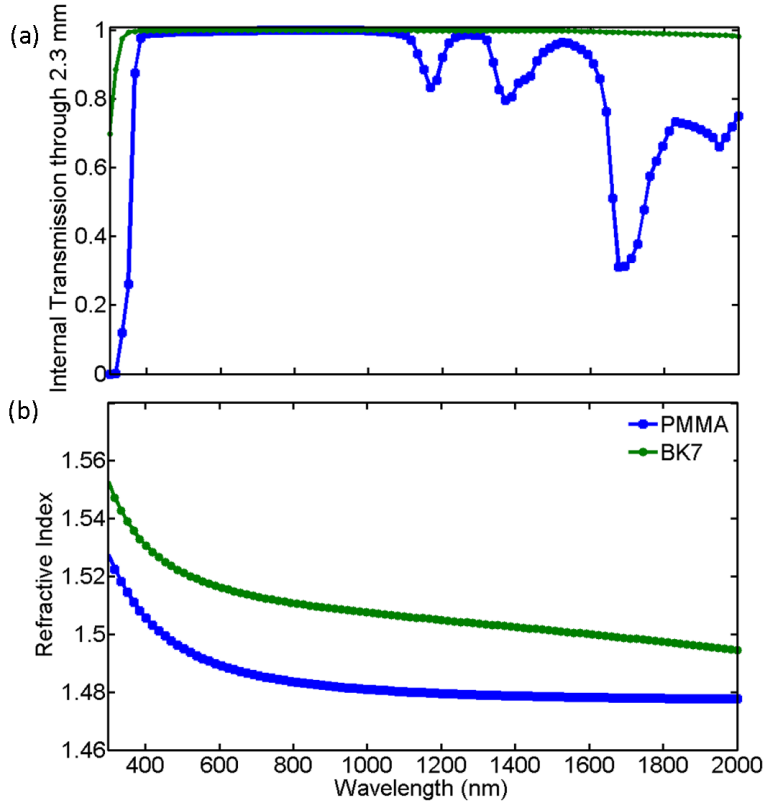

Figure 4.6: *(a) Internal transmission and (b) dispersion characteristics of the PMMA and BK7 material used in optical modeling. These properties need to be entered in the optical design software in order to obtain realistic results.*

4.6 Simulation results

4.6.1 Optical system parameters

In order to maximize the efficiency of the optical system, multiparameter, multifunction optimization needs to be performed. An ideal system would have high optical efficiency, high acceptance angle and lower nonuniformity.

For the two-stage system with a POE and an SOE, fixing the POE parameters, the variable parameters are: the POE-SOE working distance, SOE entrance aperture and the SOE height. Figure 4.7 illustrates these parameters.

For the single-stage, Fresnel lens based system with no SOE, the working distance is chosen to be the only variable parameter.

4.6.2 Optical ray-tracing

First the response of the optical system itself is considered to gain insight into the nominal sensitivity of the illumination profile to variation in critical system dimensions. This allows for a more careful assessment of the range of parameter space over which the full system efficiencies are to be calculated, so that actual system sensitivities to parameter variation can be assessed in the neighborhood of the maximum system efficiency. Ray tracing here can serve as a visual optimization tool to determine a range to narrow on an optimal value. Ray-tracing results for a monochrome source are presented first followed by a more detailed assessment over the entire wavelength range.

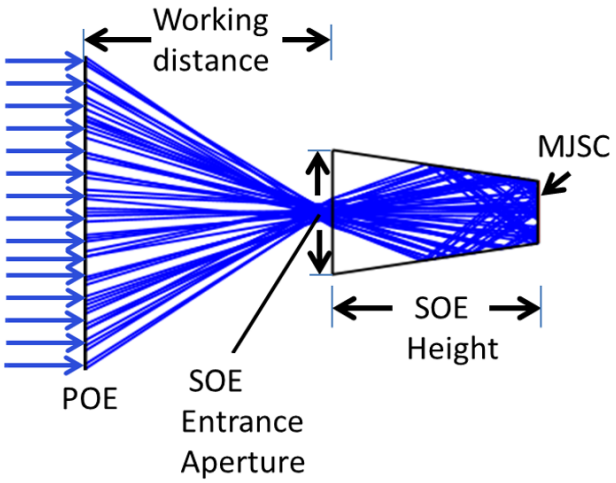

Figure 4.7: *Optimization parameters defined for the 2-stage optical system. Sunlight (from the left hand side) falls on the Fresnel POE and the rays are then incident on to the SOE entrance aperture with the focal point varying as function of the wavelength. The incident rays undergo total internal reflection, reflecting off the walls of the SOE, finally reaching the MJSC at the exit aperture of the SOE via a lossless interface. Losses arising due to the height of the grid contacts are ignored in our simulation.*

The primary-to-secondary working distance determines if the lens focal point for a given wavelength is positioned inside or outside the SOE. It influences the number of total internal reflections in the SOE. Figure 4.8(a) shows the position of the focal point at a wavelength of 550 nm for POE-SOE working distances of (i) 250 mm and (ii) 260 mm using a fixed SOE height of 33 mm and an SOE entrance aperture of 20 mm for a 1250× system. The two distances, 250 and 260 mm, are chosen in order to demonstrate the effect of the focal point being inside the SOE and outside the SOE and how that would affect ray paths. A monochrome design is chosen initially for simplification and the 550 nm wavelength is

chosen for demonstration, since this wavelength lies within the top cell absorption range, which in typical MJSC designs, is the current limiting subcell. A loss in optical efficiency at this wavelength will imply a reduction in the number of photons reaching the top subcell, thereby limiting the overall system efficiency. A more detailed optical transfer function based analysis encompassing the entire wavelength range is performed in the next section to demonstrate the effects of parametric variations. Ray color change is used to visualize the number of internal reflections in a path. For the shorter working distance of 250 mm, the focal point lies inside the SOE and less internal reflections are found. For the longer distance, the focal point lies outside the SOE and the rays diverge before hitting the SOE, and homogeneity is improved, but at the cost of a 16% loss in optical efficiency due to the escaping rays. For the 260 mm distance, the rays are no longer confined to the SOE and the total internal reflection condition is not satisfied. The focal point of the Fresnel lens varies as a function of wavelength due to the dispersion in the PMMA, implying that the optimal working distance will be wavelength dependent. In the case of longer wavelengths, the focal length increases and the loss in optical efficiency may not occur at 260 mm but instead at working distances >260 mm. By increasing the height of the SOE (from 25 to 35 mm) for fixed working distance, we increase the number of total internal reflections in the SOE. An increase in total internal reflection implies an increase in spatial uniformity. Figure 4.8(b) shows ray-traces at a wavelength of 550 nm for two different SOE heights, (i) 25 and (ii) 35 mm, for a fixed working distance of 250 mm and an entrance aperture of 20 mm. At an SOE height of 25 mm, the peak-to-average irradiance ratio (PAR) is approximately 1.3; for the longer SOE (35 mm), the increased distribution of red and blue rays striking the MJSC indicates an increase in the number of multiple reflections, resulting in an improved

homogeneity and a PAR = 1.1. The difference in optical efficiencies is negligible (0.1%). Increasing the width of the SOE entrance aperture increases the angle at which rays strike the SOE wall, leading to a loss of confinement when total internal reflection is no longer typically satisfied; this reduces the optical efficiency. This is illustrated in Figure 4.8 (c) by comparison of ray traces at 550 nm for entrance apertures of (i) 16 and (ii) 40 mm, at a fixed working distance of 250 mm and a height of 33 mm. All the rays are contained within the SOE for the narrower width, but for the wider width, there is a marked failure to satisfy total internal reflection leading to a 50% reduction in optical efficiency. Optimal aperture widths vary based on concentration and optical design. Various types of SOE and corresponding aperture widths have been specified in [89] with SOE entrance to exit aperture width ratios varying from 1.5 to 2.5.

The working distance was changed to 260 mm to demonstrate that any working distance other than the optimal can have a significant effect on the optical efficiency. A similar study was done to demonstrate that the change in SOE height and entrance aperture has a similar effect. The main objective of this demonstration was to show that these three parameters can significantly affect system efficiencies.

4.6.3 Optical transfer function

In order to determine the optical transfer function, the wavelength range needs to be determined. Since the response of the MJSCs, described in Chapter 2, is restricted between the 360 - 2000 nm range and the transmission of the PMMA and BK7 materials cuts-off below 360 nm, a 360 - 2000 nm range is chosen for all optical simulations in this thesis.

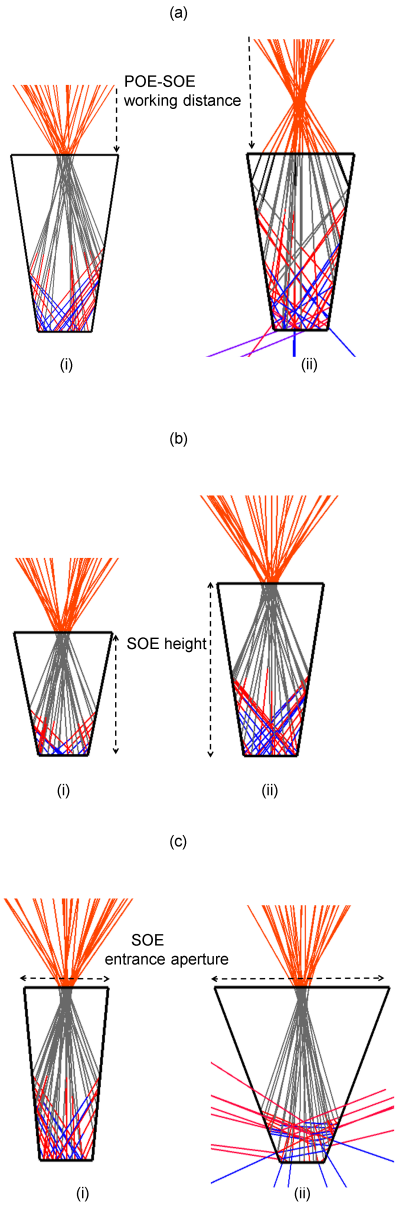

Figure 4.8: *Ray traces displaying the variation in the location of Fresnel lens focal point and the total internal reflection as a result of a change in (a) POE-SOE working distance (b) SOE height, and (c) the SOE entrance aperture width at a wavelength of 550 nm for the 1250× system.*

In order to illustrate the effects of the varying the optimization parameters, the 1250× design is chosen, primarily because it may be more sensitive to these variations. Figure 4.9 shows the optical transfer function for the 1250× system at different working distances, SOE heights and SOE entrance aperture widths.

Figure 4.9 (a) shows the dependence of the optical transfer function on wavelength for four different values of the POE-SOE working distance. The OTF, expressed as an optical efficiency, is determined for 161 wavelengths within a range from 360 to 2000 nm. The entrance aperture and the height of the SOE are fixed at 16 and 35 mm, respectively. At short wavelengths, the OTF rises more rapidly as the working distance decreases, with optical efficiencies plateauing at wavelengths > 500 nm. Little change in the OTF is seen over the rest of the spectrum, except at the shortest of working distances, where from about 1200 nm to 2000 nm a decrease of about 20% is noted. This is mainly due to the escaping rays and a failure to satisfy total internal reflection within the SOE at longer wavelengths. Consequently, the top subcell should be the most sensitive to variations in the working distance. Figure 4.9(b) shows the dependence of the OTF on wavelength for four different values of the SOE height. The OTF is determined for a primary-to-secondary working distance of 250 mm and an entrance aperture width of 16 mm. Little change in optical efficiency is seen over most of the spectrum except around 400 nm for the shortest height (as shown in the inset). For SOE heights ranging from 20 to 40 mm, a small reduction in the OTF is seen at wavelengths above 1540 nm. One anticipates negligible impact on system efficiency for the three-junction designs since the 3JLM has an overproducing bottom subcell and the 3JIMM is spectrally unresponsive to wavelengths above 1400 nm. A modest

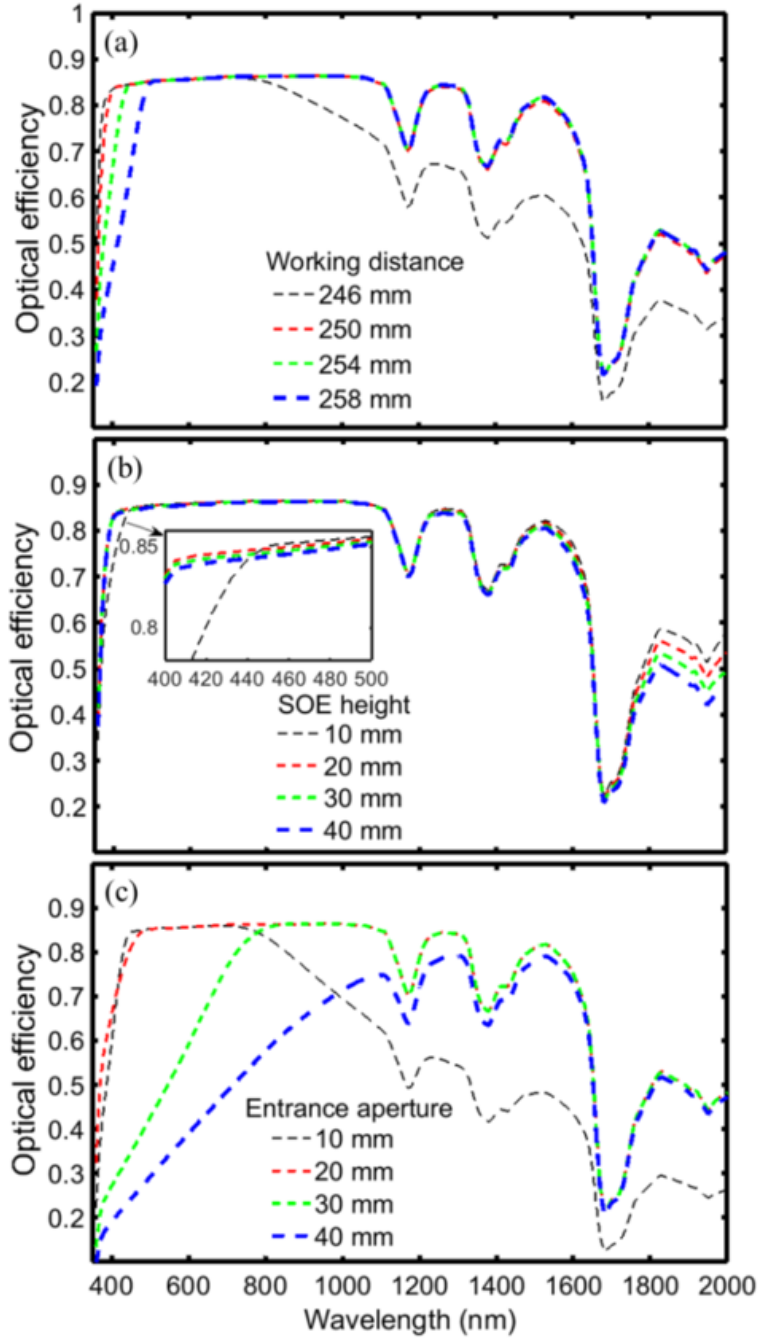

Figure 4.9: *Optical efficiency as a function of wavelength for the 1250× system at different (a) POE-SOE distances (b) SOE heights, inset shows the variation in the optical transfer function between 400 and 500 nm , and (c) SOE entrance aperture widths*

impact, however, can be expected for the 4JLM design due to its broad absorption range and its current-matched bottom subcell. An optical efficiency reduction in the bottom subcell range of absorbed wavelengths would imply a current-limiting bottom subcell and a decrease in system efficiency. Figure 4.9 shows the dependence of the OTF on wavelength for four different values of the SOE entrance aperture width. The OTF is determined for a primary-to-secondary working distance of 250 mm and an SOE height of 35 mm. A very strong dependence on aperture width is seen across all wavelengths, increasingly so for larger apertures, and especially towards wavelengths < 770 nm. This arises from a loss in total internal reflection. There will, therefore, be a marked impact on system efficiencies for all designs with any significant departure from the optimal SOE width.

4.6.4 System optimization for truncated pyramid based designs

Although the OTF provides valuable information about the system's performance over a range of wavelengths, the calculation of the OTF and the corresponding short-circuit current for each value in the parameter space adds to the computational time for each simulation. In order to simplify the optimization process, instead of using the OTF, the optical efficiency is chosen as an initial metric. Setting the source spectrum to the reference AM1.5D spectrum, the optical efficiency is calculated by taking a ratio of the total power incident on the solar cell to the total power incident on the entrance aperture i.e. the Fresnel lens. In addition to the optical efficiency, the acceptance half-angle and the peak-to-average irradiance ratios also need to be evaluated over the parameter space.

In this section, the three figures of merit are evaluated for the optical designs at the

two concentrations.

Figure 4.10 shows the multiparameter optimization results as scatter plots with (a) optical efficiency, (b) the acceptance half-angle and (c) the PAR value for the 846× system.

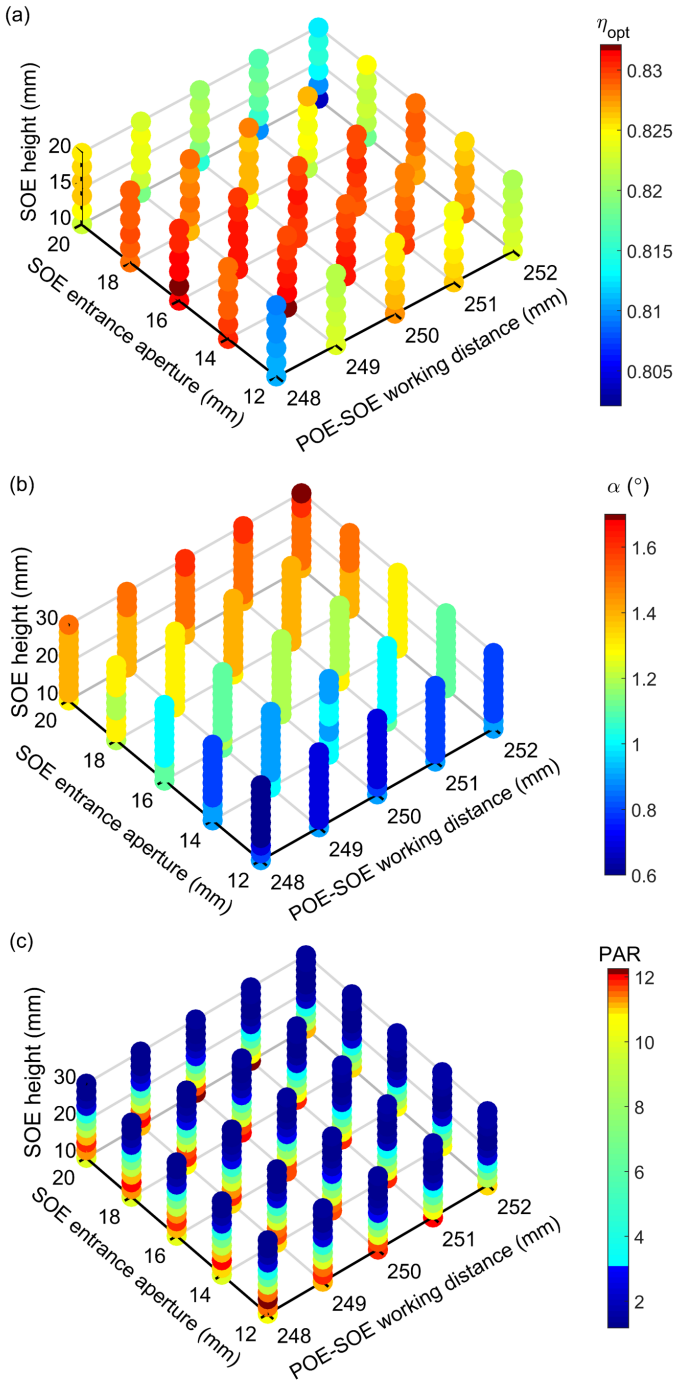

Figure 4.10: *(a) Optical efficiency (b) Peak-to-average irradiance ratio (c) Acceptance half-angle for a 846× system over a range of parameter values.*

Figure 4.11 shows the multiparameter optimization results as scatter plots with (a) optical efficiency, (b) the acceptance half-angle and (c) the PAR value for the 1250× system.

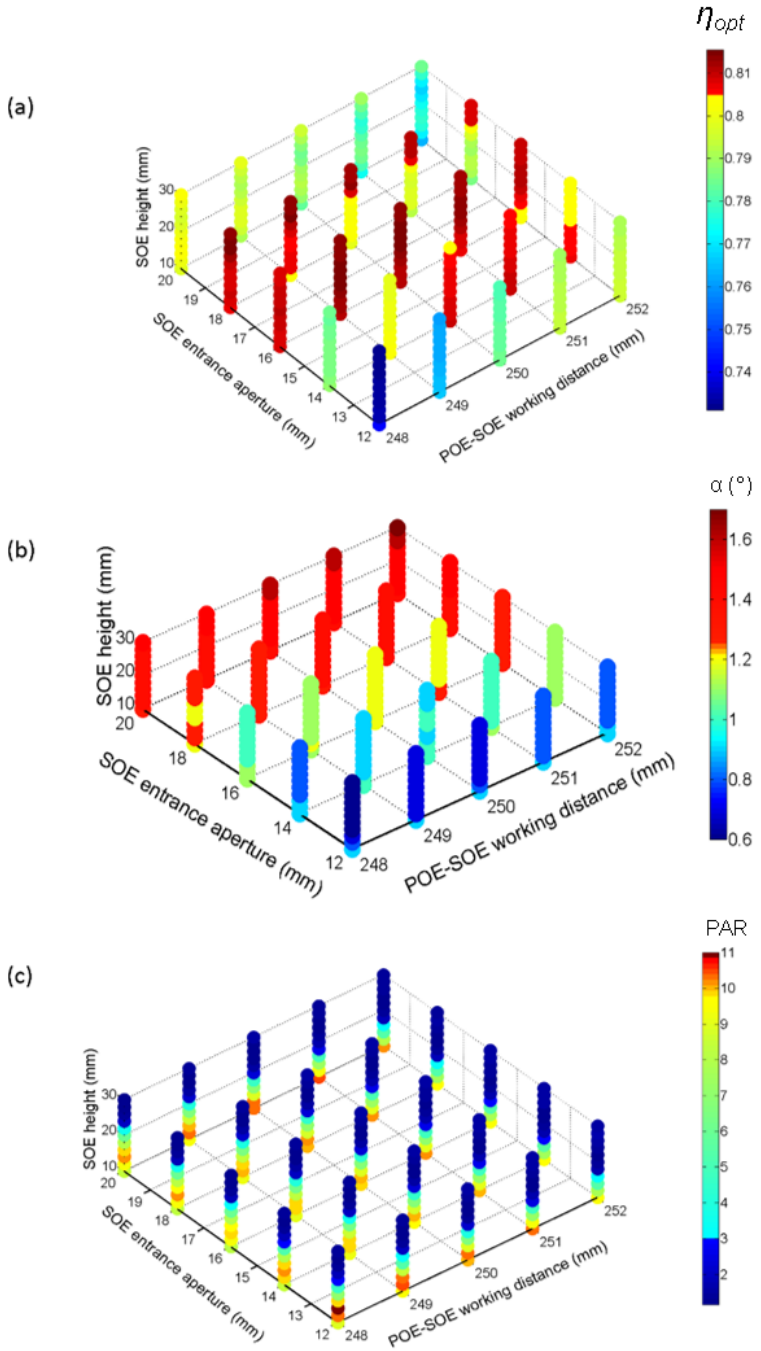

Figure 4.11: *(a) Optical efficiency (b) Peak-to-average irradiance ratio (c) Acceptance half-angle for a 1250× system over a range of parameter values.*

Both Figure 4.10 and Figure 4.11 indicate that a trade-off has to be made between optical efficiency, acceptance angle and PAR values. If the design point with maximum optical efficiency is chosen, the acceptance angle is reduced and the PAR value is high, which is undesirable. It can be seen that higher optical efficiencies are obtained with lower SOE heights. However, lower SOE heights cause an increase in PAR. This may have a different impact, depending on the MJSC design. Therefore, the design point has to be chosen keeping in mind the three figures of merit as they correspond to the individual MJSC design. In addition, higher SOE heights would imply a higher cost. This is an added factor to be kept in mind while designing for manufacturing.

For this analysis, to optimize the optical parameters without the knowledge of the individual MJSC design, the optimization methodology chosen is as follows. Simulation results within the parameter ranges are first sorted by parameter values which yield maximum optical efficiency, followed by the values yielding maximum acceptance half-angle. Data is further filtered for PAR values $<$ 2, since all the three designs in Chapter 2 show less reduction in efficiencies at this PAR. Such a scheme has been adopted to maximize the photons falling on the cell at angles $\leq$1, which is almost 5 times the solar angle. This implies that the allowable errors for the tracker system are upto 1°. In addition, the values are chosen to minimize the SOE heights to lower manufacturing costs.

Based on this criterion, the working distance for the 846× design is 251 mm while for the 1250× system is 250 mm. While the SOE entrance apertures are 16 mm for both the designs, the SOE heights are 22 mm and 20 mm for the 846× and the 1250× design respectively.

At these design points, the figures of merit values obtained are presented in Table 4.1.

Table 4.1: *Figure of merit value obtained at the design point.*

***X* (suns)**	η_{opt} (%)	α (°)	PAR
846	82.9	1.2	1.5
1250	81.6	1.0	1.5

Optical efficiency is most sensitive to variations in the working distance followed by the SOE height both the concentrations. Optical efficiencies of >80% can be obtained at both concentrations with acceptance half-angles $\geq 1°$. It can be seen that the acceptance angle decreases with concentration, as expected. In order to assess the response over wavelength, the OTF at each design point is calculated. Figure 4.12 shows the OTF and the PARs at design point for both the concentrations. This allows for a more thorough understanding of the behavior and performance of the optical system.

Based on these results, it can be seen that in order to achieve higher acceptance angles, optical efficiency needs to be compromised. The OTF clearly indicates the absorption bands of the PMMA material. The loss penalty in the OTF can be attributed to 4% loss at each interface. For the design with the SOE, this amounts to 12% due to Fresnel reflections. Losses in the material (both PMMA and BK7) further increase the loss penalty.

4.6.5 System optimization for a single stage design

The single-stage Fresnel lens-based design has been optimized for both 846 and 1250 suns. For a system without an SOE, the only optimization parameter is the POE-Cell distance.

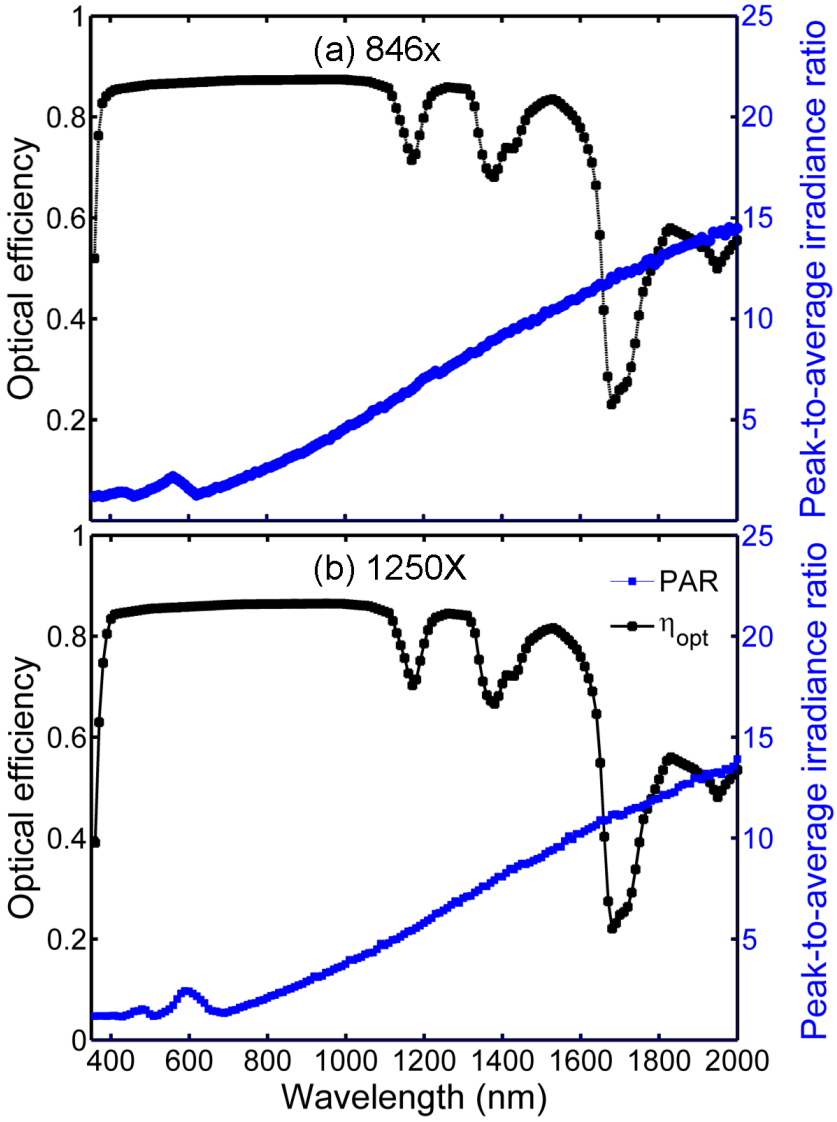

Figure 4.12: *Optical transfer function and the peak-to-average irradiance ratio as a function of wavelength for (a) the 846× system and (b) the 1250× system.*

Fresnel lens parameters are kept the same as the one with the SOE. Figure 4.13 shows the optical efficiency and acceptance angle and PAR values the 846× and the 1250× system, over a range of POE-Cell distances. Again, the optical efficiency is calculated under the reference spectrum for both the concentrations.

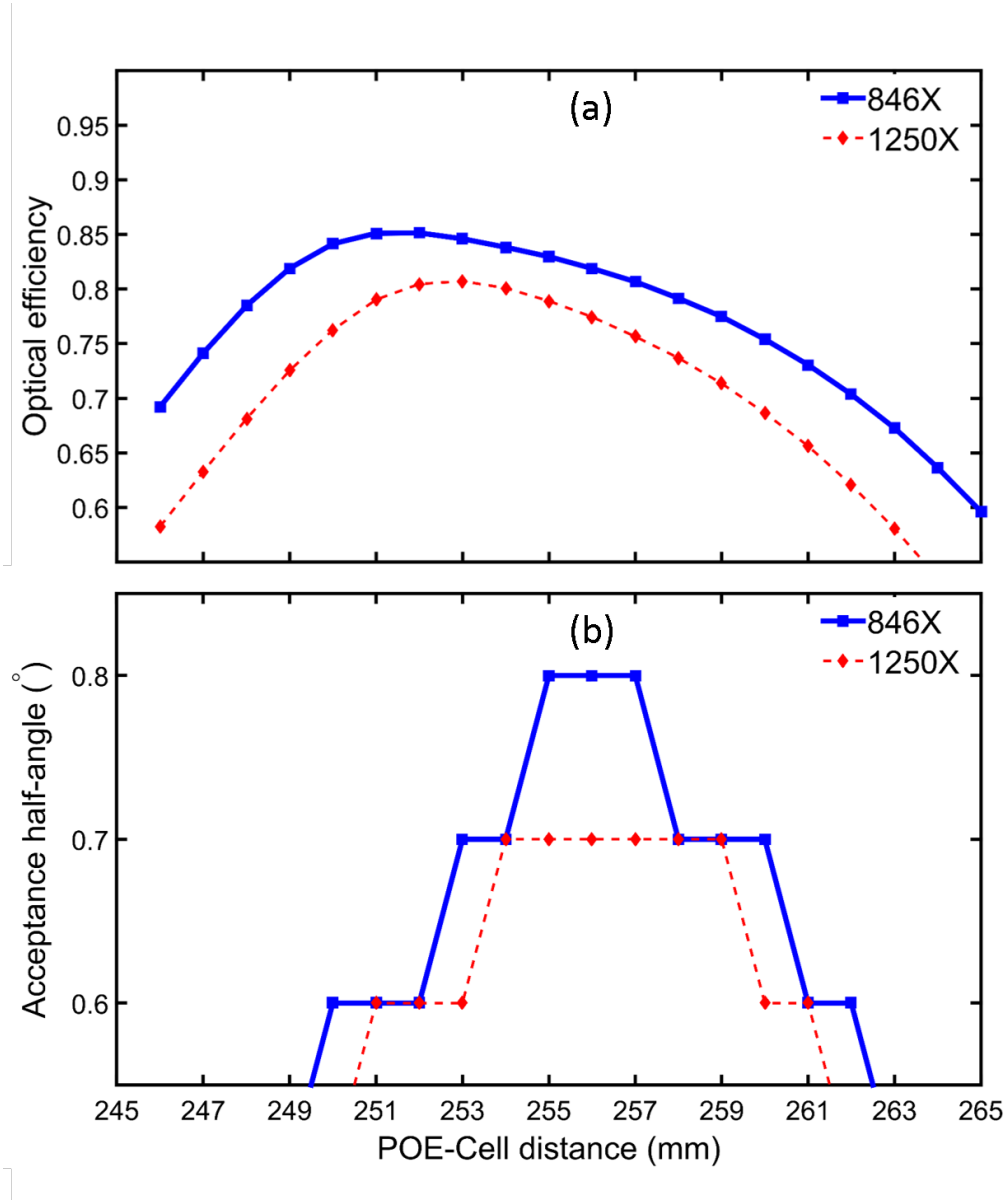

Figure 4.13: *(a) Optical efficiency and (b) acceptance angle as a function of POE-cell distance for the 846× and the 1250× systems .*

For the 846× system, The maximum attainable angle of acceptance is now 0.8°, almost half of the maximum angle with the truncated pyramid SOE. The optical efficiency is however increased to $> 85\%$ under the AM1.5D spectrum. This is because the additional 4% Fresnel reflection losses due to the front surface of the SOE are now avoided. Even though the optical efficiency has improved, the PAR values suffer drastically with the maximum PAR value of 16 obtained at a working distance of 258 mm. If the design point is chosen to be at maximum optical efficiency (working distance = 252 mm), the acceptance angle would be 0.6° and the PAR would be 7.7. Similarly, for the 1250× system, the POE-cell distance at the maximum optical efficiency (80.7%) was determined to be 253 mm. It should be noted that the optical efficiency in this case was reduced from the case with the SOE (81.6%). This is because at such high concentrations, there is a loss of rays even at the optimal distance.

In order to analyze this further, the OTF and the PAR values at the optimal distance is determined as shown in Figure 4.14. At the optimal distance, for the 846× while the optical transfer function may be improved, the PAR significantly increases for the lower wavelengths, implying higher losses for the top subcell in a MJSC. For the 1250× concentration, the optical efficiency characteristics are lower than the 846× design. The PAR values show a very similar trend, with higher PARs for wavelengths between 500 to 750 nm. This can have a significant effect on the performance of an MJSC due to current mismatch between the subcells. The impact might be more pronounced for cells with greater number of junctions, as the wavelength sensitivity will be greater for such designs.

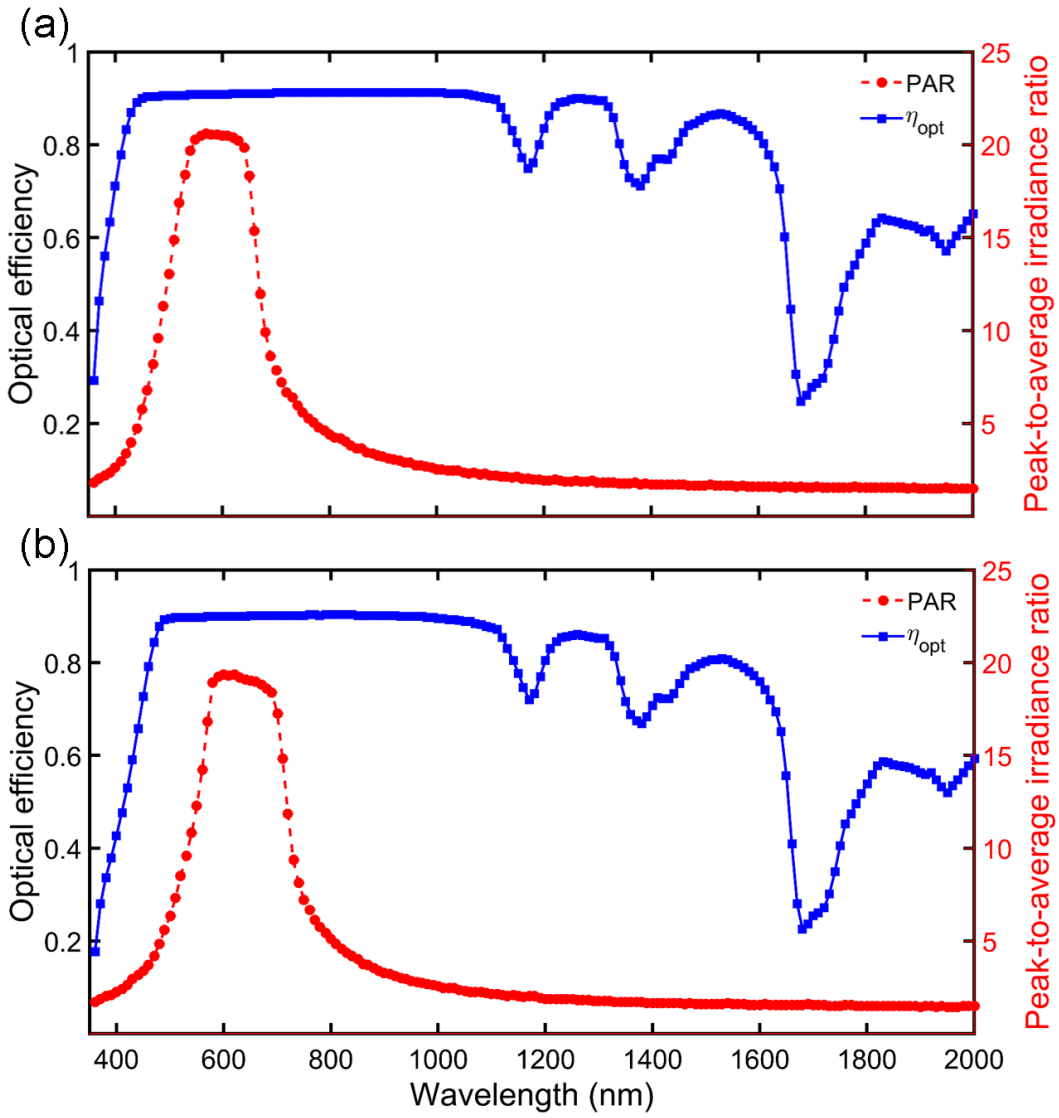

Figure 4.14: *Optical transfer function as a function of wavelength for the (a) 846× and (b) 1250× system without the secondary.*

4.7 Case study: Fresnel Köhler CPV system

The F-K system modeled here is based on the Ventana design by LPI [92]. The CAD files for the POE and the SOE were provided by LPI and were used unchanged for the simulations in this section. In order to compare the performance of this design with the Fresnel-Truncated pyramid design, the same PMMA material is used for the 4-quadrant Fresnel lens as the truncated pyramid counterpart. The SOE is made up of BK7 glass. Typically index-matched silicone material is used as an adhesive for attaching the cell with the secondary [95]. The properties of the silicone material used in this case study have been included in the Appendix. Figure 4.15 shows the OTF of the Fresnel and truncated pyramid (F-TP) design and the F-K design at the design point. Comparison shows that the optical efficiency of the F-K system (with the silicone adhesive) is <3% than the F-TP design until 1130 nm and the difference increases more towards the higher wavelengths. If the silicone material properties are changed to a material similar to BK7, there is an improvement in optical efficiency at these wavelengths. While groove losses are ignored in Zemax for the F-TP design, these losses are included in the F-K design, which could be the cause of the reduced optical efficiency.

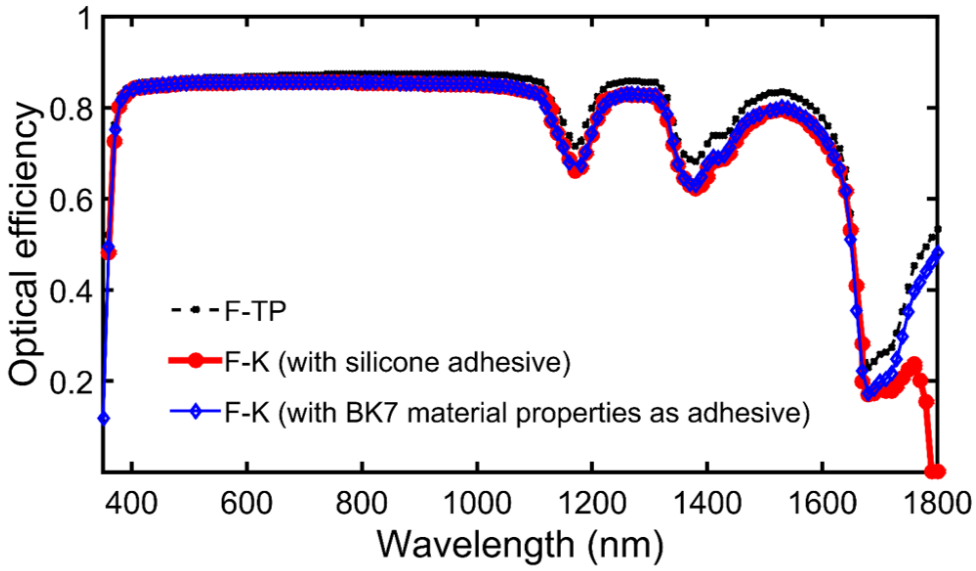

Figure 4.15: *Optical transfer function as a function of wavelength for the Fresnel lens with truncated pyramid (F-TP) and the Fresnel Köhler (F-K) design at 846× concentration.*

At the design point the acceptance half-angle was 0.8° for the F-K design and 1.2° for the F-TP design. The acceptance half-angle for the F-K design is lower than expected based on the calculations in [96], implying the need for improvement. Figure 4.16 shows the normalized irradiance profile (pixel area of 40 x 40) of (a) the F-TP design and (b) the F-K design at the design point. While the F-TP design shows a more Gaussian-like distribution, the F-K design shows a rectangular window-like, even distribution on the cell. There is a sharper cut-off with the F-K design as indicated by the surface plot.

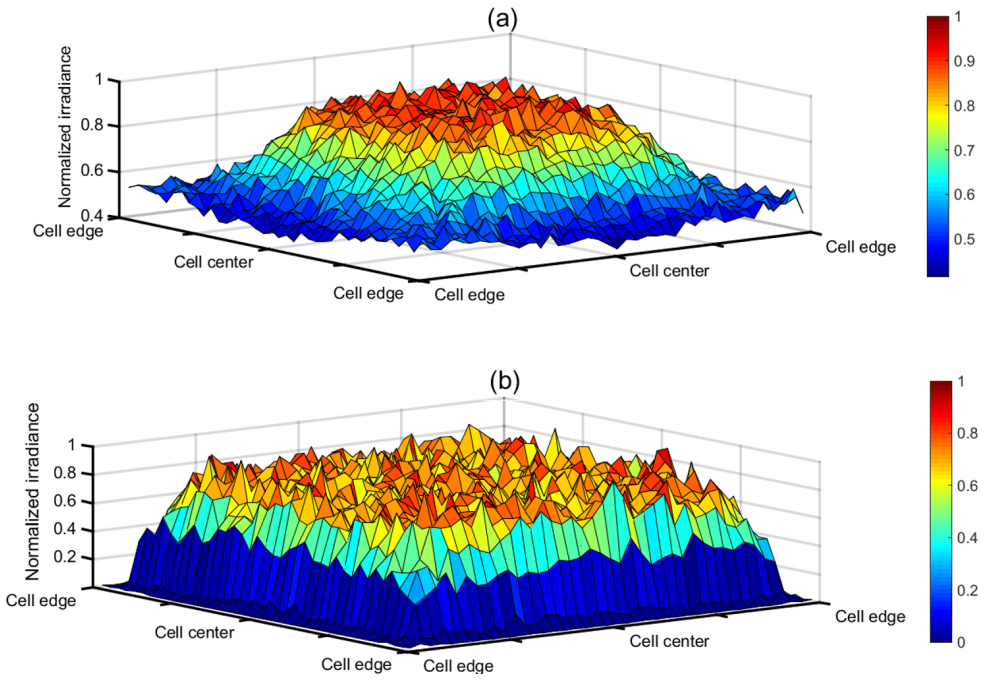

Figure 4.16: *Normalized irradiance on the solar cell for (a) the Fresnel-truncated pyramid design and (b) the Fresnel Köhler (F-K) design under the AM1.5D spectrum.*

In order to determine the tolerance to POE-SOE working distance, the optical efficiency for both the designs is evaluated over a 30 mm range. Figure 4.17 shows the normalized optical efficiency as a function of the POE-SOE working distance for the two designs. The results indicate that the F-K design is significantly less sensitive to changes in working distance, with less than 1% drop in efficiency over a 17 mm range. This implies that the F-K design is more tolerant to manufacturing errors due to working distance.

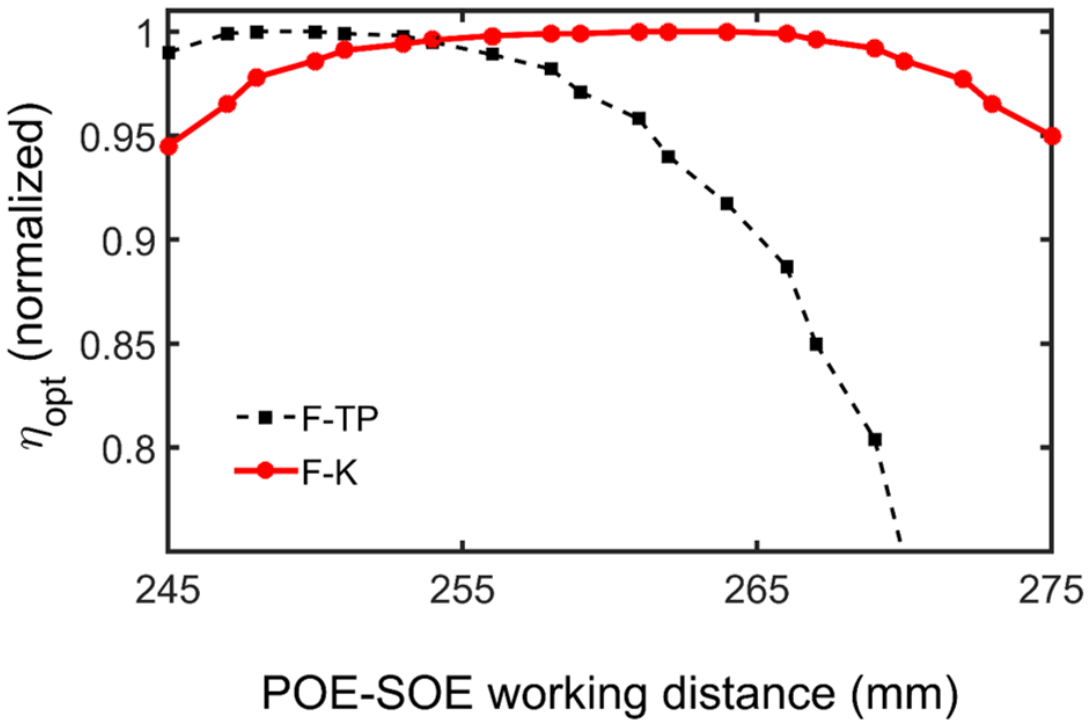

Figure 4.17: *Normalized optical efficiency as a function of the POE-SOE working distance for the truncated pyramid (F-TP) and the Fresnel Köhler (F-K) design under the AM1.5D spectrum.*

In conclusion, the results indicate that while the F-TP design demonstrates a marginally higher optical efficiency and a larger acceptance angle, the F-K design presented above is superior in terms of illumination uniformity and tolerance to working distance changes. Improvements in the design could be made to obtain better acceptance angles theoretically possible with the F-K design.

4.8 Mitigating losses due to dispersion

Since the solar spectrum is composed of several different wavelengths, refractive Fresnel lenses are *ideally* required to provide high-efficiency for the entire wavelength range. However, this is practically unattainable primarily due to absorption and dispersion in the material. Dispersion in the Fresnel lens implies that the refractive index of the Fresnel lens material varies as a function of the wavelength and therefore light is bent by different amounts depending on wavelength. Fresnel lenses are typically designed and optimized to work at a specific design wavelength and when these lenses are used at a wavelength other than the design wavelength, the location of focal spot changes and the solar cell is irradiated by varying distributions depending on the wavelength. In order to mitigate losses due to dispersion, the use of diffractive lenses is proposed. The following subsections focus on the theory and design of an achromat using diffractive lenses.

(a) Diffractive lenses

A diffractive lens can be viewed as a wavelength converter instead of a ray-bender unlike the refractive lens. A diffractive lens also focuses light to a point but by imposing a phase-shift on the incident wave. A Fresnel phase plate can be used as the closest approximation to a thin diffractive lens and is composed of radial, concentric Fresnel zones [97]. If the individual Fresnel zones are designed appropriately, each zone will focus light to a common point. Figure 4.18 depicts the Fresnel zones in a diffractive lens focusing at a common focal point.

If λ_0 is the design wavelength and f_0 is the desired focal length, then the radius of each

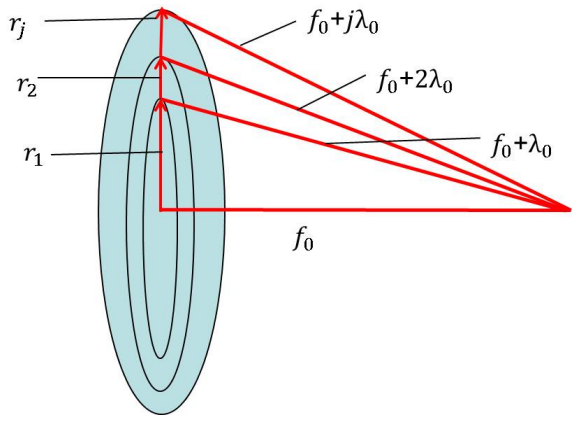

Figure 4.18: *Fresnel zones in a simple diffractive lens. Image reproduced from [97].*

zone can be determined by using Pythagorean theorem as follows.

$$r_j^2 = 2j\lambda_0 f_0 + (j\lambda_0)^2 \tag{4.5}$$

In the paraxial region, $(j\lambda/4f_0 << 1)$, hence equation (4.5) reduces to

$$r_j^2 = (2j\lambda_0 f_0) \tag{4.6}$$

In paraxial approximation, the radii of the jth zone is given by

$$r_j = \sqrt{(2j\lambda_0 f_0)} \tag{4.7}$$

So, in order to create a diffractive lens focusing at f_0 at the design wavelength, a surface-relief structure needs to be created which changes the phase by 2π at the radii. A 2π phase change translates to one wavelength of optical path difference (OPD).

Distance between Fresnel zones can be determined by taking the difference between the radius of the j^{th} zone and the radius of the $(j+1)^{th}$ zone [97].

$$r_j^2 = 2j\lambda_0 f_0 \tag{4.8}$$

$$r_{j+1}^2 = 2(j+1)\lambda_0 f_0 \tag{4.9}$$

$$r_{j+1}^2 - r_j^2 = 2f_0\lambda_0 \tag{4.10}$$

If j is very large, then $r_{j+1} + r_j$ is approximately equal to $2r_j$ and $\Delta r = r_{j+1} - r_j$. So,

$$2r_j \Delta r = 2f_0\lambda_0 \tag{4.11}$$

$$\Delta r = f_0\lambda_0/r \tag{4.12}$$

Δr can be then considered to be the local grating period $\Lambda(r)$.

(b) Dispersion in a Diffractive lens

The focal length of a diffractive lens varies linearly as the wavelength. Based on equation (4.12), power of a diffractive lens can be determined as

$$\phi_0 = \lambda_0/r\Lambda r \tag{4.13}$$

The profile of the lens is depicted by the denominator in equation (4.13) and is constant for a particular lens.

To analyze the effect of dispersion, the optical power of a diffractive lens at a wavelength other than the design wavelength is given as

$$\phi(\lambda) = (\lambda/\lambda_0)\phi_0 \tag{4.14}$$

$$\phi_0 = \lambda_0/r\Lambda r; \tag{4.15}$$

At long wavelength λ_l and short wavelength λ_s the optical power would be

$$\phi_l = \lambda_l / r\Lambda r; \phi_s = \lambda_s / r\Lambda r \tag{4.16}$$

So, the amount of chromatic aberration can be calculated as:

$$\Delta\phi = \phi_s - \phi_l = (\lambda_s - \lambda_l)/r\Lambda r; \tag{4.17}$$

Therefore the equivalent Abbe number or *V-number* for this lens would be

$$V = \lambda_0 / \lambda_s - \lambda_l \tag{4.18}$$

For a plastic, PMMA lens, the *V-number* in the visible region can be calculated as

$$V = 587.6/(486.1 - 656.3) = -3.45 \tag{4.19}$$

This clearly demonstrates that a diffractive lens is dispersion negative and can be extremely useful in designing an achromat.

(c) Simulation results

A separate Zemax model at 625× concentration was created for this section to evaluate focal shift.

The focal shift due to chromatic aberration is determined by using "Sequential Analysis" simulation in Zemax. Figure 4.19 shows simulation results for the focal shift as a function of wavelength in this refractive Fresnel lens system. The net chromatic focal shift of this system is about 18 mm at a concentration of 625 suns.

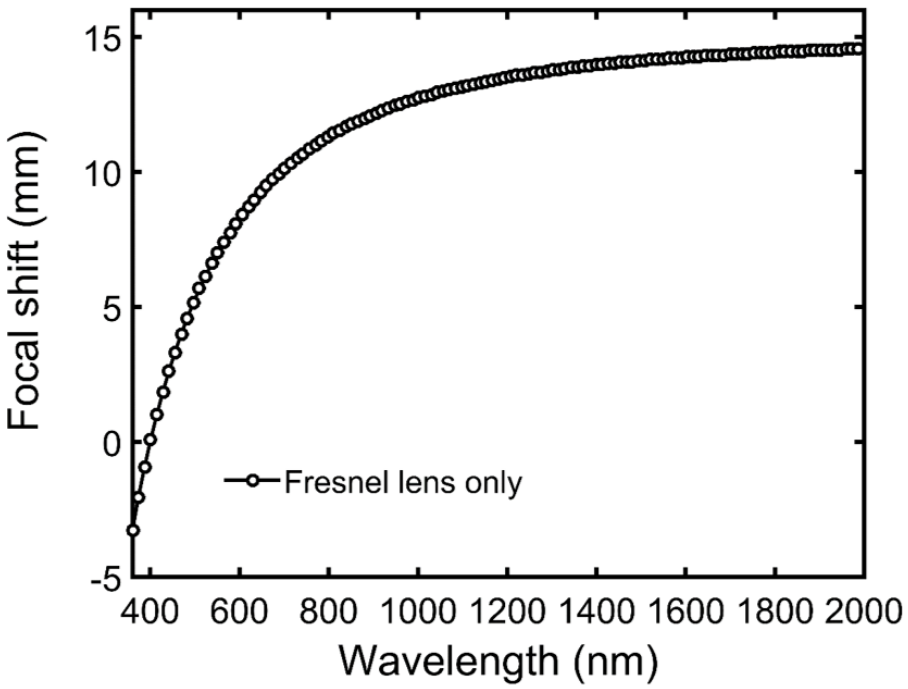

Figure 4.19: *Chromatic focal shift with a refractive Fresnel lens.*

Before an achromat is designed,the *V-number* of a glass material needs to be determined. For visible region, the *V-number* is given as:

$$Vnumber = (n_d - 1)/(n_F - n_C) \tag{4.20}$$

where n_d= refractive index of the material at 589.67 nm (yellow line of helium), n_F= refractive index of the material at 485.1 nm (blue line of hydrogen), n_C= refractive index of the material at 656.3 nm (red line of hydrogen).

The *V-number* of PMMA, used for the refractive Fresnel lens, can be calculated as:

$$Vnumber = (n_d - 1)/(n_F - n_C) = 52.6 \tag{4.21}$$

An achromat consists of two or more lenses combined together such that their total

dispersion is equal to 0 [97], [98]. Considering a two lens design, the basic achromatization condition would be

$$\phi = \phi_a + \phi_b = (n_1 - 1)c_1 + (n_2 - 1)c_2 \tag{4.22}$$

where n_1 and n_2 are the refractive indices at the central wavelength λ_d for the two lenses and c_1 and c_2 are the sum of curvatures of individual lenses.

The optical power of each lens and lens material (which governs the refractive index), is selected such that the net chromatic aberration of the combined lens is 0.

$$\Delta\phi == (n_F - n_C)c_a + (n_F - n_C)c_b = 0 \tag{4.23}$$

Given that $c_a = f_a/(n_a - 1)$ and $c_b = f_b/(n_b - 1)$ [97], substituting in (4.23), the final equation can be simplified to

$$\Delta\phi_a/V_a = -\Delta\phi_b/V_b \tag{4.24}$$

This implies that to achromatize a positive lens, either a lens with *negative optical power* or a *negative V-number* needs to be used.

Since diffractive lenses are dispersion negative and have a negative *V-number*, they can be successfully deployed for achromatization. Using equation (4.24) the parameters of a diffractive lens can be calculated as:

The design parameters for the diffractive lens indicate that the required optical power and the thickness of the lens is very small as compared to the refractive lens counter-

Table 4.2: *Parameters calculated for a Hybrid Lens.*

Parameter	**Value**
Focal length	4500 mm
$F/\#$	18.1
Optical power	0.000220624/mm
Radial height	125 mm
Maximum Thickness	1.1 microns

part. In addition, since the *V-number* of the lens is independent of the material, this lens can be made with the same material as the refractive Fresnel lens making it simpler to manufacture.

The refractive lens and the diffractive lens, combined together, form a "Hybrid" lens which can be visualized as shown in Figure 4.20. A similar design has been proposed in [98] analytically. However, no Zemax models have been presented with the design which depicts a diffractive lens on top and the refractive lens on the bottom. Such a design would have problems in the field as the diffractive lens, which has much smaller grooves, would be difficult to clean if facing the sun. Hence, we propose the diffractive lens to be at the bottom, with grooves facing the solar cell inside the assembly.

Note that the two lenses have been designed with no space between them. This is to avoid any additional surfaces that can incur losses due to Fresnel reflections.

A model of a hybrid lens as designed in Zemax is shown in Figure 4.21.

The appropriate diffractive lens was created using the "Binary" object in Zemax. Once

Figure 4.20: *Hybrid lens with a refractive lens on top and a diffractive lens at the bottom. (Figure not to scale)*

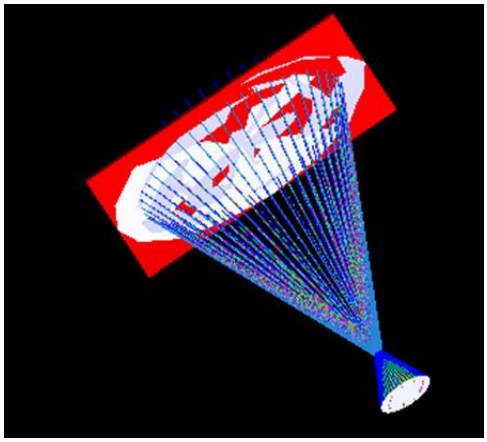

Figure 4.21: *Hybrid lens model as implemented in Zemax.*

the diffractive lens parameters were set as an input to the Zemax model, the design was optimized using Zemax's default merit function. The default merit function is supposed to determine parameters to optimize to a minimum spot size within a wavelength range. The hybrid design was optimized and the chromatic focal shift was determined with this design.

A comparison of results for the chromatic focal shift with a refractive Fresnel lens and a hybrid lens is shown in Figure 4.22.

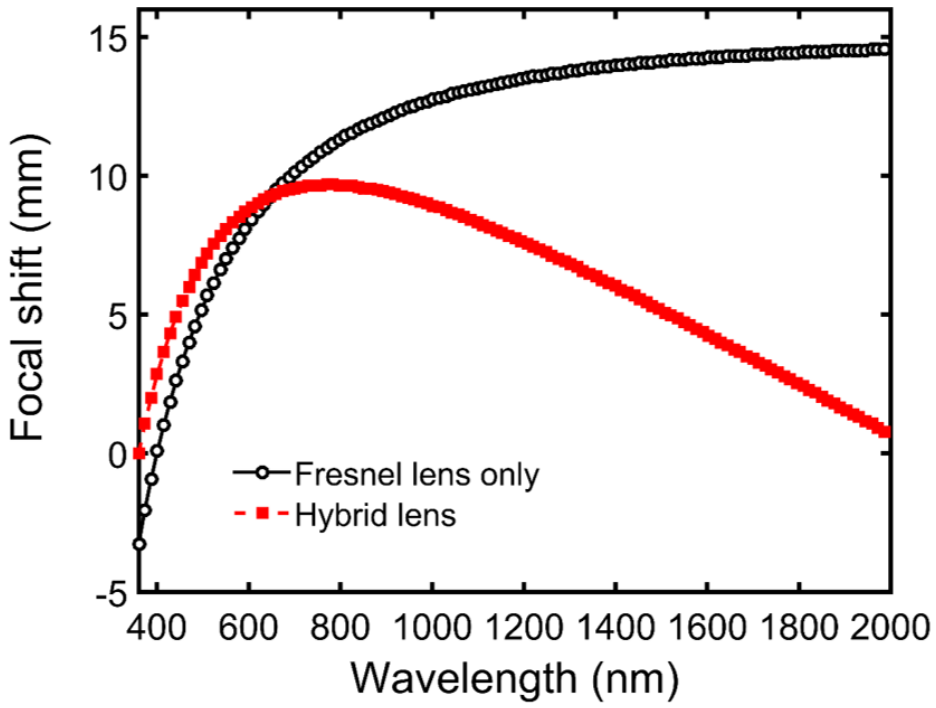

Figure 4.22: *Comparison of focal shift with a* Hybrid *lens and a refractive lens.*

(d) Discussion

Our design clearly demonstrated a reduction in chromatic focal shift when a hybrid lens was used. The chromatic focal shift reduced from a net value of 17 mm to about 9 mm with a hybrid lens in 50 optimization cycles. In order to completely analyze the system, the diffraction efficiency needs to determined. The simplest method of determining the efficiency of a diffractive element is to analyze a blazed grating. A continuous saw-tooth blazed grating diffracts with 100% efficiency in the first diffraction order when the peak-to-peak phase variation is 2π radians [97], [99].

Consider a periodic, linear, blazed grating with depth d and period Λ. For an incident plane wave with an amplitude of unity, the aperture function can be expressed as a

convolution of *comb* with *rect* [97]. The phase term has a slope ϕ/Λ.

$$U(x) = comb(x/\Lambda) \otimes rect(x/\Lambda) exp(i\phi(x)/\Lambda) \tag{4.25}$$

where phase difference ϕ is $2\pi(n-1)d/\lambda$

Since the simplest diffractive lens is assumed to be a grating, the grating equation can be applied.

$$\Lambda \sin(\theta_m) = m\lambda \tag{4.26}$$

where m = diffraction order

The diffraction orders are the Fourier transform of U and the fraction of light in the m^{th} diffraction order is given by the magnitude squared the Fourier coefficients of that order [97].

$$\eta_m = [\sin(\pi(k-m))/\pi(k-m)]^2 \tag{4.27}$$

$$\eta_m = sinc^2(k-m) \tag{4.28}$$

If the diffraction order is 1 and the wavelength range is 360 nm to 1700 nm, the diffraction efficiency will be 100% at the design wavelength 550 nm. However, the diffraction efficiency decreases drastically for wavelengths other than the design wavelength as shown in the Figure 4.23.

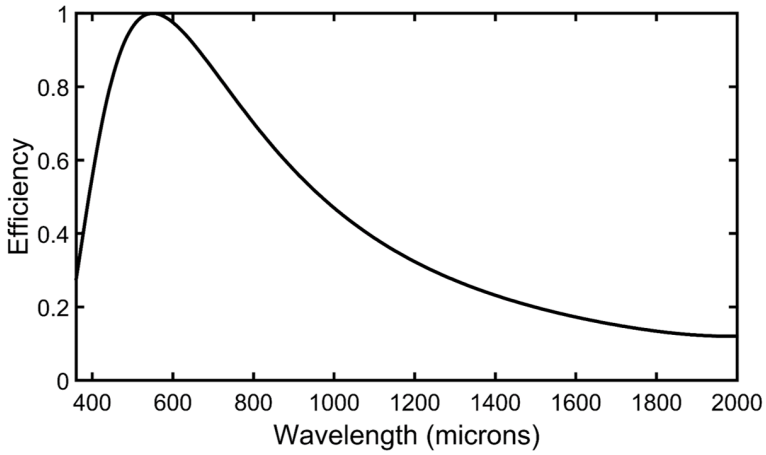

Figure 4.23: *Diffraction efficiency of a blazed lens.*

This implies that the diffraction lens based achromat although suitable for dispersion correction, the diffraction efficiency needs to be improved in order to be used for solar concentrator applications.

4.9 Summary

The most significant conclusions from this chapter include:

1. Maximizing optical efficiencies is of prime importance in order to obtain maximum module efficiencies. Therefore, system optimization needs to be performed with actual material properties for specific concentrations. Optical efficiencies >than 80% can be obtained at both the concentrations with the F-TP and the Fresnel lens only design.

2. The concentration and acceptance angle product for a particular design stays constant implying a reduction in acceptance angle with concentration. CPV optics can be

designed using Fresnel lenses alone. A secondary homogenizer may be added to improve homogeneity and acceptance angle. Acceptance half angles of 1.2 ° and 1 ° are obtained with a F-TP system at 846× and 1250× concentration respectively.

3. The Fresnel only design, promises higher optical efficiency at 846 suns due to the reduction in Fresnel reflection losses while optical efficiency lowers at 1250 sins. This design suffers from lower acceptance angles and higher PARs at both concentrations, which may increase loss penalties for CPV systems.

4. While the F-K design shows a lower optical efficiency and acceptance angle than the F-TP counterpart at 846× concentration, the tolerance to POE-SOE working distance is significantly higher with the F-K design. In addition, better illumination uniformity is also achieved with the F-K design.

5. Losses due to material dispersion can be reduced by designing an achromat using diffractive lenses. Diffractive efficiencies need to be improved to use this method for practical purposes.

Chapter 5

Integrating cells and optics

Efficiency of a CPV module depends on the efficiency of the optical system as well as the efficiency of the multijunction cell. High efficiency MJSCs combined with high-efficiency CPV optics are expected to provide high module efficiencies. However, if the optics and the MJSC are not designed in tandem with each other, loss penalties may arise. Hence, the design and optimization of cells and optics in an integrated manner is necessary.

While Chapters 3 and 4 of this thesis focused on the electrical and optical modeling of CPV systems independently, in this chapter, an integrated modeling approach is proposed. Outputs from the numerical simulations are integrated into the optical system simulations, and are input to the parametrized 2-D distributed circuit models (Figure 5.1). The integrated opto-electrical model can be used to simulate realistic CPV systems by including the effects of spectral and spatial nonuniform illumination profiles. In the first part of this chapter, a 1250× CPV system with a Fresnel lens POE and a truncated pyramid SOE is optimized for the 3JLM, the 3JIMM and, the 4JLM design using this integrated analysis.

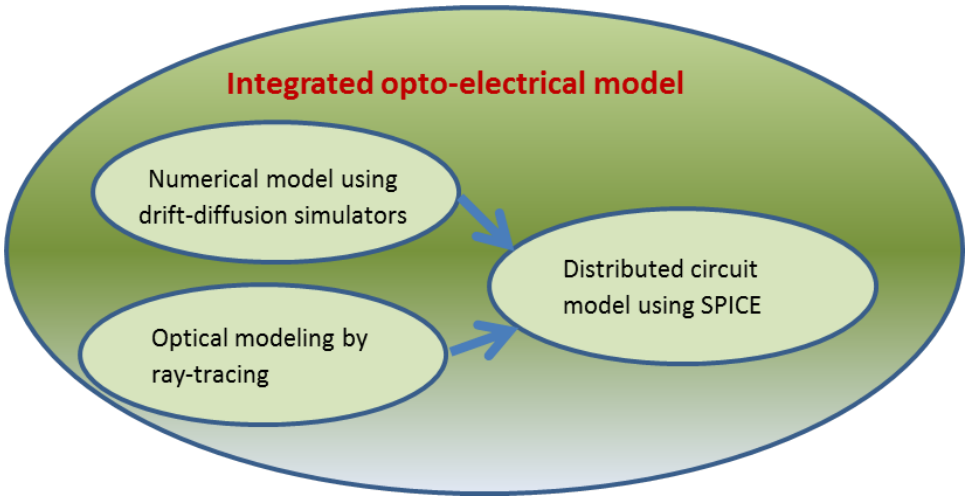

Figure 5.1: *Integrated modeling involves the outputs of distributed circuit model and the optical system model.*

The latter part of this chapter focuses on the results obtained by using this method for acceptance angle determination in a 625× system. Refractive concentrator architectures are studied using triple-junction solar cells and on-sun measurements of angular response are compared with results obtained using the integrated approach.

5.1 Modeling methodology

Modeling is performed under standard test conditions (STC: 25 ° C and 1000 W/m^2) using the parametrized distributed circuit models of each MJSC are developed by curve-fitting a two-diode, equivalent model to subcell I-V curves as detailed in Chapter 3. Since the subcell distributed circuit must see only those spectral components that it can harvest, the intensity-normalized AM1.5D spectrum is multiplied by the subcell EQE to acquire a virtual spectrum [76].

The relative optical power in each subcell block is found by ray tracing the total power in its virtual spectrum through the optical train using Zemax, giving the integrated optical power across the entire subcell depth, parallel to the grid line. The Sentaurus-derived subcell short circuit current density is rescaled by the functional block area, the relative optical power within that area, the 1000 W/m^2 reference intensity, and the geometric concentration to obtain the local current source value. The geometric concentration is fixed at 1250 suns.

System efficiency is determined for each MJSC from the I-V curve extracted from SPICE simulations of its distributed circuit. This is done across the range of critical system dimensions, identified as the POE-SOE working distance, the SOE entrance aperture width and the SOE height, and the maximum system efficiency is identified for each design under both uniform and nonuniform illumination conditions. Uniform illumination conditions are achieved by ignoring spatial variations by averaging each subcell irradiance profile over the entire subcell. This allows for comparative assessment between MJSC designs for the spectral and spatial variations produced by their optimized systems.

5.2 Simulation results

5.2.1 Spectral variation ignoring spatial nonuniformity

To first consider only the impact of spectral variation, any spatial variations in the optical efficiency are ignored by calculating the average profile intensity for each system.

Full system efficiencies are determined with each MJSC, across the nominal parameter

ranges for POE-SOE working distance, SOE height, and SOE aperture width. To see system sensitivities to these parameters, multidimensional results are presented in Figure 5.2 as system efficiency scatter plots for each design. Each color bar peaks at its maximum system efficiency and spans a one percent (absolute) range, so that the three designs may be quantitatively compared. It is noted that all designs show a reasonably well-defined but broad peak about the system maximum (indicated by a black rectangle around the hottest dot on a scatter plot). They likewise all show comparable response to variations in height, working distance, and aperture width of <0.02%, <0.05%, and <0.3% (absolute) per mm, respectively, in the vicinity of system efficiency maxima. The adjacent contour plot shows a slice of the plot at the optimal entrance aperture width. The optimal parameter values are summarized in Table 5.1. Interpreting these values in light of the variations seen in Figure 5.2 implies that one system design may be somewhat suitable for all cell designs without suffering a dramatic loss in efficiency. This implies that using 3JIMM and 4JLM cells in a 3JLM optimized system gives absolute efficiency reductions of <0.1% and approximately 1%, respectively.

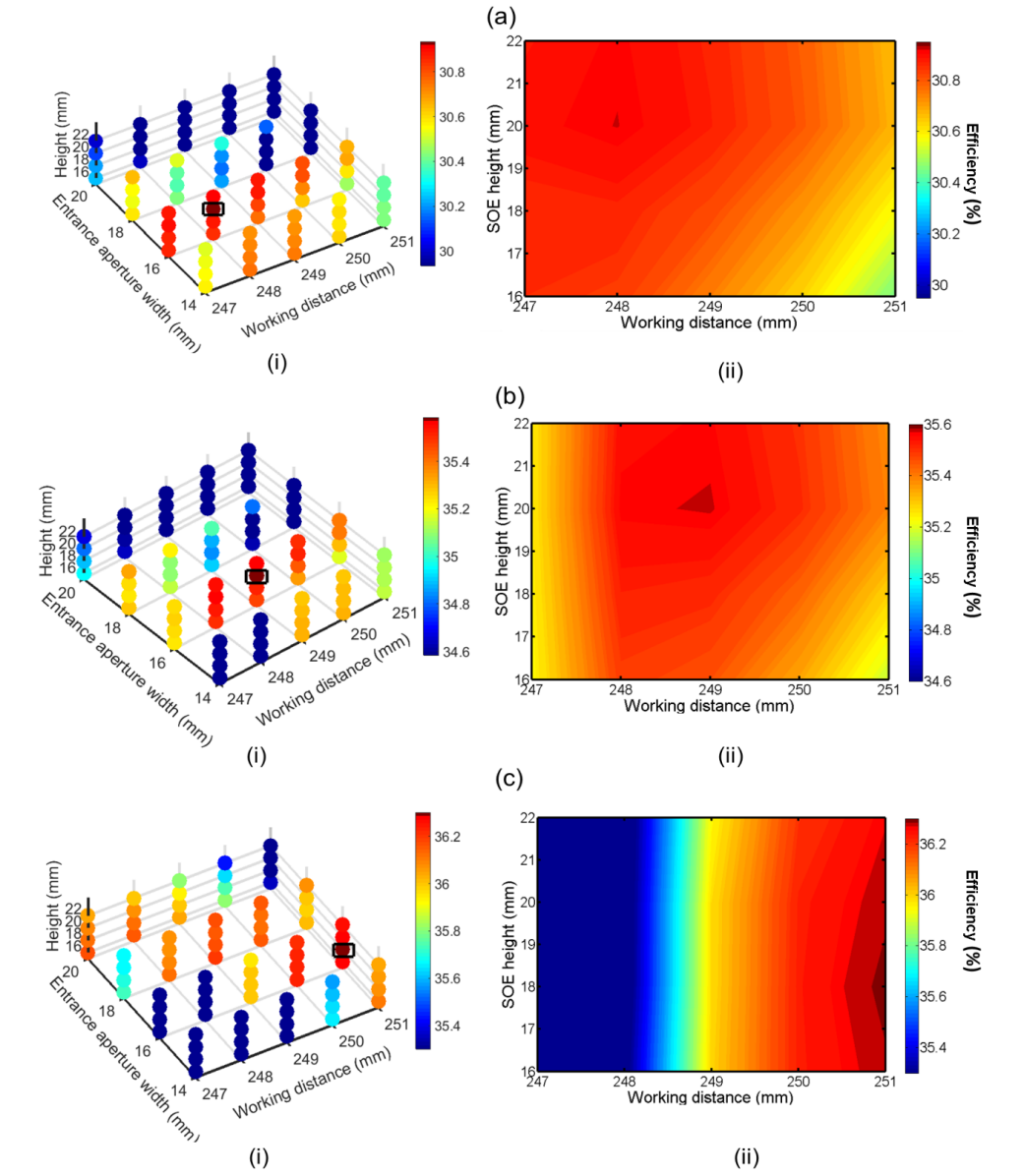

Figure 5.2: *Scatter plots (i) and contour plots (ii) showing the maximum efficiency (black rectangle) based only on spectral variation ignoring spatial effects for (a) 3JLM (b) 3JIMM and (c) 4JLM designs. The color bar shows the efficiency for each design. All scatter plots have the same parameter ranges; the efficiency range is also fixed, at 1% absolute for each design. The contour plots show the efficiency as a function of SOE height and working distance at the fixed, optimal entrance aperture widths.*

Table 5.1: *Optimal parameter values (mm) for maximum system efficiency with a 10 mm SOE exit aperture, for the three MJSC designs, with a 1250× optical system.*

Uniform illumination				**Nonuniform illumination**		
Design	**Working distance**	**Entrance aperture**	**SOE height**	**Working distance**	**Entrance aperture**	**SOE height**
3JLM	248	16	20	249	16	37
3JIMM	249	16	20	251	16	36
4JLM	251	16	18	252	18	36

Maximum system efficiencies and MJSC efficiencies are presented in Table 5.2. Note that all efficiencies are for uniform illumination at 1250 suns, so that comparison extracts the loss penalty due to the optical transfer function. A loss penalty may be associated with dispersive and non-dispersive components. Spectral variations associated with dispersion may current mismatch between subcells and therefore are separated for a detailed analysis. The non-dispersive component is seen by inspection of the OTF plateaus to be 15% and does affect current matching. The reader is referred to the OTF calculations in Chapter 4 to visualize this. The loss penalty is given as a relative (to the cell) percentage less 15% to permit quantitative design comparison since the cells have different efficiencies. Although, the greatest improvement in system response would be achieved by decreasing this loss, originating primarily due to reflections at the various interfaces.

Table 5.2 shows that spectral variations impose loss penalties of lower than 2% for all the three systems. The comparable loss penalties for the three-junction systems are primarily because the current balances between subcells one and two are impacted by similar roll-offs on the blue end of their OTFs. The 3JIMM sees a slightly lower loss penalty than

does the 3JLM because its bottom subcell is not sensitive to spectral variations in the OTF beyond 1200 nm, whereas the 3JLM does; but the difference is significant due to an overproducing bottom subcell. The larger loss penalty for the 4JLM system is primarily due to how the current balance between subcells one and four is disturbed by the OTF; the fourth subcell sees a greater impact than the first, while subcells two and three are not significantly impacted.

Table 5.2: *Design efficiencies (absolute %) and corresponding loss penalties for the three MJSC designs, with a 1250× optical system. A nondispersive baseline of 15% has been subtracted to show the effect of the variation.*

Maximum efficiency (%)			**Loss penalty (Relative %)**			
Design	**Cell (STC)**	**Uniform illumination**	**Nonuniform illumination**	**Spectral variation only**	**Spectral + spatial variation**	**Spatial variation only**
3JLM	36.9	30.9	30.5	1.3	2.3	1.1
3JIMM	42.4	35.6	34.0	1.0	4.8	3.8
4JLM	43.5	36.3	35.3	1.6	3.9	2.3

5.2.2 Spectral and spatial variations

In the previous section, the spatial variation in spectral mismatch has been neglected. To provide more realistic system efficiency estimates, the fully-two-dimensional distributed circuit model and the actual illumination profiles generated by ray tracing are used. Complete system efficiencies are determined using the integrated approach for all parameter combinations within nominal ranges around system efficiency maxima. The results are

shown in Figure 5.3 as scatter plots for each design. The color bars now span a three percent (absolute) range, in contrast to the one percent span in the earlier analysis. In contrast to earlier, all designs show a sharp peak about the system maximum (again indicated by a black rectangle around the hottest dot on a scatter plot). The three-junction designs show similar responses to variations in height, of about 0.3% (absolute) per mm while the four-junction design has a sensitivities of 0.8% and 0.1% per mm for heights lower and higher than optimal, respectively. The three-junction designs show a 0.6% per mm design sensitivity in working distance while the four-junction design has a 1.5% per mm sensitivity. For the entrance aperture width, the sensitivities for all designs are $< 0.3\%$ per mm. Again, contour plots are included in order to highlight the system maxima at a fixed entrance aperture width.

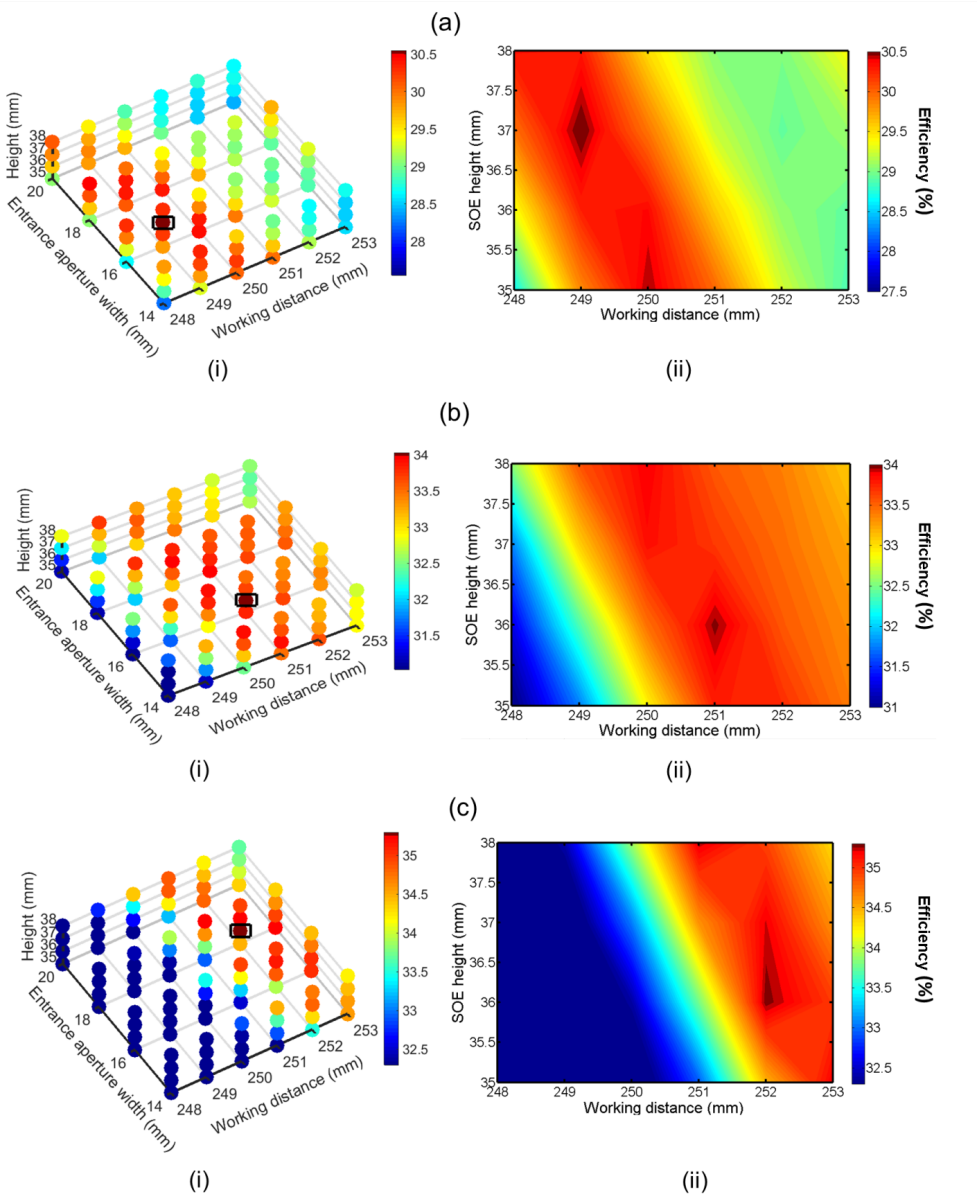

Figure 5.3: *Scatter plots (i) and contour plots (ii) showing the maximum efficiency (black rectangle) based only on spectral variation including spatial and spectral effects for (a) 3JLM (b) 3JIMM and (c) 4JLM designs. The color bar shows the efficiency for each design. The contour plots show the efficiency as a function of SOE height and working distance at a fixed, optimal entrance aperture width. The color bars now span over a 3% absolute range for system efficiency.*

The optimal parameter values obtained including spatial variations are summarized in Table 5.1. Comparison with the uniform illumination case finds similar values for working distances and entrance apertures, but considerably different values for SOE heights. Since spatial variations are included, now almost doubled SOE heights are required to enable total internal reflection to homogenize the nonuniform profile as much as possible. System efficiencies are now far more sensitive to variations in working distance and aperture width, greater than ten times both for the height and the working distance. The sensitivity to entrance aperture width stays less than 0.3% per mm. Interpreting parameter values in light of the variations seen in Figure 5.3 implies that one system design cannot be used for all cell designs without suffering a dramatic loss in efficiency. For example, using 3JIMM and 4JLM cells in a 3JLM optimized system gives absolute loss penalties of 1% and 3.4%, respectively. This is in marked contrast to the earlier case; it underlines the critical need for a full system optimization under realistic cell illumination conditions.

Maximum system efficiencies are summarized again in Table 5.2. Comparison of results obtained under uniform and nonuniform illumination reveals that system efficiencies decrease under nonuniform spatial profiles. The most significant reduction is for the 3JIMM design, while the impact appears to worsen for the LM designs with a higher number of junctions. To ascertain the origin of such losses, the loss penalties are again quantified in Table 5.2 relative to its cell efficiency under uniform spectral and spatial profile. The impact of both spectral and spatial variations on the 3JIMM design is seen to be more than twice as severe as their impact on the 3JLM design (4.8% vs. 2.3%); their impact on the 4JLM design lies between these values. To gain further insight, spatial and spectral effects

are decoupled linearly and so the spectral only loss penalty is subtracted from the spectral + spatial loss penalty to determine the loss penalty due solely to spatial variations. This penalty is more than 3.5 times greater for the 3JIMM design (3.8%) than for the 3JLM design (1.1%), but only about twice as great for the 4JLM design (2.3%). The impact of spatial variation on the 3JIMM design is seen to be a much more severe than the impact of spectral variation, somewhat more severe for the 4JLM design, and slightly less severe for the 3JLM design. To understand these dependencies, the current distributions within each subcell are consideted. For each design, Figure 5.4 shows the distributed circuit source currents, which are calculated from the subcell short-circuit current distributions. For the 3JLM design, Figure 5.4(a) shows that the top subcell clearly limits current production across the entire device. The middle subcell slightly overproduces in the central region, but is otherwise well matched; the bottom subcell heavily overproduces at the edges, and is only well matched in a smaller central region. The small loss penalty of 1.08% noted in Table 5.2 is therefore likely due to minor lateral current flows associated with matched currents that are slightly higher (by about 20%) in the central region than on the edges.

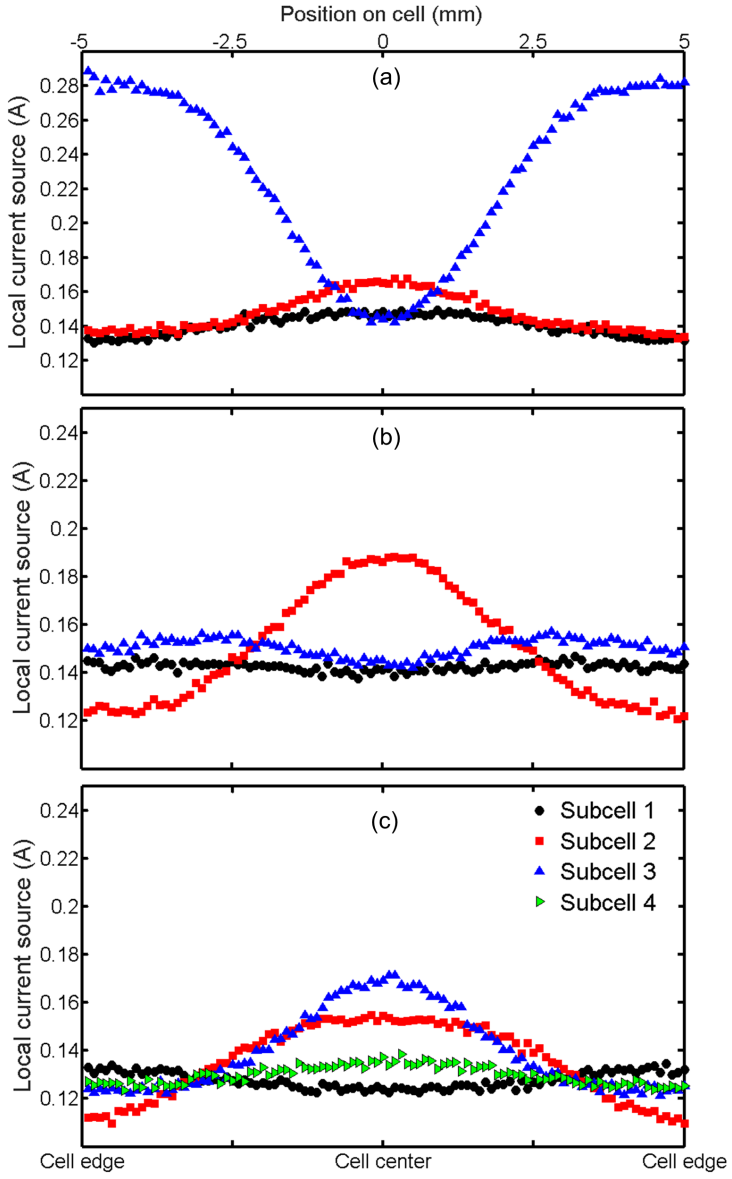

Figure 5.4: *Local current source distributions on the (a) 3JLM (b) 3JIMM and (c) 4JLM cells at the optimal parameter values as obtained using our full system optimization. The local current source value is obtained by rescaling the current density obtained at 1000 W/m2, the illuminated area within a functional unit, the relative optical power within that area, and the geometric concentration. Bottom subcell limiting behavior cannot be ignored for fully current-matched configurations, such as the 3JIMM and the 4JLM in this study.*

For the 3JIMM design, Figure 5.4 (b) shows top and bottom subcells closely current matched across their reasonably flat profiles. However, the middle subcell strongly over-produces in the central region, but correspondingly underproduces at the edges. All else being equal, lateral current flows in the middle cell from the center to the edge should act to achieve an overall current balance, yielding negligible loss penalty. The large loss penalty of 3.8% noted in Table 5.2 arises from the dissipative effect of the large lateral resistances (on average 6.9 Ω see Chapter 3, Table 3.1) and higher overall currents. The same is true to a lesser degree for the 4JLM design, where subcell currents shown in Figure 5.4(c) have distributions similar to that of the 3JIMM cell. Again, top and bottom subcells are closely current matched across their reasonably flat profiles. The middle two subcells strongly overproduce in the central region, but only subcell 2 significantly under-produces at the edges. Less spatial inhomogeneity, and less dissipation, due to somewhat smaller subcell 2 lateral resistances (on average, 2.4 Ω), means a smaller loss penalty should be observed, as is indeed noted in Table 5.2. The integrated approach, therefore, helps in better system optimization and can lead to enhanced system efficiencies.

5.3 Acceptance angle measurement

In order to validate the effectiveness of the integrated approach, acceptance angle measurements are performed with concentrator modules. Three prototype, refractive-concentrator based CPV modules mounted on a commercial dual-axis, solar tracker (GoldenSun model GS3500) were studied to check tracker precision. The modules are located at one of the SUNLAB facilities in Ottawa. The tracker design is a circular azimuth railway carrying

a horizontal elevation shaft located near the center-of-mass of the payload scaffold and the sun position sensor is a four-quadrant photodiode array with a shadow-mask. While the results of this study are included in [100], the comparison of the results from the integrated approach and the field measurements is presented here, briefly. All the designs are based on the 3JLM cell. The tracker is normally operated using signals from a sun sensor mounted directly to its payload scaffold under active closed-loop control. Angular response is measured by determining the I_{sc}. For each angular response measurement:

1. The tracker position was calibrated for known time of day (UTC) and known sun position determined using the NREL SOLPOS sun position calculator [101];

2. The NREL SOLPOS calculator was then used to determine sun position about 30 minutes in advance of a center time and the tracker was advanced to that position and stopped;

3. As the sun moved along its arc at about 0.25° per minute, I_{sc} was manually recorded on a 1-minute timebase with a separate handheld digital ammeter for each prototype, and sun positions in the sun align jig were noted.

The raw I_{sc} vs time datasets were normalized and I_{sc} response vs tracker deviation angle were determined. These results were obtained in only one direction of sun travel.

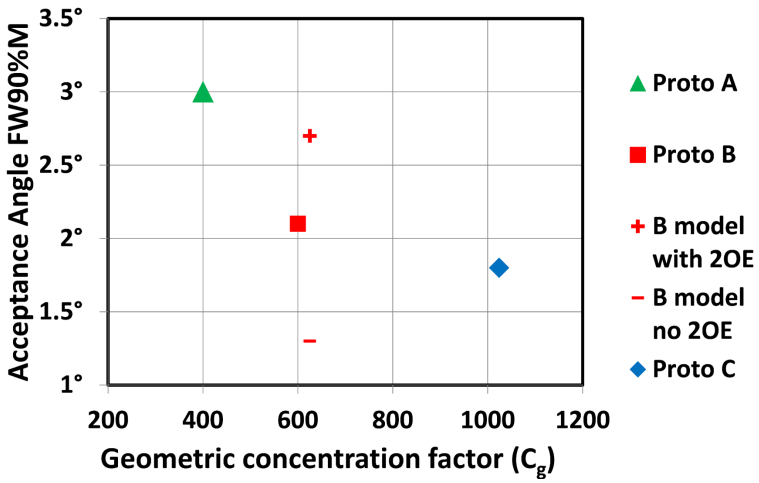

Figure 5.5: *Measured and modeled angular response, as a function of geometric concentration for different refractive architectures. Prototype B was modeled with and without the SOE.*

Prototype B was a system with a Fresnel lens and an SOE. Modeling angular acceptance of a single channel in Prototype B yielded similar results to the measured values. However, some discrepancy was noted. The discrepancy could be attributed to variation among the six channels, which is expected to degrade the acceptance angle due to the losses in electrical interconnection, Fresnel lens warp and discoloration after several years on-sun. The substantial effect of the SOE in improving angular response is evident. It should also be noted that since the distributed resistance model considers spectrally varying spatial profiles, the effect of non-uniform illumination is included in the results obtained using the integrated approach. In the case of a concentrator system without the SOE, the peak-to-average irradiance values are much higher and can therefore lead to higher series resistances losses due to greater localized concentrations as described in Chapter 3 of this thesis.

5.4 Summary

Multiparameter system optimization using integrated opto-electrical modeling, employing ray tracing and SPICE modeling, is carried out for 3JLM, 3JIMM and 4JLM cell designs. A consequence of the optical system are the nonuniform spatial and spectral illumination profiles at the MJSC with loss penalties varying, depending on the MJSC design. Nonuniform illumination represents a less-than-ideal scenario for MJSCs, but its effect can be partly mitigated by allowing excessive currents to flow laterally through alternative paths. However, high lateral resistances impede current flow and cause loss penalties. While spectral variations alone have the greatest impact ($< 1.5\%$ relative loss penalty) on the 4JLM design due to its longer wavelength absorption range, loss penalties due to spatial variations are significantly higher ($< 3.5\%$ relative) for 3JIMM design, primarily due to its high lateral resistance. Lateral resistance varies depending on layer thicknesses, doping concentrations and mobilities of charge carriers. These parameters are typically optimized for maximum efficiency under uniform illumination profiles, leading to loss penalties under realistic, nonuniform illumination profiles. Such loss penalties may be reduced if the MJSC subcell layers are specifically designed to accommodate nonuniform illumination profiles. Simulation results also indicate that optical system optimization be performed in concert with the specific MJSC design in order to obtain maximum system efficiencies.

In addition, the on-sun tracker measurements suggest that the integrated approach yields results similar to those obtained in the field and can be a valuable tool to assess and compare designs. It can also allow the calculation of energy yields over different spectrums for different locations.

Chapter 6

Temperature effects

6.1 Introduction

The efficiency of a MJSC is temperature as well as irradiance dependent. Operation at high concentration leads to an elevation in cell temperature and therefore, an increase in the dark current. Although reduction in bandgap increases the short-circuit current, an increase in recombination dominates over the J_{sc} increase, reducing the overall efficiency at high temperatures. Therefore, modeling temperature effects reliably in MJSCs is critical to determine the performance in real world conditions. Such studies have been carried out in the past for CPV systems based on triple junction cells [102], [103], [104]. However, analysis of temperature effects on four-junction cells and comparative analysis between 3J and 4J structures has not been reported. It is also imperative to study the temperature effects for cells consisting of newer materials and structure as the modeling methodology may change depending on the behavior of each layer to changes in temperature. A rise

in ambient temperature affects all components of a CPV system. Similar to the flat-plate technologies, CPV module efficiencies suffer due to a rise in temperature [105], but the detrimental effects are much reduced as compared to flat-plate silicon cells. Analysis and mitigation of the detrimental effects of temperature increase is an important part of the design and characterization of CPV systems. While both cells and CPV optics are affected by an increase in temperature [106], this work focuses on the influence of temperature on the MJSCs. The 2-D distributed circuit model is extended to incorporate temperature effects for three-junction, lattice-matched and four-junction, lattice-matched, dilute-nitride based solar cells and the results are validated by laboratory measurements with 3JLM isotypes. Before the extended distributed circuit model is discussed, a brief description of temperature-dependent MJSC parameters is presented.

6.1.1 Solar cell bandgap

The bandgap of most semiconductors decreases with temperature. An increase thermal energy increases the interatomic spacing thereby decreasing the potential seen by the electrons, lowering the material bandgap. For typical semiconductors, the temperature dependence of bandgap is expressed using the Varshni equation [107]

$$E_g = E_0 - \alpha.T^2/(T + \beta) \tag{6.1}$$

E_g is the bandgap at temperature T, E_0 is the bandgap at 0 K, and α and β are constants.

While most semiconductors follow the Varshni equation, the dilute-nitride material does

not comply and instead a band-anticrossing model is typically used [108], [109]. Dilute nitrides materials typically use GaAs semiconductors with the addition of nitrogen which allows for not only reducing the bandgap but also the lattice constant of the compound material. This bandgap tunability of dilute nitride material has made it a useful option for the third subcell in a 3JSC and a 4JSC. Band-anticrossing, in a dilute-nitride like material, can be described as the interaction between the single energy level of the nitrogen atoms and the conduction band of the host semiconductor. The result is a separation of the bands, and a concentration-dependent bandgap, which can be described by [109]:

$$E_g = 1/2 \left[(E_{gNN} + E_N) - \sqrt{(E_{gNN} + E_N)^2 + 4W^2 y} \right] \tag{6.2}$$

E_{gNN} is the bandgap for the non-nitride materials, calculated using the Varshni equation, E_N and W are material composition-dependent model parameters, and y is the nitrogen mole-fraction. For the material $In_xGa_{1-x}As_{1-y}N_y$, the In concentration has an influence on the bandgap as well and the entire bandgap can be modeled as a function of temperature as described in [109]. In this case E_{gNN} would be calculated for the InGaAs alloy, depending on composition and the value will be substibuted in equation 6.2. Figure 6.1 shows the bandgap as a function of temperature for $In_xGa_{1-x}As_{1-y}N_y$ where the mole fraction of indium is 0.11 and that of nitrogen is 0.0037.

6.1.2 Open-circuit voltage

With a rise in temperature, the equilibrium population of electrons is increased leading to an increase in the dark current density (J_0). An increase in dark current leads to

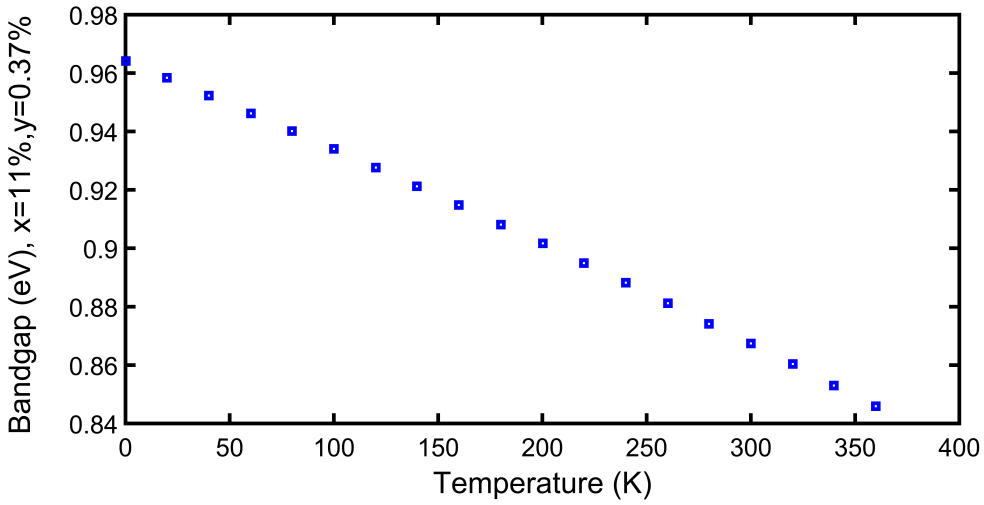

Figure 6.1: *Bandgap as a function of temperature for* $In_xGa_{1-x}As_{1-y}N_y$.

a reduction in open circuit voltage. V_{oc} is the most sensitive parameter to changes in temperature, which leads to a reduction in efficiency.

6.1.3 Short-circuit current

With the lowering of the bandgap, due to an increase in temperature, high-energy photons can now be absorbed, leading to an increase in the J_{sc} for single-junction cells. For MJSCs however, there might be a decrease in the short-circuit current for the bottom subcell(s) of the MJSC due to the shift in bandgap, which may lead to a reduction in the number of photons to the bottom subcells. Also, a change in bandgap may also change the current-limiting subcell, thus varying the J_{sc}. Overall, if there is a small increase, this increase is, typically, not significant, as compared to the reduction in V_{oc} and so does not have a large impact on cell efficiency.

6.1.4 Fill factor

A change in FF due to a temperature rise is primarily related to the temperature coefficient of V_{oc}. Apart from the V_{oc}, in the case of multijunction cells, changes in bandgap may lead to spectral mismatch, leading to a change in fill-factor.

6.1.5 Efficiency

A decrease in solar cell efficiency is seen with a rise in temperature. The temperature coefficient of the solar cell efficiency can be computed using the temperature coefficients of J_{sc}, V_{oc} and FF, the impact of temperature coefficient of the V_{oc} being the greatest. Although operation at high-temperature reduces cell efficiencies, this effect is much reduced under concentration. Thus, the idea of using MJSCs under concentration at elevated temperatures gains more ground.

6.2 Modeling temperature effects in MJSCs

6.2.1 Model description

The distributed resistance model has been expanded to include the effects on temperature on MJSCs. In particular, the following changes have been implemented to each functional unit.

The recombination current calculation should include temperature dependence [110], which is represented by:

$$J_0(T) = J_0(T_{ref}) \left(\frac{T}{T_{ref}}\right)^{3+Xti} \exp\left[\frac{-qE_g}{k_b T}\left(1 - \frac{T}{T_{ref}}\right)\right] \tag{6.3}$$

$$J_{02}(T) = J_0(T_{ref}) \left(\frac{T}{T_{ref}}\right)^{\frac{3+Xti}{2}} \exp\left[\frac{-qE_g}{2k_b T}\left(1 - \frac{T}{T_{ref}}\right)\right] \tag{6.4}$$

J_0 and J_{02} are the recombination current densities at temperature T, Xti represents the temperature coefficient of saturation current, k_b is Boltzmann's constant and T_{ref} is the reference temperature. For non-nitride subcells, the value of Xti has been obtained from Ota et al. [110]. For the dilute-nitride subcell, this value has been fixed to 2.2 for the simulations, similar to the InGaAs value in [110]. The bandgaps have been included in LTSPICE on the basis of the original design for the 4JLM as described in Chapter 2. Temperature is defined in the SPICE netlist for all the functional units. In addition, due to the lack of relevant data for the bandgaps corresponding to the 4JLM, the temperature coefficient of short-circuit current has been approximated from [111], [112].

6.3 3JLM experimental results

In order to validate the SPICE modeling, 1 cm^2 isotypes for 3JLM cells were used. I-V curves were obtained using the Oriel 92191 solar simulator, which is powered by a 1600 W xenon lamp. The simulator is capable of uniformly illuminating MJSCs upto a concentration 150 suns and has a temperature-controlled platform for measurements. Air mass filters were used to set-up the AM1.5 spectrum. The parameters, obtained with $<2\%$ error, were extracted using MATLAB's curve-fitting toolbox and are presented in the

Appendix.

In order to validate the SPICE results with experimental data, temperature dependent measurements were performed with standard 3JLM cells and the results were compared with the SPICE model. Figure 6.2 shows a comparison of the the I-V curves obtained by experiment and by SPICE simulation.

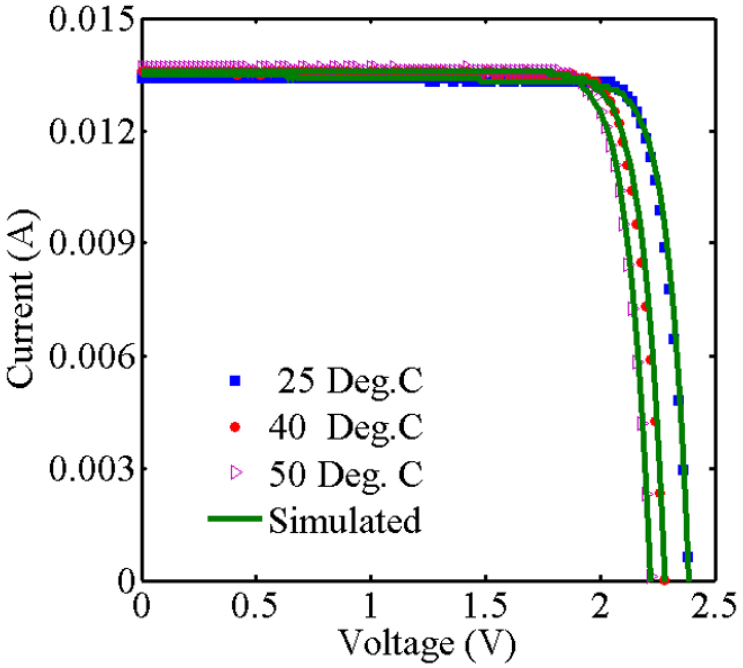

Figure 6.2: *Measured and simulated I-V curves at different temperatures for a 3JLM cell.*

Further, the temperature coefficient of V_{oc} was determined by varying temperatures on the ORIEL simulator platform. The values have been measured at temperatures from 25 to 70°C at 1.2 suns. The spectral mismatch was accounted for in the calculations to determine the concentration. While the measured value of the temperature coefficient of V_{oc} was -6.69 mV/ °C, the simulated value was -6.66 mV/ °C. The temperature coefficient of efficiency was calculated to be the same (0.08%/ °C) using both the methods.

In addition, to evaluate the model at higher concentrations, values obtained using published data are compared with the simulation results. Figure 6.3 shows a comparison of the published values of the temperature coefficient of V_{oc} compared with simulation results from this thesis for the 3JLM cell [102], [113].

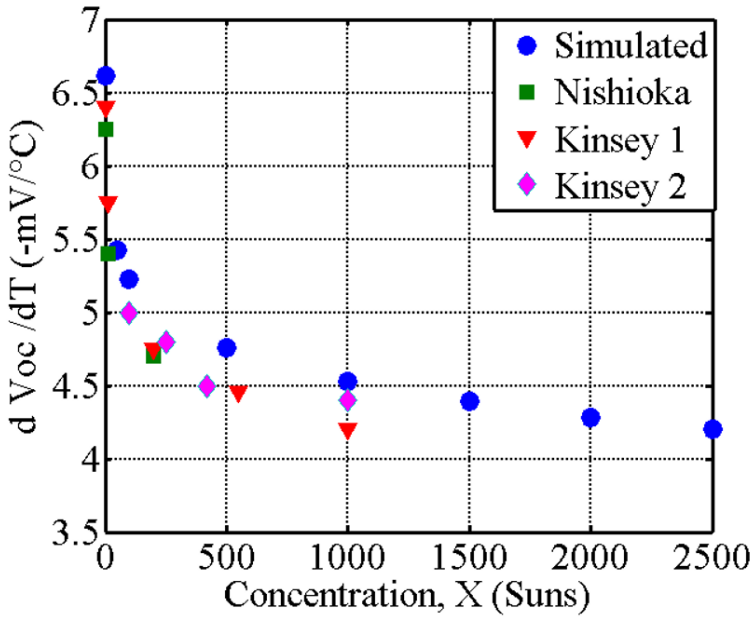

Figure 6.3: *Measured values (obtained from published data [102], [113] and simulated I-V curves at different concentrations for a 3JLM cell.*

6.4 Experimental results - Single-junction dilute nitride based cell

In order to determine the bandgap dependence of the dilute-nitride subcell and to calculate the temperature coefficient of I_{sc}, spectral response measurements were performed for a single-junction dilute-nitride subcell, designed at SUNLAB and grown at National Research

Council, targeted for a 4JLM configuration. The structure is shown in Figure 6.4. The thickness of the dilute-nitride layer is 650 nm in this design. Additional details and material properties can be obtained from [37]. The cell size was 5 mm x 5 mm.

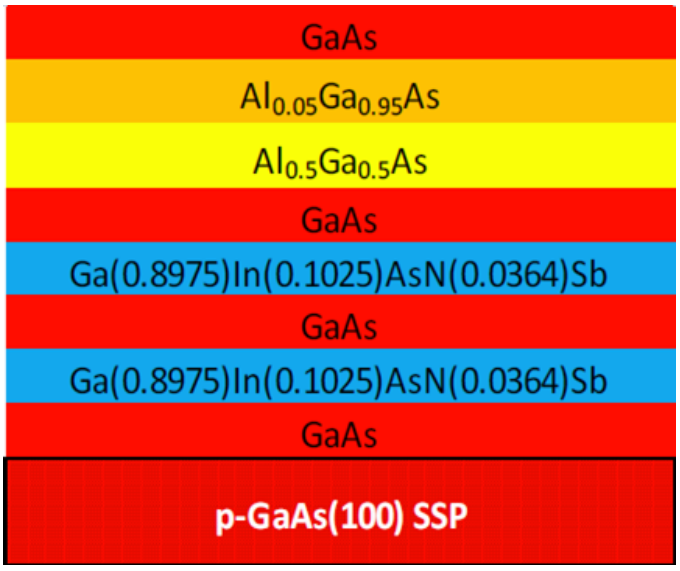

Figure 6.4: *Layer structure for a single junction dilute nitride solar cell designed for application in a 4JLM. Higher bandgap layers with appropriate bandgaps are grown in order to simulate the top layers in a 4JLM structure.*

Figure 6.5 shows the EQE measured over different temperatures. Based on these curves, the temperature coefficient of I_{sc} was determined to be -60μA/°C.

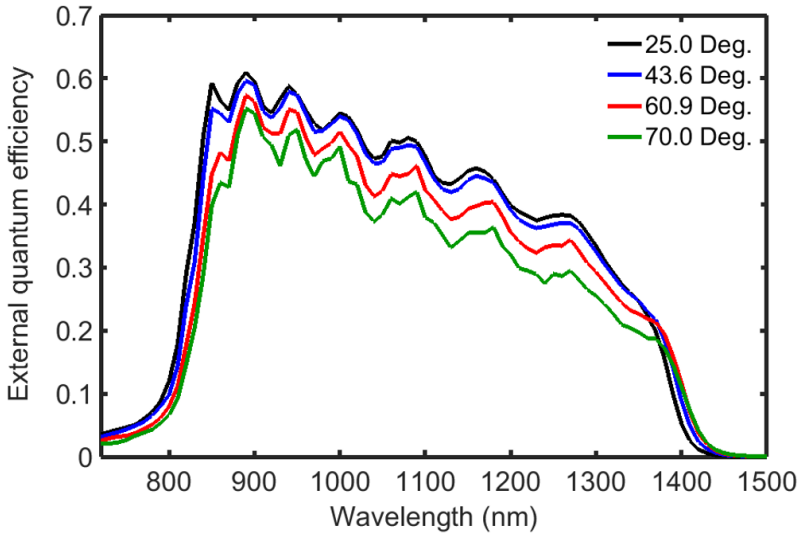

Figure 6.5: *EQE as a function of wavelength at different temperatures for the dilute-nitride sample.*

In addition, the I-V curves were also measured in 5° increments from 15 to 70° C. Figure 6.6 shows the I-V curves obtained using this sample.

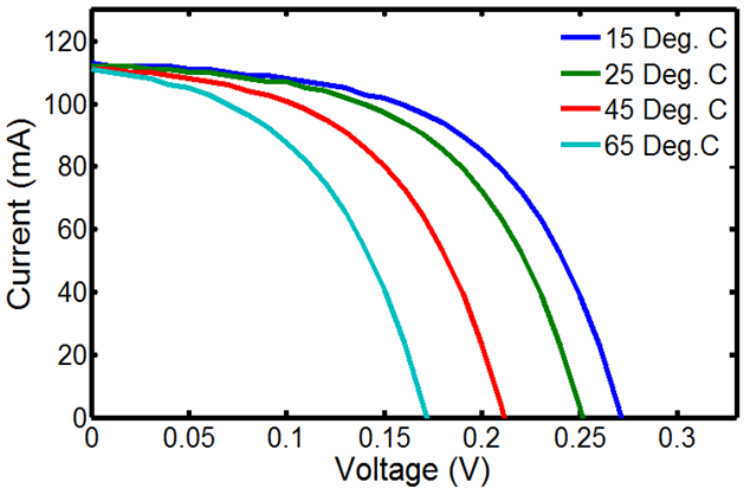

Figure 6.6: *I-V curves at different temperatures for a single-junction dilute-nitride based solar cell.*

The temperature coefficient of V_{oc} was also measured using the I-V curve data. Figure 6.7 shows the reduction in V_{oc} as a function of temperature. The temperature coefficient of V_{oc} was determined to be -1.9 mV/ °C

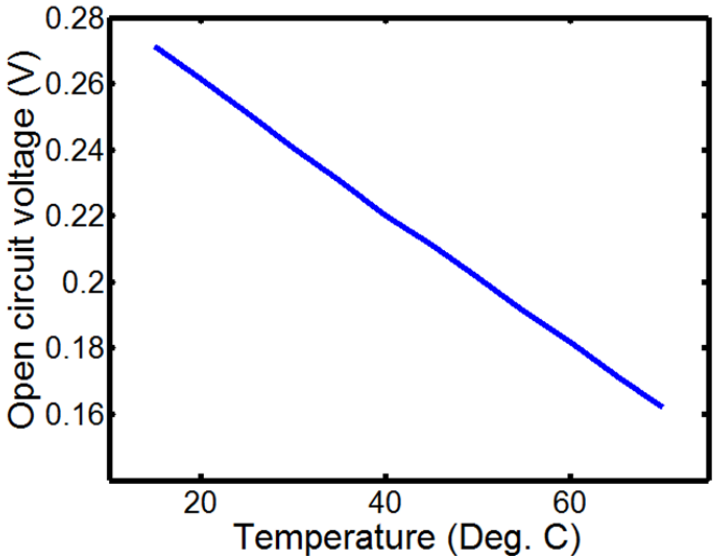

Figure 6.7: *Variation in V_{oc} as a function of temperature for the dilute-nitride sample.*

6.5 Simulation results for the 4JLM

Simulations for the 4JLM have been performed with 5% shading for a 1 cm^2 cell area. Simulations have been performed both under uniform and under nonuniform illumination and temperature profiles under 8 different concentrations. Figure 6.8 shows the change in the temperature coefficient of V_{oc} with concentration under uniform illumination and uniform temperature profile compared with the performance under nonuniform illumination (Gaussian profile with a PAR = 3) and a uniform temperature profile.

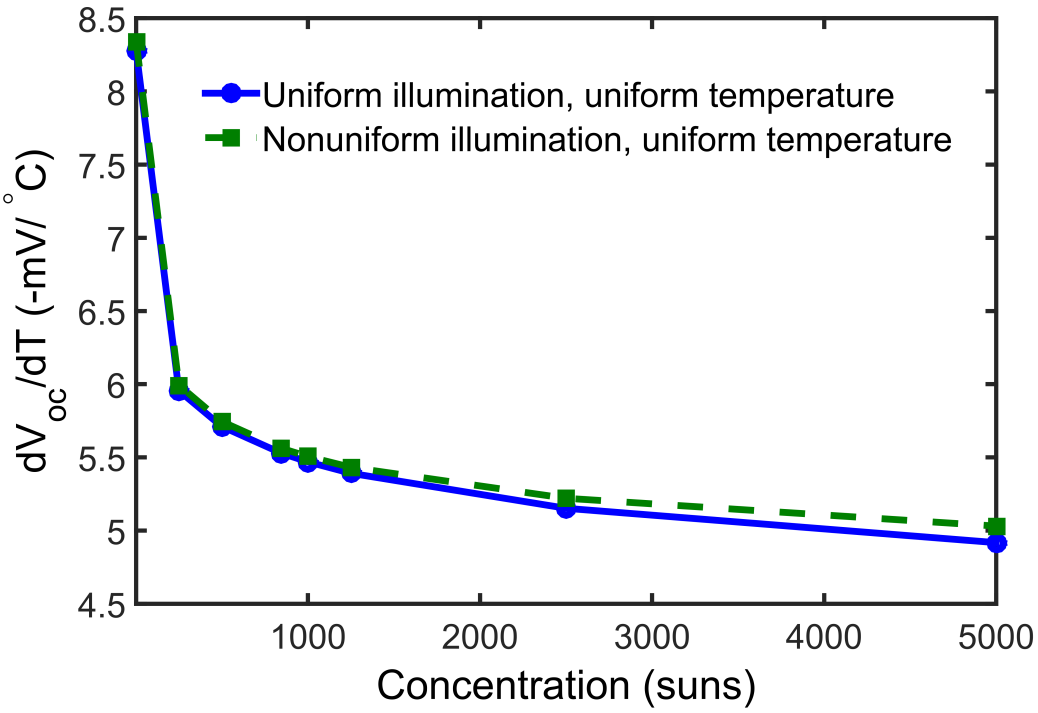

Figure 6.8: *Open-circuit voltage as a function of concentration for the 4JLM cell under uniform and nonuniform illumination profiles. The temperature profile is uniform.*

Although nonuniform illumination profiles are known to cause a reduction in V_{oc} and efficiency, as described in Chapter 3, the temperature coefficient of V_{oc} does not suffer

drastically as long as the temperature profile is maintained to be uniform. It can be seen that there is a change in V_{oc} at lower concentrations, while for higher concentrations (>1000 suns) the temperature coefficient of V_{oc} is slightly reduced for the nonuniform illumination case. This could be due to the higher localized concentration caused by the Gaussian profile. Since the temperature profile is still maintained to be constant, higher overall temperatures do not have a significant effect on the temperature coefficient of V_{oc} in these localized areas, thus leading to a slightly lower temperature coefficient of V_{oc}.

In order to evaluate performance over a nonuniform temperature profile, a Gaussian temperature profile with a PAR = 1.5 and an average temperature of 60 °C is used. Figure 6.9 shows the change in efficiency as a function of concentration with a nonuniform illumination (Gaussian PAR = 3) and a nonuniform temperature profile (Gaussian peak-to-average temperature = 1.5).

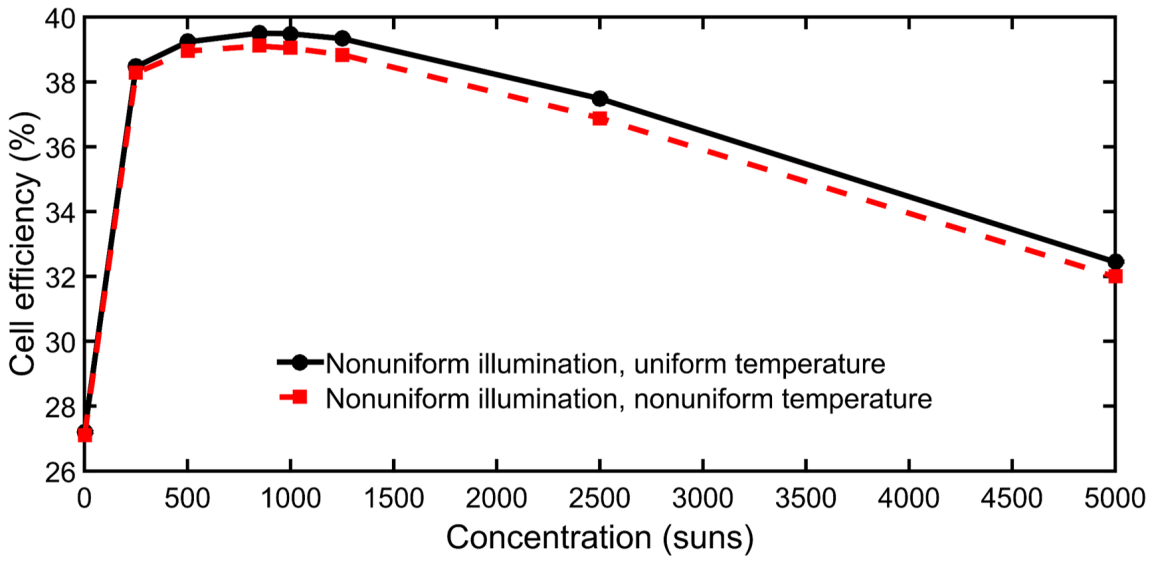

Figure 6.9: *Efficiency as a function of concentration under nonuniform and uniform temperature profiles.*

Simulation results indicate the effect of a nonuniform temperature profile over a range of concentrations. Efficiency decreases if a nonuniform illumination profile is used with a nonuniform temperature profile. This effect is more pronounced with an increase in concentration. It can also be inferred that a highly efficient heat-sink, which can flatten the temperature profile, can be used with a nonuniform illumination profile to mitigate losses.

6.6 Summary

Higher temperatures greatly affect the operation of MJSCs by reducing V_{oc} and therefore cell efficiency. The 2-D distributed circuit model has been extended to include the effects of temperature and has been successfully validated for a 3JLM cell by laboratory measurements.

A dilute-nitride based single junction cell design, targeted for use in a 4JLM, is evaluated and EQE and I-V curves are measured over a range of temperatures. Simulations are conducted for 4JLM cell under uniform and nonuniform illumination and temperature profiles. Nonuniform illumination profiles with uniform temperatures do not show any remarkable change in the temperature coefficient of V_{oc}. Under nonuniform illumination and nonuniform temperature profiles, the efficiency of an MJSC suffers drastically. It can be seen that losses can be mitigated if a uniform temperature profile can be maintained on the cell, irrespective of the illumination profiles.

Chapter 7

Conclusions

Research is to see what everybody else has seen,

and to think what nobody else has thought.

Albert Szent-Gyorgyi

7.1 Conclusions

In this thesis, refractive-concentrator systems, based on multijunction solar cells have been modeled and analyzed, with an intent to enable high-concentration, high-efficiency CPV systems. The main findings of this thesis are summarized as follows:

Modeling and simulation play an important role in the analysis of CPV systems, specially for optimization and analysis of novel designs. Three and four-junction solar cells were modeled using a drift-diffusion simulator, and efficiencies of 37%, 42.5% and 43.4% were obtained for the 3JLM, 3JIMM and 4JLM designs respectively, under 1000 suns (uni-

form illumination). While numerical modeling approaches are useful for understanding the physical processes governing the solar cell and for simulation of small-symmetrical elements, distributed circuit models are required to analyze effects of nonuniform illumination on concentrator solar cells. An improved 2-D distributed model, parametrized for the three MJSC designs, was presented. The implementation of a four-junction cell in a distributed resistance model is a novel contribution of this work. Cell efficiencies were predicted using this model, over a range of concentrations, under both uniform and nonuniform illumination profiles. While previous studies have reported results for 3JLM under specific, design concentrations, this work looked at the performance of newer designs such as the 3JIMM and the 4JLM, working under concentrations other than the designed concentration. The effect of nonuniform illumination was analyzed using spatially and spectrally varying Gaussian distributions. A range of Gaussian distributions was used in order to simulate different types of CPV optics. Such a detailed analysis has not been reported in the past, to the best of author's knowledge. While the absolute loss penalties at 1250 suns, due to spatial nonuniformity at PAR = 3, for the lattice-matched designs were <1.5% , these penalties were >3% for the 3JIMM. Further reduction in efficiency was caused due to spectrally varying spatially profiles, which could be partly mitigated by reducing the sheet resistance of the current-limiting subcell, as simulated for the 3JIMM design.

Efficiency enhancements could be potentially achieved, even under uniform illumination, if finger spacings were optimized based on the specific concentration. Loss penalties due to nonuniform illumination profiles could be partly mitigated, if finger spacings were optimized on the basis of the specific nonuniform illumination profiles targeted for a specific

MJSC design, with smaller cell sizes being more favorable for handling nonuniformities.

The inclusion of luminescent coupling led to >5% absolute efficiency enhancement for the 3JIMM design, implying that losses due to spectrally varying spatial profiles could be partly mitigated by designing structures which allow for radiated photons to be coupled from the higher to the lower bandgap subcells.

Ray-tracing models, with realistic material properties, were created for three refractive CPV systems, namely: the Fresnel lens system, Fresnel POE with truncated pyramid SOE, and the 4-fold Fresnel Köhler system. System optimization, performed with actual material properties, for specific concentrations indicated that optical efficiencies >than 80% can be obtained with all the three designs. A reduction in acceptance angle with concentration was observed. While the F-K design showed a lower optical efficiency and acceptance angle than the F-TP counterpart at 846× concentration, the tolerance to POE-SOE working distance was significantly higher with the F-K design. In addition, better illumination uniformity is also achieved with the F-K design. A comparative analysis, such as the one presented here, at 846× concentration, has not beeen presented elsewhere and can be useful for CPV system designers.

A technique for mitigating losses due to material dispersion was proposed by designing an achromat using diffractive lenses. While the net chromatic shift was reduced, the theoretical efficiency of the diffractive lens was low and requires further investigation.

An integrated approach, combining ray-tracing with distributed circuit modeling was proposed. The F-TP system was optimized for the three MJSC designs to obtain maximum efficiency with changes in working distance, SOE entrance aperture width and SOE height

at 1250 suns. The integrated approach allowed for the analysis of illumination profiles, decoupling the loss penalties due to spectral and spatial nonuniformities. While the 3JIMM showed the greatest sensitivity to spatial nonuniformities (similar to the result obtained by the cell efficiency analysis with Gaussian PARs), the 4JLM design was the most sensitive to spectral nonuniformities. Such an analysis has not been reported in the literature thus far and aims to provide feedback to CPV system designers, without manufacturing the cell or the optic. The approach was tested with on-sun measurements with a similar CPV system.

A brief analysis of temperature-based effects was performed and experimental results were presented for the 3JLM. EQE and I-V curve measurements over temperature were presented for a single-junction cell based on dilute-nitride material and simulation results were presented for the 4JLM both over nonuniform illumination and nonuniform temperature profiles.

7.2 Future work

The issues, which may be investigated, as an extension of this research, are enumerated as follows:

- With the MJSCs advancing to an even higher number of junctions, it would be beneficial to expand the distributed resistance model to include a larger number of junctions, with different material properties.

- With the increase in computational speeds available with advanced CPUs, a 3-D

model based on Bethe lattice can be used.

- Although AM1.5D is considered a reference spectrum for CPV system analysis, solar spectrum changes significantly based on geographical locations and atmospheric conditions. These can be taken into account in the ray-tracing models and optical efficiencies can be evaluated for a particular location. CPV optics could be selected based on location.

- Prediction of energy yield using the integrated approach could be another area where this work can be extended. Although several models for energy prediction exist currently, spatial nonuniformities are typically ignored. By using a 2-D model, this prediction can be made more accurately without the need for very high computational resources.

- MJSCs are typically optimized for uniform illumination and normal incidence. It would be valuable to analyze the variation in spatial profiles as a function of angular input to the MJSC. The performance of the anti-reflective coatings could be analyzed over a range of input angles as a function of position on the MJSC. This can potentially be performed using the distributed resistance model, extended with an angular dependence component.

- A thorough study on the effects of temperature including the effect on CPV optics would be interesting and might provide ideas for mitigation of losses in CPV systems. These studies, if directed towards the more novel 4J designs, would be beneficial for heat-sink designers.

- Finally, on-sun measurements with the 3JIMM and 4JLM systems, now available commercially, would be an important step in validating the results presented in this thesis.

APPENDICES

Appendix A

Material properties of silicone adhesive

The material properties of the silicone adhesive are described below. Figure A.1 shows the transmission as a function of wavelength through a thickness of 1 mm. This adhesive has been used in the F-K design.

Index at d-light : 1.40845168

Abbe at d-light : 57.87175643

Dispersion Formula used: Schott

A0 : 1.964954670E+000

A1 : -5.419468291E-003

A2 : 1.041285002E-004

A3 : 4.753067602E-003

A4 : -1.070711745E-003

A5 : 9.223033828E-005

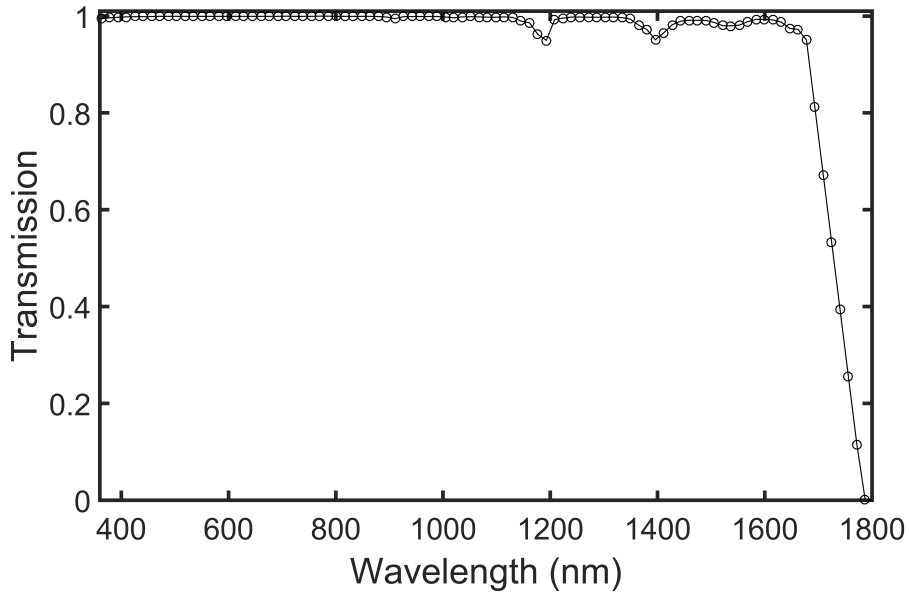

Figure A.1: *Transmission through 1 mm of the silicone-adhesive material.*

Appendix B

SPICE parameters for experimental 3JLM

Table B.1: *The SPICE parameters for the 3JLM design extracted from subcell IV curves obtained from Spectrolab isotypes.*

3JLM	$\mathbf{I}_{01}$ **(A)**	$\mathbf{I}_{02}$ **(A)**	$\mathbf{R}_{sh}$ **(kΩ)**	$\mathbf{R}_{L}$ **(Ω)**
Top subcell	1.5×10^{-25}	3.7×10^{-14}	15	R_{L1}= 1.2 , R_{L2} = 6.6
Middle subcell	3.1×10^{-20}	5.9×10^{-11}	7.5	R_{L3} = 0.4 , R_{L4} = 0.8
Bottom subcell	1.6×10^{-6}	1.7×10^{-5}	3.5	R_{L5} = 0.3

References

[1] M. Hosenuzzaman, N. A. Rahim, J. Selvaraj, M. Hasanuzzaman, A. B. M. A. Malek, and A. Nahar, "Global prospects, progress, policies, and environmental impact of solar photovoltaic power generation," *Renewable and Sustainable Energy Reviews*, vol. 41, pp. 284–297, Jan. 2015.

[2] S. P. Europe, " Global Market Outlook, For Solar Power 2015-2019," tech. rep., European Photovoltaic Industry Association, 2016.

[3] M. A. Green, K. Emery, Y. Hishikawa, W. Warta, and E. D. Dunlop, "Solar cell efficiency tables (version 47)," *Progress in Photovoltaics: Research and Applications*, vol. 24, no. 1, pp. 3–11, 2016. PIP-15-272.

[4] W. Shockley and H. J. Queisser, "Detailed balance limit of efficiency of p-n junction solar cells," *Journal of applied physics*, vol. 32, no. 3, pp. 510–519, 1961.

[5] J. Fossum, E. Burgess, and F. Lindholm, "Silicon solar cell designs based on physical behavior in concentrated sunlight," *Solid-State Electronics*, vol. 21, no. 5, pp. 729–737, 1978.

[6] E. Burgess and D. Pritchard, "Performance of a one kilowatt concentrator photovoltaic array utilizing active cooling," tech. rep., Sandia Labs., Albuquerque, N. Mex.(USA), 1978.

[7] R. Sinton, Y. Kwark, J. Gan, and R. M. Swanson, "27.5-percent silicon concentrator solar cells," *IEEE Electron Device Letters*, vol. 7, no. 10, pp. 567–569, 1986.

[8] R. M. Swanson, "The promise of concentrators," *Progress in Photovoltaics Research and Applications*, vol. 8, no. 1, pp. 93–111, 2000.

[9] A. L. Luque and A. Viacheslav, *Concentrator photovoltaics*. Springer, 2007.

[10] P. Chiang, D. Kurt, B. Cavicchi, K. Bertness, S. Kurtz, and J. Olson, "Large area GaInP/GaAs/Ge multijunction solar cells for space applications," in *Photovoltaic Energy Conversion, 1994., Conference Record of the Twenty Fourth. IEEE Photovoltaic Specialists Conference-1994, 1994 IEEE First World Conference on*, vol. 2, pp. 2120–2123, IEEE, 1994.

[11] M. B. Spitzer and J. C. Fan, "Multijunction cells for space applications," *Solar Cells*, vol. 29, no. 2, pp. 183–203, 1990.

[12] L. Fraas, J. Avery, V. Sundaram, V. Dinh, T. Davenport, J. Yerkes, J. Gee, and K. Emery, "Over 35% efficient GaAs/GaSb stacked concentrator cell assemblies for terrestrial applications," in *Photovoltaic Specialists Conference, 1990., Conference Record of the Twenty First IEEE*, pp. 190–195, IEEE, 1990.

[13] D. Friedman, S. R. Kurtz, K. Bertness, A. Kibbler, C. Kramer, J. Olson, D. King, B. Hansen, and J. Snyder, "Accelerated publication 30.2% efficient GaInP/GaAs

monolithic two-terminal tandem concentrator cell," *Progress in Photovoltaics: Research and Applications*, vol. 3, no. 1, pp. 47–50, 1995.

[14] M. Dunlap, "Solar radiation data manual for flat-plate and concentrating collectors," *NASA STI/Recon Technical Report N*, vol. 95, p. 12647, 1994.

[15] W. Nishikawa, S. Horne, and J. Melia, "Lcoe for concentrating photovoltaics (CPV)," in *International Conference on Solar Concentrators for the Generation of Electricity (ICSC-5) Technical Digest*, 2008.

[16] NREL and F. I. for Solar Energy Systems ISE, "Current Status of Concentrator Photovoltaic (CPV) technology," tech. rep., Fraunhofer Institute for Solar Energy Systems ISE and National Renewable Energy Laboratory, 02 2016.

[17] "Dropping silicon prices threaten CPV industry." `http://www.solarnovus.com/dropping-silicon-prices-threaten-cpv-industry_N4404.html`. Accessed: 2016-07-05.

[18] X. Wang, L. Kurdgelashvili, J. Byrne, and A. Barnett, "The value of module efficiency in lowering the levelized cost of energy of photovoltaic systems," *Renewable and Sustainable Energy Reviews*, vol. 15, no. 9, pp. 4248–4254, 2011.

[19] J. E. Haysom, O. Jafarieh, H. Anis, K. Hinzer, and D. Wright, "Learning curve analysis of concentrated photovoltaic systems," *Progress in Photovoltaics: Research and Applications*, vol. 23, no. 11, pp. 1678–1686, 2015.

[20] N. L. A. Chan, H. E. Brindley, and N. J. Ekins-Daukes, "Impact of individual atmospheric parameters on CPV system power, energy yield and cost of energy," *Progress in Photovoltaics: Research and Applications*, vol. 22, no. 10, pp. 1080–1095, 2014.

[21] C. Algora, A. Martì, and A. Luque, "Next generation photovoltaics: High efficiency through full spectrum utilization," 2004.

[22] A. Mokri and M. Emziane, "Concentrator Photovoltaic Technologies and Market: A Critical Review," in *World renewable energy congress*, pp. 2738–2742, Nov. 2011.

[23] D. Talavera, P. Pérez-Higueras, J. Ruíz-Arias, and E. Fernández, "Levelised cost of electricity in high concentrated photovoltaic grid connected systems: spatial analysis of spain," *Applied Energy*, vol. 151, pp. 49–59, 2015.

[24] M. Buljan, J. Mendes-Lopes, P. Benítez, and J. C. Miñano, "Recent trends in concentrated photovoltaics concentrators architecture," *Journal of Photonics for Energy*, vol. 4, no. 1, pp. 040995–040995, 2014.

[25] J. Nelson, *The physics of solar cells*. Imperial College Press, 2003.

[26] P. Wrfel, "Thermodynamic limitations to solar energy conversion," *Physica E: Low-dimensional Systems and Nanostructures*, vol. 14, no. 12, pp. 18 – 26, 2002.

[27] G. P. Smestad, *Optoelectronics of solar cells*. Spie Press, 2002.

[28] "Reference Solar Spectral Irradiance: Air Mass 1.5.." `http://rredc.nrel.gov/solar/spectra/am1.5/`. Accessed: 2016-08-10.

[29] C. Maragliano, A. Zayan, and M. Stefancich, "Three-dimensional point-focus spectral splitting solar concentrator system," *International Journal of Optics and Applications*, vol. 4, no. 4A, pp. 6–11, 2014.

[30] L. Castaner and S. Silvestre, *Modelling photovoltaic systems using PSPICE*. John Wiley and Sons, 2002.

[31] L. C. Hirst and N. J. Ekins-Daukes, "Fundamental losses in solar cells," *Progress in Photovoltaics: Research and Applications*, vol. 19, no. 3, pp. 286–293, 2011.

[32] A. Mojiri, R. Taylor, E. Thomsen, and G. Rosengarten, "Spectral beam splitting for efficient conversion of solar energya review," *Renewable and Sustainable Energy Reviews*, vol. 28, pp. 654–663, 2013.

[33] B. Burnett, *The basic physics and design of III-V multijunction solar cells*, 2002 (accessed June 21, 2016). `http://educypedia.karadimov.info/library/NREL.pdf`.

[34] D. Derkacs, R. Jones-Albertus, F. Suarez, and O. Fidaner, "Lattice-matched multijunction solar cells employing a 1 ev GaInNAsSb bottom cell," *Journal of Photonics for Energy*, vol. 2, no. 1, pp. 021805–1, 2012.

[35] W. Guter, R. Kern, W. Köstler, T. Kubera, R. Löckenhoff, M. Meusel, M. Shirnow, and G. Strobl, "III-V multijunction solar cellsnew lattice-matched products and development of upright metamorphic 3J cells," in *7th International conference on concentrating photovoltaic systems: CPV-7*, vol. 1407, pp. 5–8, AIP Publishing, 2011.

[36] "New world record for solar cell efficiency at 46% French-German cooperation confirms competitive advantage of European photovoltaic industry." https://www.ise.fraunhofer.de/en/press-and-media/press-releases/press-releases-2014/new-world-record-for-solar-cell-efficiency-at-46-percent. Accessed: 2016-08-12.

[37] R. Cheriton, M. M. Wilkins, P. Sharma, C. E. Valdivia, A. H. Trojnar, H. Schriemer, K. Hinzer, J. Gupta, B. Bouzazi, G. Kolhatkar, *et al.*, "Design optimizations of ingaasn (sb) subcells for concentrator photovoltaic systems," *Journal of Vacuum Science & Technology B*, vol. 34, no. 2, p. 02M103, 2016.

[38] R. R. King, A. Boca, W. Hong, X. Liu, D. Bhusari, D. Larrabee, K. Edmondson, D. Law, C. Fetzer, S. Mesropian, *et al.*, "Band-gap-engineered architectures for high-efficiency multijunction concentrator solar cells," in *24th European Photovoltaic Solar Energy Conference and Exhibition, Hamburg, Germany*, vol. 21, 2009.

[39] R. King, D. Law, K. Edmondson, C. Fetzer, R. Sherif, G. Kinsey, D. Krut, H. Cotal, and N. Karam, "Metamorphic and lattice-matched solar cells under concentration," in *2006 IEEE 4th World Conference on Photovoltaic Energy Conference*, vol. 1, pp. 760–763, IEEE, 2006.

[40] A. W. Bett, F. Dimroth, W. Guter, R. Hoheisel, E. Oliva, S. P. Philipps, J. Schöne, G. Siefer, M. Steiner, A. Wekkeli, *et al.*, "Highest efficiency multi-junction solar cell for terrestrial and space applications," *space*, vol. 25, no. 25.8, pp. 30–6, 2009.

[41] J. Schultz, M. Klausmeier-Brown, M. L. Ristow, L. Partain, M. Al-Jassim, and K. Jones, "Development of high-quantum-efficiency, lattice-mismatched, 1.0-ev GaInAs solar cells," *Journal of electronic materials*, vol. 22, no. 7, pp. 755–761, 1993.

[42] J. Geisz, D. Friedman, J. Ward, A. Duda, W. Olavarria, T. Moriarty, J. Kiehl, M. Romero, A. Norman, and K. Jones, "40.8% efficient inverted triple-junction solar cell with two independently metamorphic junctions," *Applied Physics Letters*, vol. 93, no. 12, p. 123505, 2008.

[43] R. M. France, J. F. Geisz, I. García, M. A. Steiner, W. E. McMahon, D. J. Friedman, T. E. Moriarty, C. Osterwald, J. S. Ward, A. Duda, *et al.*, "Design flexibility of ultrahigh efficiency four-junction inverted metamorphic solar cells," *IEEE Journal of Photovoltaics*, vol. 6, no. 2, pp. 578–583, 2016.

[44] K. Tanabe, D. J. Aiken, M. W. Wanlass, A. F. I. Morral, and H. A. Atwater, "Lattice-mismatched monolithic GaAs/InGaAs two-junction solar cells by direct wafer bonding," in *2006 IEEE 4th World Conference on Photovoltaic Energy Conference*, vol. 1, pp. 768–771, IEEE, 2006.

[45] D. C. Law, R. King, H. Yoon, M. Archer, A. Boca, C. Fetzer, S. Mesropian, T. Isshiki, M. Haddad, K. Edmondson, *et al.*, "Future technology pathways of terrestrial III-V multijunction solar cells for concentrator photovoltaic systems," *Solar Energy Materials and Solar Cells*, vol. 94, no. 8, pp. 1314–1318, 2010.

[46] K. Derendorf, S. Essig, E. Oliva, V. Klinger, T. Roesener, S. P. Philipps, J. Benick, M. Hermle, M. Schachtner, G. Siefer, *et al.*, "Fabrication of GaInP/GaAs//Si solar cells by surface activated direct wafer bonding," *IEEE Journal of Photovoltaics*, vol. 3, no. 4, pp. 1423–1428, 2013.

[47] F. Dimroth, M. Grave, P. Beutel, U. Fiedeler, C. Karcher, T. N. Tibbits, E. Oliva, G. Siefer, M. Schachtner, A. Wekkeli, *et al.*, "Wafer bonded four-junction GaInP/GaAs//GaInAsP/GaInAs concentrator solar cells with 44.7% efficiency," *Progress in Photovoltaics: Research and Applications*, vol. 22, no. 3, pp. 277–282, 2014.

[48] K. Barnham, I. Ballard, J. Barnes, J. Connolly, P. Griffin, B. Kluftinger, J. Nelson, E. Tsui, and A. Zachariou, "Quantum well solar cells," *Applied Surface Science*, vol. 113, pp. 722–733, 1997.

[49] A. W. Walker, O. Thériault, and K. Hinzer, "Carrier dynamics in quantum-dot multijunction solar cells under concentration," *IEEE Journal of Photovoltaics*, vol. 4, no. 4, pp. 1095–1099, 2014.

[50] J. M. Gee and G. F. Virshup, "A 31%-efficient gaas/silicon mechanically stacked, multijunction concentrator solar cell," tech. rep., Sandia National Labs., Albuquerque, NM (USA), 1988.

[51] P. Chiu, S. Wojtczuk, X. Zhang, C. Harris, D. Pulver, and M. Timmons, "42.3% efficient ingap/gaas/ingaas concentrators using bifacial epigrowth," in *Photovoltaic Specialists Conference (PVSC), 2011 37th IEEE*, pp. 000771–000774, IEEE, 2011.

[52] A. Marti and A. Luque, *Next generation photovoltaics - High efficiency through full spectrum utilization*. Institute of physics publishing, 2004.

[53] "Process and Device Simulation Tools to Accelerate Innovation." `http://www.synopsys.com/tools/tcad/Pages/default.aspx`. Accessed: 2016-07-26.

[54] "Device Simulation Framework." `http://www.silvaco.com/products/tcad/device_simulation/atlas/atlas.html`. Accessed: 2016-07-26.

[55] L. D. Nielsen, "Distributed series resistance effects in solar cells," *IEEE Transactions on electron devices*, vol. 29, no. 5, pp. 821–827, 1982.

[56] A. Zekry and A. Y. Al-Mazroo, "A distributed SPICE-model of a solar cell," *IEEE Transactions on Electron Devices*, vol. 43, no. 5, pp. 691–700, 1996.

[57] K. Araki and M. Yamaguchi, "Extended distributed model for analysis of non-ideal concentration operation," *Solar energy materials and solar cells*, vol. 75, no. 3, pp. 467–473, 2003.

[58] K. Nishioka, T. Takamoto, T. Agui, M. Kaneiwa, Y. Uraoka, and T. Fuyuki, "Evaluation of InGaP/InGaAs/Ge triple-junction solar cell under concentrated light by simulation program with integrated circuit emphasis," *Japanese journal of applied physics*, vol. 43, no. 3R, p. 882, 2004.

[59] B. Galiana, C. Algora, and I. Rey-Stolle, "Comparison of 1d and 3d analysis of the front contact influence on GaAs concentrator solar cell performance," *Solar Energy Materials and Solar Cells*, vol. 90, no. 16, pp. 2589–2604, 2006.

[60] P. Espinet, I. García, I. Rey-Stolle, C. Algora, and M. Baudrit, "Extended description of tunnel junctions for distributed modeling of concentrator multi-junction solar cells," *Solar Energy Materials and Solar Cells*, vol. 95, no. 9, pp. 2693–2697, 2011.

[61] I. Rey-Stolle, C. Algora, I. García, M. Baudrit, P. Espinet, B. Galiana, and E. Barrigon, "Simulating III-V concentrator solar cells: a comparison of advantages and limitations of lumped analytical models; distributed analytical models and numerical simulation," in *2009 34th IEEE Photovoltaic Specialists Conference (PVSC)*, 2009.

[62] "LTSPICE IV." `http://www.linear.com/designtools/software/#LTspice`. Accessed: 2016-08-19.

[63] K. Nishioka, T. Takamoto, T. Agui, M. Kaneiwa, Y. Uraoka, and T. Fuyuki, "Evaluation of InGaP/InGaAs/Ge triple-junction solar cell and optimization of solar cell's structure focusing on series resistance for high-efficiency concentrator photovoltaic systems," *Solar Energy Materials and Solar Cells*, vol. 90, no. 9, pp. 1308–1321, 2006.

[64] P. Sharma, A. Walker, J. Wheeldon, H. Schriemer, and K. Hinzer, "Optimization of finger spacing for concentrator photovoltaic cells under non-uniform illumination using spice," in *Photonics North 2013*, pp. 891505–891505, International Society for Optics and Photonics, 2013.

[65] J. F. Wheeldon, C. E. Valdivia, A. W. Walker, G. Kolhatkar, A. Jaouad, A. Turala, B. Riel, D. Masson, N. Puetz, S. Fafard, *et al.*, "Performance comparison of AlGaAs, GaAs and InGaP tunnel junctions for concentrated multijunction solar cells,"

Progress in Photovoltaics: Research and Applications, vol. 19, no. 4, pp. 442–452, 2011.

[66] "CPV Point Focus Solar Cells." `http://www.spectrolab.com/DataSheets/PV/CPV/C4MJ_40_Percent_Solar_Cell.pdf`. Accessed: 2016-08-18.

[67] G. Segev, G. Mittelman, and A. Kribus, "Equivalent circuit models for triple-junction concentrator solar cells," *Solar Energy Materials and Solar Cells*, vol. 98, pp. 57–65, 2012.

[68] "Curve Fitting Toolbox - MATLAB." `http://www.mathworks.com/products/curvefitting/`. Accessed: 2016-09-27.

[69] L. Fu, R. Leutz, and H. P. Annen, "Secondary optics for fresnel lens solar concentrators," in *SPIE Optical Engineering+ Applications*, pp. 778509–778509, International Society for Optics and Photonics, 2010.

[70] R. Herrero, M. Victoria, C. Domínguez, S. Askins, I. Antón, and G. Sala, "Concentration photovoltaic optical system irradiance distribution measurements and its effect on multi-junction solar cells," *Progress in Photovoltaics: Research and Applications*, vol. 20, no. 4, pp. 423–430, 2012.

[71] C. Algora, "The importance of the very high concentration in third-generation solar cells," *Next Generation Photovoltaics*, pp. 108–136, 2003.

[72] C. Algora and V. Díaz, "Influence of series resistance on guidelines for manufacture of concentrator p-on-n GaAs solar cells," *Progress in Photovoltaics: Research and Applications*, vol. 8, no. 2, pp. 211–225, 2000.

[73] H. Baig, K. C. Heasman, and T. K. Mallick, "Non-uniform illumination in concentrating solar cells," *Renewable and Sustainable Energy Reviews*, vol. 16, no. 8, pp. 5890 – 5909, 2012.

[74] H. Baig, N. Sarmah, K. C. Heasman, and T. K. Mallick, "Numerical modelling and experimental validation of a low concentrating photovoltaic system," *Solar Energy Materials and Solar Cells*, vol. 113, pp. 201–219, 2013.

[75] H. Cotal and R. Sherif, "The effects of chromatic aberration on the performance of GaInP/GaAs/Ge concentrator solar cells from fresnel optics," in *Conference Record of the Thirty-first IEEE Photovoltaic Specialists Conference, 2005.*, pp. 747–750, IEEE, 2005.

[76] M. Victoria, R. Herrero, C. Domínguez, I. Antón, S. Askins, and G. Sala, "Characterization of the spatial distribution of irradiance and spectrum in concentrating photovoltaic systems and their effect on multi-junction solar cells," *Progress in Photovoltaics: Research and Applications*, vol. 21, no. 3, pp. 308–318, 2013.

[77] R. King, "Ultra-high efficiency multijunction cell and receiver module, Phase 1B: high performance PV exploring and accelerating ultimate pathways," *National Renewable Energy Laboratory, Boulder, Colorado, Tech. Rep. NREL/SR-520-47602*, 2010.

[78] P. Sharma, A. W. Walker, J. F. Wheeldon, K. Hinzer, and H. Schriemer, "Enhanced efficiencies for high-concentration, multijunction pv systems by optimizing grid spacing under nonuniform illumination," *International Journal of Photoenergy*, vol. 2014, 2014.

[79] I. Garcia, C. Algora, I. Rey-Stolle, and B. Galiana, "Study of non-uniform light profiles on high concentration III–V solar cells using quasi-3d distributed models," in *Photovoltaic Specialists Conference, 2008. PVSC'08. 33rd IEEE*, pp. 1–6, IEEE, 2008.

[80] D. Derkacs, D. T. Bilir, and V. A. Sabnis, "Luminescent coupling in GaAs/GaInNAsSb multijunction solar cells," *IEEE Journal of Photovoltaics*, vol. 3, no. 1, pp. 520–527, 2013.

[81] D. J. Friedman, J. F. Geisz, and M. A. Steiner, "Effect of luminescent coupling on the optimal design of multijunction solar cells," *IEEE Journal of Photovoltaics*, vol. 4, no. 3, pp. 986–990, 2014.

[82] A. S. Brown and M. A. Green, "Radiative coupling as a means to reduce spectral mismatch in monolithic tandem solar cell stacks theoretical considerations," in *Photovoltaic Specialists Conference, 2002. Conference Record of the Twenty-Ninth IEEE*, pp. 868–871, IEEE, 2002.

[83] J. Jia, F. Suarez, T. Bilir, V. Sabnis, and J. Harris, "3-d modeling of luminescent coupling effects in multijunction concentrator solar cells," in *10th International Conference on Concentrator Photovoltaic Systems: CPV-10*, vol. 1616, pp. 3–7, AIP Publishing, 2014.

[84] C. Algora and I. Rey-Stolle, "Handbook on concentrator photovoltaic technology," 2016.

[85] J. Wheeldon, A. W. Walker, O. Theriault, M. Yandt, and K. Hinzer, "Numerical simulations of temperature dependence of high-efficiency multi-junction solar cells under concentrated sunlight," in *Access Networks and In-house Communications*, p. JTuB21, Optical Society of America, 2011.

[86] S. Kurtz *et al.*, "Opportunities and challenges for development of a mature concentrating photovoltaic power industry," 2009.

[87] W. Xie, Y. Dai, R. Wang, and K. Sumathy, "Concentrated solar energy applications using fresnel lenses: A review," *Renewable and Sustainable Energy Reviews*, vol. 15, no. 6, pp. 2588 – 2606, 2011.

[88] R. Leutz and A. Suzuki, *Nonimaging Fresnel lenses: design and performance of solar concentrators*, vol. 83. Springer, 2012.

[89] M. Victoria, C. Domínguez, I. Antón, and G. Sala, "Comparative analysis of different secondary optical elements for aspheric primary lenses," *Opt. Express*, vol. 17, pp. 6487–6492, Apr 2009.

[90] R. Winston, J. C. Miñano, P. G. Benitez, *et al.*, *Nonimaging optics*. Academic Press, 2005.

[91] M. Hernández, A. Cvetkovic, P. Benítez, and J. Miñano, "High-performance kohler concentrators with uniform irradiance on solar cell," in *Optical Engineering+ Applications*, pp. 705908–705908, International Society for Optics and Photonics, 2008.

[92] "Ventana design by LPI." `http://www.lpi-llc.com/pdf/Ventana2012.pdf`. Accessed: 2016-10-13.

[93] K. Chong, F. Siaw, C. Wong, and G. Wong, "Design and construction of non-imaging planar concentrator for concentrator photovoltaic system," *Renewable Energy*, vol. 34, no. 5, pp. 1364–1370, 2009.

[94] "Acrylite Solar material."
URL: http://www.acrylite-shop.com/pdfs/232-23-ACRYLITE-Solar-0Z023-en-Cyro.pdf.

[95] M. Velderrain, "Choosing a silicone encapsulant for photovoltaic applications," in *7th International conference on concentrating photovoltaic systems: CPV-7*, vol. 1407, pp. 79–83, AIP Publishing, 2011.

[96] P. Benítez, J. C. Miñano, P. Zamora, R. Mohedano, A. Cvetkovic, M. Buljan, J. Chaves, and M. Hernández, "High performance fresnel-based photovoltaic concentrator," *Optics Express*, vol. 18, no. 101, pp. A25–A40, 2010.

[97] D. C. O'Shea, T. J. Suleski, A. D. Kathman, and D. W. Prather, "Diffractive optics: design, fabrication, and test," 2004.

[98] N. Davidson, A. A. Friesem, and E. Hasman, "Analytic design of hybrid diffractive–refractive achromats," *Appl. Opt.*, vol. 32, pp. 4770–4774, Sep 1993.

[99] J. W. Goodman, *Introduction to Fourier optics*. Roberts and Company Publishers, 2005.

[100] H. Schriemer, J. Cook, P. Sharma, L. De La Salle, F. Carle, P. White, V. Tatsiankou, N. Bosscher, J. Haysom, E. Dragomirescu, *et al.*, "Refractive concentrator

optics architectures, tracker precision, and cumulative energy harvest," in *Photovoltaic Specialist Conference (PVSC), 2015 IEEE 42nd*, pp. 1–6, IEEE, 2015.

[101] "NREL SOLPOS sun position calculator." `http://www.nrel.gov/midc/solpos/solpos.html`. Accessed: 2016-10-13.

[102] G. S. Kinsey, P. Hebert, K. E. Barbour, D. D. Krut, H. L. Cotal, and R. A. Sherif, "Concentrator multijunction solar cell characteristics under variable intensity and temperature," *Progress in Photovoltaics: Research and Applications*, vol. 16, no. 6, pp. 503–508, 2008.

[103] H. Helmers, M. Schachtner, and A. W. Bett, "Influence of temperature and irradiance on triple-junction solar subcells," *Solar Energy Materials and Solar Cells*, vol. 116, pp. 144–152, 2013.

[104] H. Cotal and R. Sherif, "Temperature dependence of the IV parameters from triple junction GaInP/InGaAs/Ge concentrator solar cells," in *2006 IEEE 4th World Conference on Photovoltaic Energy Conference*, vol. 1, pp. 845–848, IEEE, 2006.

[105] G. Peharz, J. P. Ferrer Rodríguez, G. Siefer, and A. W. Bett, "Investigations on the temperature dependence of CPV modules equipped with triple-junction solar cells," *Progress in Photovoltaics: Research and Applications*, vol. 19, no. 1, pp. 54–60, 2011.

[106] T. Schult, M. Neubauer, Y. Bessler, P. Nitz, and A. Gombert, "Temperature dependence of fresnel lenses for concentrating photovoltaics," in *2nd International Workshop on Concentrating Photovoltaic Optics and Power, Germany*, 2009.

[107] Y. P. Varshni, "Temperature dependence of the energy gap in semiconductors," *Physica*, vol. 34, no. 1, pp. 149–154, 1967.

[108] I. Vurgaftman and J. Meyer, "Band parameters for nitrogen-containing semiconductors," *Journal of Applied Physics*, vol. 94, no. 6, pp. 3675–3696, 2003.

[109] G. Arbez, J. Wheeldon, A. Walker, K. Hinzer, and H. Schriemer, "Modeling and simulation of triple junction solar cells," in *Photonics North 2010*, pp. 775032–775032, International Society for Optics and Photonics, 2010.

[110] Y. Ota, Y. Sakurada, and K. Nishioka, "Temperature characteristics analysis of InGaP/InGaAs/Ge triple-junction solar cell under concentrated light using spice diode model," in *Photovoltaic Specialists Conference (PVSC), 2010 35th IEEE*, pp. 002093–002096, IEEE, 2010.

[111] G. Siefer and A. W. Bett, "Analysis of temperature coefficients for III-V multijunction concentrator cells," *Progress in Photovoltaics: Research and Applications*, vol. 22, no. 5, pp. 515–524, 2014.

[112] M. A. Steiner, J. F. Geisz, D. J. Friedman, W. J. Olavarria, A. Duda, and T. E. Moriarty, "Temperature-dependent measurements of an inverted metamorphic multijunction (IMM) solar cell," in *Photovoltaic Specialists Conference (PVSC), 2011 37th IEEE*, pp. 002527–002532, IEEE, 2011.

[113] K. Nishioka, T. Takamoto, T. Agui, M. Kaneiwa, Y. Uraoka, and T. Fuyuki, "Annual output estimation of concentrator photovoltaic systems using high-efficiency InGaP/InGaAs/Ge triple-junction solar cells based on experimental solar cell's charac-

teristics and field-test meteorological data," *Solar Energy Materials and Solar Cells*, vol. 90, no. 1, pp. 57–67, 2006.